SYNTHESIS CHARACTERIZATION AND CATALYTIC APPLICATION OF DISORDERED MESOPOROUS MATERIALS FOR OXIDATION REACTIONS

A THESIS SUBMITED TO THE

SAVITRIBAI PHULE PUNE UNIVERSITY

FOR THE DEGREE OF

DOCTOR OF PHILOSOPHY

IN CHEMISTRY

BY

SANJAY SINGH NEGI

Dr. CHINNAKONDA S. GOPINATH

(RESEARCH GUIDE)

INORGANIC CHEMISTRY AND CATALYSIS DIVISION

NATIONAL CHEMICAL LABORATORY

PUNE-411008

INDIA

AUGUST 2015

DECLARATION BY RESEARCH SCHOLAR

I hereby declare that the thesis "**Synthesis characterization and catalytic application of disordered mesoporous materials for oxidation reaction**" submitted for the degree of Doctor of Philosophy to the University of Pune has been carried out by me at the Catalysis and Inorganic Chemistry Division, National Chemical Laboratory, Pune – 411 008, India, under the supervision of Dr. Chinnakonda S. Gopinath and co-supervision of Dr. A. P. Singh. Such material as has been obtained by other sources has been duly acknowledged in this thesis. I declare that the present work or any part thereof has not been submitted to any other University for the award of any other degree or diploma.

Date: August , 2015 **Sanjay Singh Negi**

Catalysis Division,
National Chemical Laboratory,
Pune 411 008,
Maharashtra,
India

राष्ट्रीय रासायनिक प्रयोगशाला
(वैज्ञानिक तथा औद्योगिक अनुसंधान परिषद)
डॉ. होमी भाभा रोड, पुणे - 411 008. भारत
NATIONAL CHEMICAL LABORATORY
(Council of Scientific & Industrial Research)
Dr. Homi Bhabha Road, Pune - 411008. India

CERTIFICATE BY RESEARCH GUIDE

This is to certify that the work incorporated in the thesis entitled, "**Synthesis characterization and catalytic application of disordered mesoporous materials for oxidation reaction**" submitted by **Mr. Sanjay Singh Negi**, for the Degree of **Doctor of Philosophy**, was carried out by the candidate under my supervision in the Catalysis Division, National Chemical Laboratory, Pune – 411 008, India. Such material as has been obtained from other sources has been duly acknowledged in the thesis. To the best of my knowledge, the present work or any part thereof has not been submitted to any other university for the award of any other degree or diploma.

Date: August 17, 2015
Catalysis Division
National Chemical Laboratory,
Pune 411 008,
Maharashtra,
India

Dr. C. S. Gopinath
(Research Supervisor)

Communications Channels ☎ +91 20 25902000 +91 20 25893300 +91 20 25893400 Fax +91 20 25902601 (Director) +91 20 25902660 (Admin.) +91 20 25902639 (Business Development) URL : www.ncl-india.org

राष्ट्रीय रासायनिक प्रयोगशाला
(वैज्ञानिक तथा औद्योगिक अनुसंधान परिषद)
डॉ. होमी भाभा रोड, पुणे - 411 008. भारत
NATIONAL CHEMICAL LABORATORY
(Council of Scientific & Industrial Research)
Dr. Homi Bhabha Road, Pune - 411008. India

CERTIFICATE BY RESEARCH CO-GUIDE

This is to certify that the work incorporated in the thesis entitled, "**Synthesis characterization and catalytic application of disordered mesoporous materials for oxidation reaction**" submitted by **Mr. Sanjay Singh Negi**, for the Degree of **Doctor of Philosophy**, was carried out by the candidate under my co-supervision in the Catalysis Division, National Chemical Laboratory, Pune – 411 008, India. Such material as has been obtained from other sources has been duly acknowledged in the thesis. To the best of my knowledge, the present work or any part thereof has not been submitted to any other university for the award of any other degree or diploma.

Date: August , 2015

Dr. A. P. Singh
(Research Co-Supervisor)

Catalysis Division
National Chemical Laboratory,
Pune 411 008,
Maharashtra,
India

Communications Channels ☎ +91 20 25902000 +91 20 25893300 +91 20 25893400 Fax +91 20 25902601 (Director) +91 20 25902660 (Admin.) +91 20 25902639 (Business Development) URL : www.ncl-india.org

Dedicated to my beloved Parents, Brother and Sister

Acknowledgement

It gives me immense pleasure to express my deep sense of gratitude to my research supervisor, Dr. C. S. Gopinath, who has helped me a lot to learn and understand more about chemistry. I thank him for an excellent and inspiring guidance, constant encouragement, sincere advice and unstinted support during all the times of my Ph.D. work. Also I would sincerely thank Dr. A. P. Singh to understand my hunger for science, understanding my dreams and always providing a helping hand whenever in need. Allowing me to develop and giving independence of thinking and work.

I would like to sincerely thank Dr. T. Raja for allowing me to use facilities in their lab in catalysis division in completing studies with fixed bed flow reactor (Industrial) otherwise which wasn't possible. I would also like to say thanks to Dr. Krishnamurthy for allowing me to use facilities in their lab in polymer division, NCL for fabricating solar cell and completing other related characterizations.

I wish to convey my sincere gratitude to Dr. A. P. Singh, Dr. D. Srinivas, Chair, Inorganic and Catalysis Division for providing necessary infrastructure, and environment; Dr. Nandini Devi for powder-XRD, Dr. Shubhangi, for FT-IR, Dr. Selvaraj for TEM-SEM support, Dr. (Mrs.) S. K. Asha for PL, Dr. S. B. Ogale for FESEM, Dr. (Mrs.) S. S. Deshpande for UV-Vis, Dr. Paresh Dhepe for letting me use the facilities in their lab. My sincere thanks goes to Ms. V. Samuel for DRS-UV and XRD, Mr. R. K. Jha for Nitrogen physisorption analysis, Mr. Ketan for SEM analysis and discussions, Mrs. Rupali Waichal for Raman spectroscopy analysis, and divisional scientists Drs. D. Srinivas, C.V.V. Satyanarayana, P. N. Joshi, C. P. Vinod, Balaraman, and Jagadeesan. I would also like to thank Mr. Purushottaman, Mr. Madhu, Mr. Milind and all other scientific, technical and administrative staff for their cooperation in completing my research and related work successfully in Catalysis division.

I don't have words to express my feelings towards my friends and seniors Deepali, Dr. Umesh Kumar, Dr. Anand Harbindu, Dr. Ankush, Dr. Asha Budakoti,

Dr. Ravindra kumar, Dr. Sallarajendra, Dr. Bhogeshwara Rao, Dr. Atul Kumar, Dr. Ravindra Tawade, Dr. Jeetendra Rout, Dr. Ajeet, Ms. Monika, Mr. Hemander Chand, Mr. Laxman Pudu, Mr. Krunal Patel, Priyanka, Sumona, Ashween, Babasaheb, Divya, Deepak Chand, Ravi, Manoj, Deepak, Anup Pratap, Gaurav, Sayan, Ejaz, Pinka, Singham. I also thank them for regular scientific discussions and it helped me towards thesis submission.

With much appreciation, I would like to mention the crucial role of my labmates, collaborators and friends, Dr. Selva Kumar, Dr. Priti Sharma, Drs. Tushara, Sivaranjani, Nagaraj, Edwin Gnanakumar, Anish, Aswathy, Sudhakar, Jino, Kanak, Rajambal, Anjani, Devaraj, Khiru, Pradnya, Ruchi, Manoj, Prabhu, Madhu, Aruna, Kavya, Femi, Drs. Anand, Sadhu, Ashwin, Bela, kalai and all other research scholars from catalysis division for such a friendly and cheerful working atmosphere, for their constant support, love and care throughout my stay in NCL.

I am forever indebted to my parents, brother and sister for their patience, love, understanding and encouragement throughout my life. Their blessings and encouragement have always made me to take proper decision in all difficult periods. Jai Mata Di, giving me strength to finish my work smoothly.

Finally, my thanks are due to Council of Scientific and Industrial Research, for awarding me NET – Junior/Senior research fellowships. I would like to thank Dr. S. Sivaram, Dr. Sourav Pal, Former Directors, NCL for extending all the support; Dr. B. D. Kulkarni, Dr. Vivek V. Ranade, Deputy Director, Dr. P. A. Joy, Dr. C. G. Suresh, (Past Chairpersons, SAO), Dr. M. S. Sashidhar, Chairman, SAO and all the staffs of SAO, National Chemical Laboratory for extending all the academic helps and to submit this work in the form of a thesis for the award of Ph. D degree.

Pune *Sanjay Singh Negi*

August, 2015

Abbreviation

BE:	Binding Energy
BET:	Brunauer-Emmett-Teller
BJH:	Barrett Joyner Halenda
CB:	Conduction Band
CTAB:	Cetyltrimethylammoniumbromide
CV:	Cyclic Voltammetry
DTA:	Differential Thermal Analysis
DRIFTs:	Diffuse Reflectance Infrared Fourier Transform Spectroscopy
DRS:	Diffuse reflectance spectroscopy
DSSC:	Dye Sensitized Solar Cell
EDAX:	Energy Dispersive Analysis of X-rays
EIS:	Electrochemical Impedance Spectroscopy
FF:	Fill Factor
FID:	Flame ionization detector
GC:	Gas Chromatography
HR-TEM:	High Resolution Transmission Electron Microscopy
HOMO:	Highest Occupied Molecular Orbital
IR:	Infra-red
JV:	Current Voltage plot
LUMO:	Lowest Unoccupied Molecular Orbital
LSV:	Linear Sweep Voltammetry
MCM:	Mobil Composition of Matter materials
MLCT:	Metal to Ligand Charge Transfer
ODH:	Oxidative De-Hydrogenation
PL:	Photoluminescence
p3D:	Psuedo three Dimensional
SAED:	Selective Area (electron) Diffraction
SBA:	Santa Barbara Amorphous materials
SCM:	Solution Combustion Method
SEM:	Scanning Electron Microscopy

SHS:	Self-propagating High-temperature Synthesis
TEM:	Transmission Electron Microscope
TCD:	Thermal Current Detector
TG:	Thermo Gravimetry
UV-Vis.:	Ultra Violet and Visible
VB:	Valence Band
XRD:	X-ray Diffraction
XPS:	X-ray Photoelectron Spectroscopy

Chapter I: Introduction

Introduction

1.1 General Background

Catalysis plays a vital role in day-to-day life since the nature bestowed the phenomenon of enzyme catalysis. Enzymes take part in catalyzing the infinite number of reactions for the physiological functioning of life. An increase of the rate of a process or reaction, brought about by a catalyst, usually present in small masses and unaffected at the end of the reaction is called catalysis. It helps reactions or processes to take place more efficiently or under milder conditions than would otherwise be possible. Materials that speed up the reaction are called positive catalysts or simply catalysts. Catalysts that slow down the reaction are called negative catalysts or inhibitors. Constituents that increase the activity of catalysts are called promoters and constituents that deactivate catalysts are called catalytic poisons. Jöns Jacob Berzelius (1779-1848) was the first scientist one who elaborated the concept of catalysis and coined the term 'Catalysis' in 1835. He described the catalysis as "internal force of substances that enables to awaken the affinities of other bodies, which are asleep at reaction by its mere presence and not by their own affinity" [1, 2]. The above definition demonstrates the fact that the use of catalyst speed up the reaction time along with increment in the yield of the product. The catalyst does not undergo any chemical change or composition during the course of the reaction. Ostwald had experimentally proven that kinetics of the reaction is only changed by the use of catalyst without any change in the free energy of the reactant and products and his contribution was awarded with Nobel Prize in 1909[3]. It involves an altering the pathway of the reaction by decreasing the value of threshold activation energy (E_a). The principle on catalysis is schematically represented in scheme 1. The formation of the activated transient state complex between the catalyst and the reactants is advantageous in lowering the activation energy. The free energy of the reactants as well as products is not changed in the presence of the catalyst. Thereby the reaction is accelerated in short time-scale and also the turn over number of the reaction is also increased. Based on the phases of the reaction catalysis can be divided into homogeneous catalysis, heterogeneous catalysis and biocatalysis.

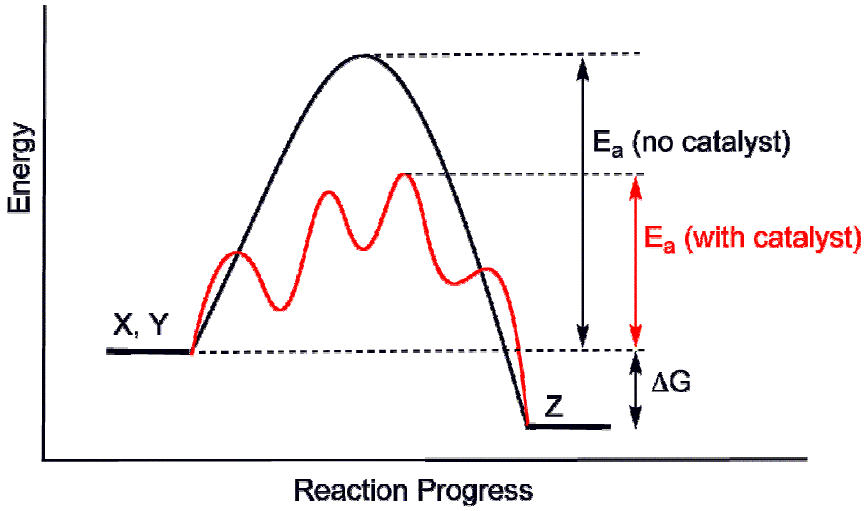

Scheme1. Schematic illustrating effect of catalyst on reaction pathway, mechanism.

A. Homogeneous Catalysis. When the catalyst is in same phase as that of reactants, the type of catalysis is known as homogenous catalysis. Most commonly, a homogeneous catalyst is co dissolved in a solvent with the reactants. High selectivity, conversion, and yield at ambient or near ambient reaction conditions are attractive features of this type of catalysis. The use of noble metal catalysts and its poor recovery remain as disadvantages. Homogeneous catalysts are primarily used for production of fine chemicals, exotic products and coupling reactions [4].

B. Heterogeneous Catalysis. When the catalyst is in different phase from that of reactants, the type of catalysis is referred to as heterogeneous catalysis. Generally, this type of catalysis demands harsh temperature and pressure conditions. The easy recovery of the catalyst and recyclability for several times are the salient features of this type of catalysis. Many industrial catalysts works anywhere between few months to years, at a stretch, underscores the economics associated with heterogeneous catalysts. Heterogeneous catalysis is of supreme importance in many areas of the chemical and energy industries, production of petroleum products, large scale of organic chemicals, biomass conversion and automobile industries. Heterogeneous catalysis has engrossed Noble prize for Fritz Haber and Carl Bosch in 1918, Irving Langmuir in 1932, and Gerhard Ertl in 2007 in the subject area of chemistry, apart

from many more in the area of heterogeneous catalysis. Heterogeneous semiconductor photocatalysis for harvesting solar energy attracts high research interest in the last few decades. It operates at ambient conditions, rather than harsh treatments required in other heterogeneous catalysis operations[5].

C. Enzyme and Biocatalysis. In biology, enzymes are protein-based catalysts in metabolism and catabolism. Most biocatalysts are enzymes, but other non-protein-based classes of biomolecules also exhibit catalytic properties including ribozymes, and synthetic deoxyribozymes. Biocatalysts can be considered of as intermediate between homogeneous and heterogeneous catalysts, although strictly speaking soluble enzymes are homogeneous catalysts and membrane-bound enzymes are heterogeneous. Many factors affect the activity of enzymes (and other catalysts) including temperature, pH, and concentration of enzyme, substrate, and products. A principally important reagent in enzymatic reactions is water, which is the product of many bond-forming reactions and a reactant in many bond-breaking processes. In biocatalysis; enzymes are employed to prepare many commodity chemicals including high fructose corn syrup and acrylamide. Some monoclonal antibodies whose binding target is a stable molecule which resembles the transition state of a chemical reaction can act as weak catalysts for that chemical reaction by lowering its activation energy. Such catalytic antibodies are sometimes called "abzymes" [6].

1.2 Porous Materials

Generally catalysis depends on the surface area of catalysts, since it composes active sites of catalysis. Porous nature of catalytic material helps in many different ways to help catalysis, such as exposure of active sites, easy diffusion of reactants and products etc. Porous materials have voids, blank spaces inside them. According to the IUPAC definition, porous materials are classified based on their pore diameter as microporous, mesoporous and macroporous material. Microporous materials exhibit pores of less than 2 nm pore diameter. Macroporous materials are having pore diameter of more than 50 nm. Mesoporous materials are with pore diameter in between 2 – 50 nm [7, 8]. Most of the organic molecular size lies at the lower end of mesoporous and microporous regime; however, mesopores helps in the diffusion of

almost all molecules, which is a pre-requisite for better catalysis. Indeed mesoporous materials are of large interest to experimental chemists.

Mesoporous materials are classified as ordered and disordered mesoporous materials depending on arrangement/nature of pore in the material [9, 10]. Ordered mesoporous materials as MCM, SBA class of materials are prepared using structure directing agents example: pluronic acid (P123), cetyltrimethylammoniumbromide (CTAB). These materials have very ordered nature of the pores as depicted in the TEM image in figure 1a. Disordered mesoporous materials need no structure directing agents; however disordered mesoporous materials are synthesized by many different methods, including solution combustion method using fuels and oxidants. Lengths of pores are of few nanometers as seen in figure 1b, thus are ordered (pseudo) three dimensionally (p3D). Porous materials affect various materials science fields such as electrochemistry, sensors, catalysis, and photochemistry. In heterogeneous catalysis, disordered nature benefits over ordered porosity as small diffusion depths leads to better control over yields and selectivity of products.

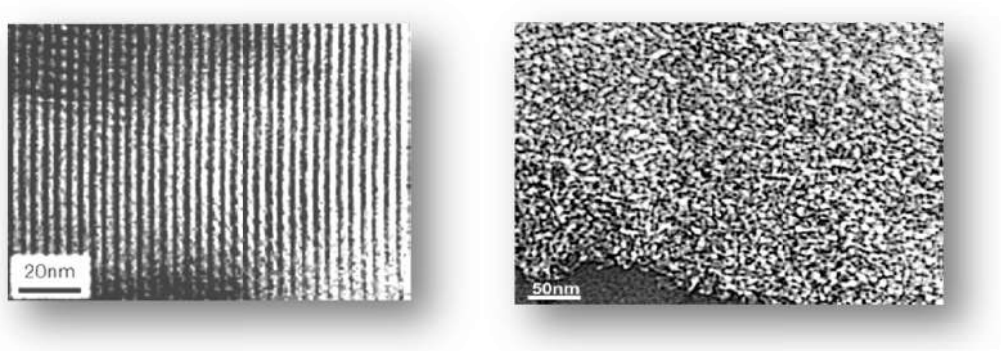

Figure 1. TEM image of ordered mesoporous materials (left), and disordered mesoporous materials (right).

1.3 TiO_2

1.3.1 Phases of Titanium Dioxide

Titanium dioxide is a naturally occurring transition metal oxide of titanium. Titanium dioxide occurs in nature as well-known minerals rutile, anatase and brookite. Rutile is the most stable, abundant and contains around 98% titanium dioxide in the ore. Rutile and anatase are two polymorphs of TiO_2 based on distorted close-packed, or eutactic, anion arrays. Space group for rutile phases is $P4_2/mnm$, and its unit cell parameters are a = 4.5937 Å, c = 2.9587 Å; Z = 2; anatase space group is $I4_1/amd$ with unit cell

parameters are a = 3.7845 Å, c = 9.5143 Å; Z = 4; brookite space group is2/m 2/m 2/m Z = 8, and unit cell parameters are a = 5.4558 Å, b = 9.1819 Å, c = 5.1429 Å. It has a broad range of applications, from paint to sunscreen to food coloring [11].

Rutile can be described as a tetragonal variant of the orthorhombic $CaCl_2$ structure. This arrangement (Figure 2a) is one of the likely ways of filling half of the octahedral holes of a hexagonal close-packed array of oxide ions to give a system with the MO_2 stoichiometry. Chains of edge-sharing octahedra, linked to each other by sharing vertices, are a striking feature of this structure. In the $CaCl_2$ structure the oxide ions are coordinated by three metal atoms in a distorted trigonal-pyramidal geometry, point symmetry C_s. The $CaCl_2$ to rutile transformation leads to a structure where these pyramids have become rigorously planar (point symmetry C_{2v}) with a unique 0-Ti-0 angle of about 99". The metal octahedra are not regular, and four short and two long Ti-0 distances are found, irrespective of the temperature of the structure determination.

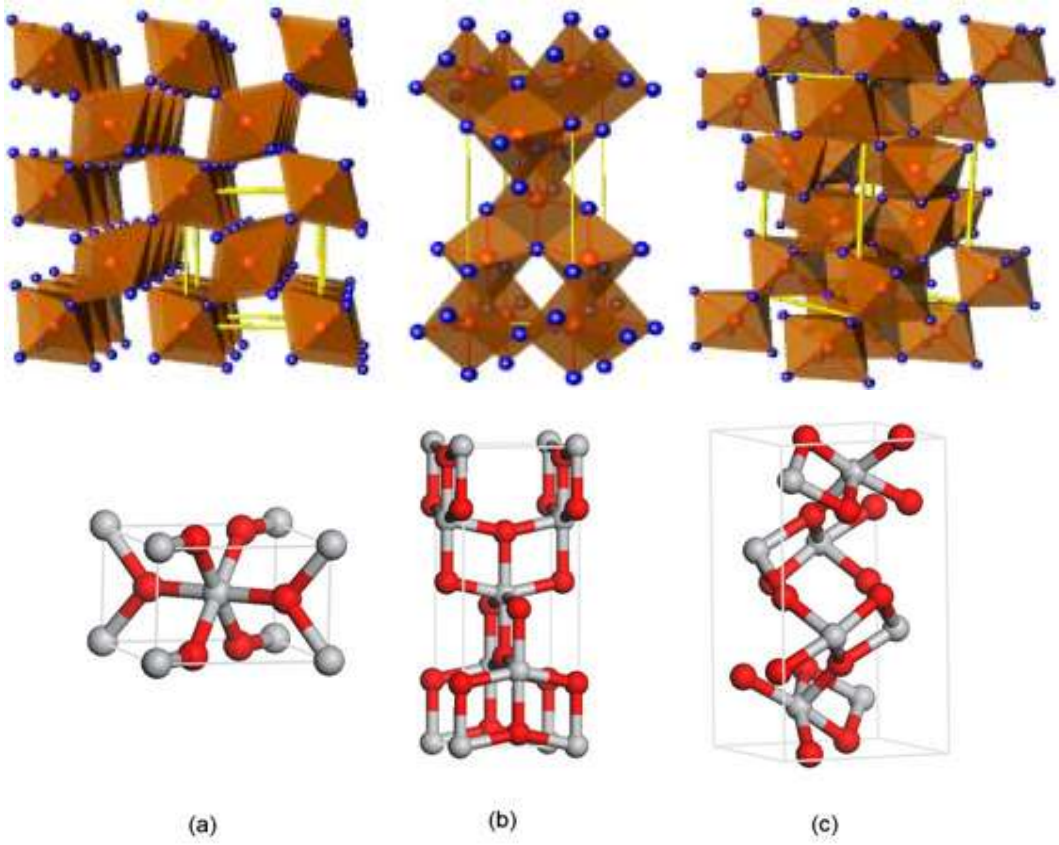

Figure 2. Unit cell and extended cell structure of Anatase, Rutile and Brookite phases of TiO_2.

The anatase structure may be similarly derived from a cubic close-packed array of oxides ions. The sense of the distortion around the Ti atom is similar to that for rutile and is maintained at low temperature, although the temperature sensitivity appears to be a little less. The TiO_6 octahedron in anatase shares four edges compared to the two in rutile. As a result of such sharing, there are short 0-0 distances in both polymorphs. In anatase the shortest is ~0.1 Å shorter than in rutile. Figure 2b shows some views of the structure.

Of the three phases of TiO_2 in the anatase phase is the most widely studied polymorph because of its high activity in catalysis and photocatalysis. The average surface energies of anatase TiO_2 (0.90 J m^{-2} for {001}, 0.53 J m^{-2} for {100}, 0.44 J m^{-2} for {101}) have been established extensively. Unfortunately, {101} surfaces, normally the majority of the external surface of anatase TiO_2 (more than 94% percent, according to the Wulff construction), are thermodynamically stable with a low surface energy (0.44 J m^{-2}), which determines its low reactivity. To improve its reactivity, the synthesis of shape-controlled anatase TiO_2 crystals with specific reactive facets exposed is greatly desired, and the minority surfaces such as {001} one's with a higher surface energy (0.90 J m^{-2}) attract extensive interest [12].

1.3.2 Reducible Nature of TiO_2

Titanium exists in +2, +3 and +4 oxidation states, thus acts as a reducible support. Thus reducible or change in oxidation states by TiO_2 is exploited for redox reactions and photocatalytic reactions. Reducibility of TiO_2 plays an excellent role for supporting many different metals and helps them for catalysis. TiO_2 help in many catalysis reactions because of redox feature. For example, Au supported TiO_2 for low temperature CO oxidation, [13] Pt/TiO_2 for water gas shift reaction, [14] Co/TiO_2used for Fischer-Tropsch synthesis, [15] metal supported titania catalysts are used for hydrodesulphurization of petroleum products [16].

1.3.3 Semiconducting Nature of TiO_2

On 1972, for first time, Honda and Fujishima used rutile TiO_2 for electrochemical photolysis of water along with Pt. Then onwards TiO_2 materials are progressively utilized for various reactions, including harvesting of solar energy [17]. Currently TiO_2 is being used for DSSC, sunscreen, paints, and pigment to block UV radiation of sun. Anatase TiO_2 is a semiconductor with a wide band gap of 3.2 eV. Thus it absorbs

in high energy UV light ($\lambda \leq 380$ nm), generate pair of electron and hole upon light absorption. TiO_2 acts as a good photocatalyst, water splitting for hydrogen production, oxidative degradation of pollutants, paints for removal of volatile organic compounds.

1.3.4 Titania Modification

Titania properties could be modified in several ways, such as doping with anion or cations in the TiO_2 lattice. Foreign elements, if when doped into host lattice, lead to good catalysts due to interaction between guest and host support. Doping of titania with nonmetals was carried out to use it as a support and gain catalytic activity for oxidation reaction. Doping of nonmetals generates new states into TiO_2 system and helps towards reduction in band gap. Energy states of foreign elements could overlap with that of TiO_2, thus the energy difference between the levels will decrease. Introduction of N, C, F nonmetals is thus favored, also doping of cations into lattice is favored [18].

1.4 Catalysis

1.4.1 Oxidation Reactions

An oxidation-reduction (redox) reaction is a type of chemical reaction that involves exchange of electrons and holes between two species. An oxidation-reduction reaction is any chemical reaction in which the oxidation number of a molecule, atom, or ion changes by gaining or losing an electron. Oxidation can also be defined as addition of oxygen, and/or removal of hydrogen. We have used titania based materials for oxidation reactions, i.e. addition of oxygen atom, removal of hydrogen atoms from a molecule [19].

Sulfoxidation is a catalytic oxidation of sulfide to partial oxidation product, sulfoxide and consecutively to total oxidation product i.e. sulfone as shown in scheme 1. Partial oxidation product (sulfoxide) is of interest, as many pharmaceutically important sulfoxide molecules ex, dapsone, (sodium glucosulfone) promin, esomeprazole and armodafinil are there. Currently homogeneous catalysts with toxic oxidants are used under harsh reaction conditions. These partial oxidations suffer with low conversion, with less sulfoxide selectivity. Thus heterogeneous catalysts which can operate at moderate reaction condition with better control of the product are the need of industry.

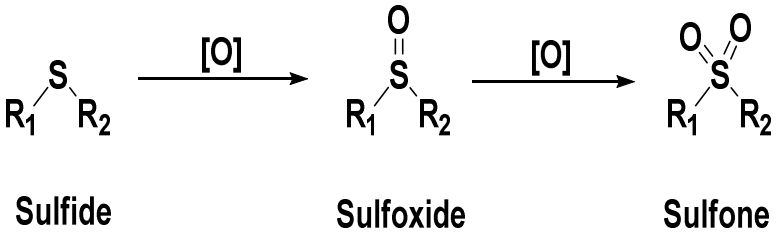

Sheme1. Schematic for sulfide oxidation to sulfoxide followed to complete oxidation product i.e. sulfone.

Styrene is industrially important precursor for polymers and fine chemicals; industrially it's synthesized via dehydrogenation of ethylbenzene over iron catalyst at 700 °C as shown in scheme 2. Operating mechanism is via dehydrogenation of ethylbenzene to styrene, which is endothermic in nature, and hence it operates at high reaction temperatures. Oxidative dehydrogenation mechanism is of exothermic nature and thus reduces operating temperature of reaction. Thus research is carried out to find catalysts which are operating at lower reaction temperature via ODH mechanism.

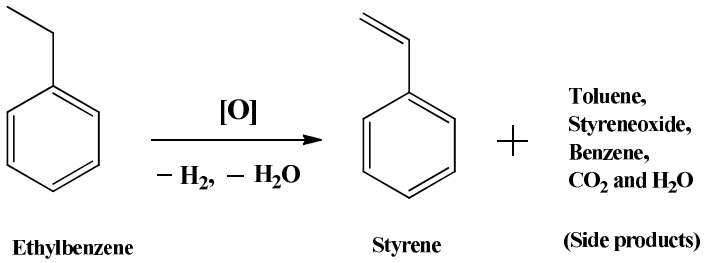

Scheme 2. Schematic for ethylbenzene to styrene by oxidative dehydrogenation/ dehydrogenation.

1.4.2 Photocatalysis

Photocatalysis is the acceleration of photoreaction in the presence of catalyst using photon particles. Photocatalysis consists of light absorption by the catalyst material, then electron and hole pair (charge carriers) generation and charge diffusion to the surface, and finally redox reaction. Chemical species reduction potential is a measure of the tendency to acquire electrons and thereby be reduced. Reduction potential is measured in volts (V), or millivolts (mV). Hydrogen evolution potential from water is at 0 V (by reduction of water) and oxygen evolution potential (from water oxidation) is at 1.23 V vs. NHE at pH 0.

TiO_2 photocatalystis a wide band gap material thus absorbs in UV light. Visible light absorption can be induced by reducing band gap of TiO_2. Doping foreign anion or cation into lattice generates new energy states closer to VB or CB thus reducing band gap. In photocatalysis, rate at which recombination occurs is a critical parameter; "recombination rate" depends on the number of excess minority carriers. If for example, there are no excess minority carriers, then the recombination rate must be zero. Two parameters that are integral to recombination rate are the minority carrier lifetime and the minority carrier diffusion length.

The minority carrier lifetime of a material, denoted by τ_n or τ_p, is the average time which a carrier can stay in an excited state after electron-hole generation before it recombines. It is often just referred to as the "lifetime" and has nothing to do with the stability of the material. The second related parameter to recombination rate, the "minority carrier diffusion length," is the average distance a carrier can move from point of generation until it recombines. The minority carrier lifetime and the diffusion length depend primarily on the type and magnitude of recombination processes in the semiconductor. The diffusion length is related to the carrier lifetime by the diffusivity according to the following formula:

$$L = \sqrt{D\tau}$$

Where τ is the lifetime in seconds, D is the diffusivity in m^2/s and L is the diffusion length in meters. A higher recombination rate lowers efficiency.

1.4.3 Hydrogen Generation via Water Splitting

Hydrogen is an important molecule in industries; it's used for refining, fuel, hydrocracking, ammonia synthesis. Conventional fuel sources are getting exhausted and need for alternative sources of energy. Up to now conventional source are used for hydrogen gas production industrially. Currently the dominant technology for hydrogen production is steam reforming from hydrocarbons or fossil fuels, natural gas, methane. Many other methods are known including electrolysis and thermolysis. Hydrogen is a high energy density molecule with zero carbon in it and when used as fuel it gives energy and water as a by-product. H_2 is considered as future energy source for mankind. Water splitting for hydrogen production using sunlight can be considered as a green method. Cheap methods to produce hydrogen will help in establishment of hydrogen economy [20].

Hydrogen production by photolysis of water is a greener opportunity. Photocatalyst material will absorb light, upon light absorption electron and holes will be generated and will diffuse towards the surface, surface charges are utilized for splitting water (redox reaction) generation H_2 and O_2 as shown in figure 3. Unfortunately this isn't a simple reaction; many problems are associated with photocatalytic water splitting. Water splitting is (a) an endothermic reaction (ΔG +ve) and reverse reaction is also possible on catalyst surface, (b) charge recombination decreases the efficiency, (c) noble elements are used as co catalysts (not abundant), (d) catalysts stability is a problem, (e) catalyst should be selective for O_2 and H_2, (f) visible light active catalyst are few in number, and (g) sacrificial agent are added for H_2 production in the reaction medium. All these problems lead to very low water splitting efficiency; also with limited photocatalyst materials. A far more challenging is the particulate nature of the photocatalyst, which encourages charge recombination due to plenty of defects on surfaces, especially nanocatalyst surfaces. Thus photocatalytic water splitting is of research interest, to understand the problems as well as to design a better catalyst.

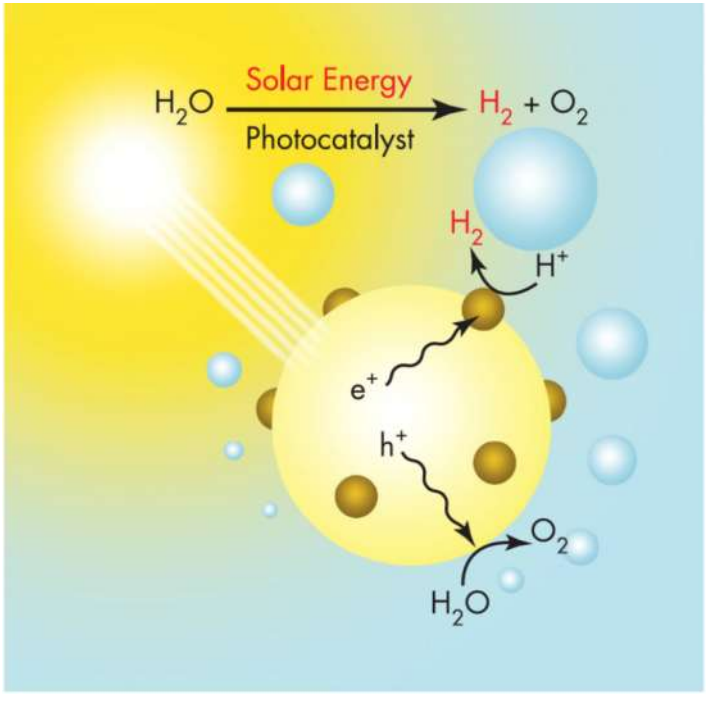

Figure 3. Schematic for water splitting by TiO_2 photocatalyst [21].

1.4.4 Solar Cell

Alternate source of energy are needed for future. Solar light conversion technique such as solar cell is a good option, currently conventional and costly silicon solar cell technologies are used for converting solar light to electricity. Thus there is a need for alternate, cheap and improved solar light harvesting techniques, such as dye sensitized solar cells (DSSC). Dyes are essentially used to absorb solar light [22] and polycrystalline semiconductors are used for harvesting generated charge carriers thus to get good solar to electricity energy conversion efficiency. Dye sensitized cells are also known as Grätzel cells, as it was discovered by Brian O'Regan and Michael Grätzel. Efforts are going on to understand the leaks of these thin layers DSSC and develop better devices based on these understandings. Conventional DSSC's design and working can be described as in Figure 4. Glass plates are taken and coated with transparent conducting material, such as FTO or ITO. Working electrode is prepared by pasting nano TiO_2 paste over conducting glass plate, visible light active dye molecules is absorbed onto the mesoporous titania for sensitization.

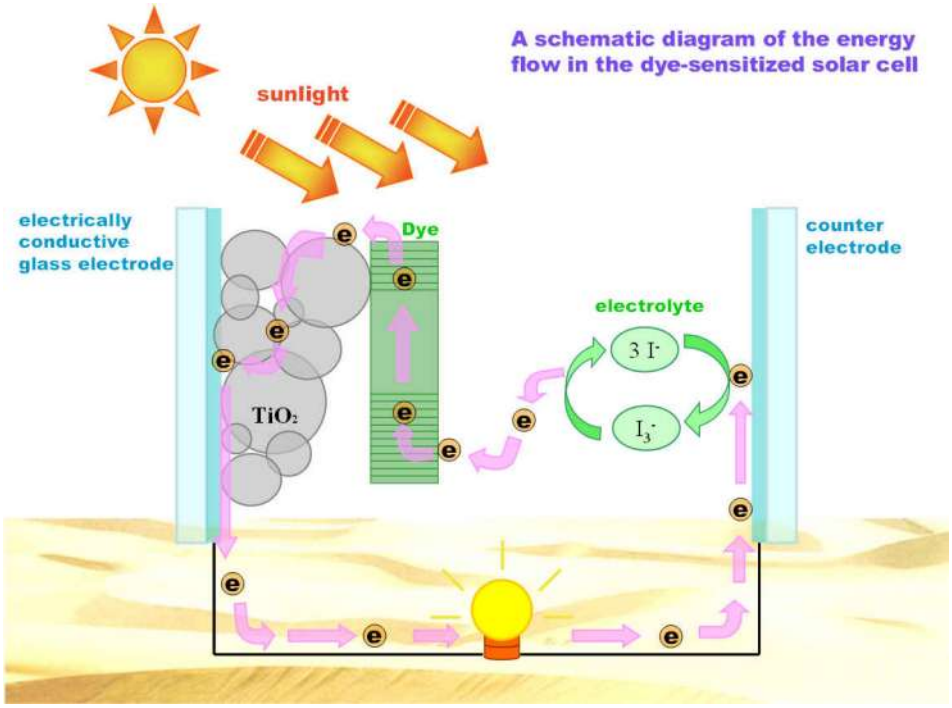

Figure 4. Schematic to show working of dye sensitized solar cell.

Redox electrolyte/mediator solution was filled in between the working and counter electrode. Above cell is irradiated with photons of energy higher than the

energy of highest occupied molecular orbital and lowest unoccupied molecular orbital or simply HOMO-LUMO gap of dye will be absorbed by the molecule. Upon light absorption by dye molecule, electrons and hole pairs are generated, and electrons to be directed from dye molecule to the conduction band of TiO_2 and then towards external circuit. Holes from dye are to be consumed by redox mediator i.e. iodide (I^-) – triiodide (I_3^-) system. Electron from the external electrode will reach counter electrode, will be consumed by the redox mediator to regenerate it again. However, there are many possibilities are available towards charge recombination, due to very small life time of charge carriers, and long life time for charge utilization. Thus various recombination mechanisms are operating which decreases the efficiency of the solar cell. Ultimately, the efficiency of the DSSC is decided by the number of electrons generated that actually generates electricity to the total number of photons absorbed, assuming one photon generates one e-h pair.

1.5 Objective of Thesis

Disordered mesoporous materials have advantages over ordered mesoporous and also nonporous materials. Hence controlling preparation of the disordered mesoporous materials will lead to better catalysts. Synthesis strategies which can affect these surface area, porosity and textural properties are sought after. Disordered mesoporous TiO_2 materials are used as active catalyst, and also doped with other elements to give better catalytic activity. Different metal ion can be doped into TiO_2 lattice and employed for various reactions [23]. Prepared materials are used for redox reactions. It is well known that vanadium pentoxide exhibits high oxidizing capacity and used as catalyst for combustion reactions. However, single or small number of vanadium atom clusters acts as good catalyst for partial oxidation reactions. Indeed, isolated vanadyl species are good for partial oxidations, and polymeric or bulk O-V-O species are efficient for complete oxidation. Isolated V/TiO_2 prepared via doping of vanadium introduced in the titania lattice $V_xTi_{1-x}O_2$ materials. If $V_xTi_{1-x}O_2$ can be prepared with high surface area and mesoporosity, it is likely to assist many reactions. In the present thesis, these $V_xTi_{1-x}O_2$ materials are used for partial oxidations of sulfides to pharmaceutically important sulfoxide molecules. By introducing a small percentage of V or any other metal ion into the lattice of TiO_2 leads to isolated metal ion into the lattice and hence catalysis properties can be tuned. Vanadium is more appropriate due

to its flexible oxidation state between 4+ and 5+ and a compatible ionic size to that of Ti4+ in TiO_2. Similarly Mn-doping also is equally possible for similar reasons. $Mn_xTi_{1-x}O_2$is prepared through Mn loading into TiO_2 lattice. Pseudo 3D (p3D) $Mn_xTi_{1-x}O_2$ mesoporous materials has been used for oxidative dehydrogenation of ethylbenzene to produce styrene. $Mn_xTi_{1-x}O_2$materials operates through oxidative dehydrogenation mechanism thus, affects EB to ST conversion at lower temperature than industry employed Fe catalyst. H-TiO_2 materials were prepared via adding reduced sites inside the TiO_2 lattice to generate a new mid-gap energy state thus reducing the band gap. These new materials (H-TiO_2) with absorbance in visible region are synthesized and applied for photocatalytic water splitting for hydrogen generation.

1.6 Outline of Thesis

The thesis deals with synthesis methods of V/TiO_2, Mn/TiO_2, and H-TiO_2mesoporous materials. First two set of materials exhibits disordered mesoporous nature with pseudo three dimensional character, namely p3D. Several characterization techniques (structural, spectral, microscopy, electrochemical) were used, for understanding of these materials; characterization results give a proper understanding of these materials. Reaction parameters for partial oxidation of sulfides to sulfoxides, ethylbenzene to styrene conversion, photocatalytic water splitting to produce H_2 and CO_2 through redox reactions, solar cell device formation for solar light conversion to electricity using p3D catalysts were obtained. Chapter wise description of the thesis is outlined in the following paragraphs.

Chapter I. Elaborate general introduction about porous materials, especially ordered and disordered mesoporous materials are given along with their advantages. As titanium dioxide is the main material dealt in all the working chapters, its structure and different phases available are discussed. A material modification aspect, such as doping, is introduced along with its advantages in catalysis. General introductions about various reactions carried out in this thesis, such as sulfide to sulfoxide, ethyl benzene to styrene by oxidative dehydrogenation route, are given. Photocatalysis aspects were described, for H_2 evolution from water splitting, and dye sensitized solar

cell fabrication for current generation. The objectives and scope of the thesis is also presented in the last section of the chapter.

Chapter II. Synthesis aspects of different materials prepared along with preparation details are presented. Although many routine and special physicochemical methods have been employed for characterization of catalyst materials, those special methods are described in detail. Experimental conditions, reactor setup used for various oxidation reactions, methods used are discussed in detail. Necessary basic theoretical aspects of characterization techniques used have been discussed in this chapter.

Chapter III. Vanadium doped titania (V/TiO_2) with isolated V species containing catalysts were prepared via solution combustion method. V/TiO_2 materials were characterized via various physiochemical methods. Materials were analyzed for their structural, textural and morphological features with XRD, Raman spectroscopy, N_2 physisorption, HRTEM, EDX techniques. V/TiO_2 materials were employed, via batch reactor, for partial catalytic oxidation of sulfides to sulfoxides. The potentiality of materials is also established for partial oxidations at ambient and below ambient temperatures. Effect of composition, temperature, recycle studies were made for various sulfides with aq. H_2O_2 oxidant. Many sulfide systems have been evaluated for sulfoxidation with the present catalyst. $V_xTi_{1-x}O_2$ systems exhibit high selectivity and yield at ambient and below ambient temperature conditions.

Chapter IV. $Mn_xTi_{1-x}O_2$ systems were prepared via solution combustion method. As-prepared $Mn_xTi_{1-x}O_2$ materials were characterized by various physiochemical methods. $Mn_xTi_{1-x}O_2$ materials were evaluated for ethylbenzene (EB) to styrene conversion via fixed bed reactor. Air or O_2 was used as oxidant for EB conversion under relatively milder temperatures around 500 ± 50 °C than the current commercial process that occurs around 700 °C. Mechanism of operation and optimum reaction conditions for high styrene yield was found. Very interestingly, initial anatase $Mn_xTi_{1-x}O_2$ undergoes structural changes to Mn_3O_4 supported on rutile titania in the first few hours of the reaction, especially due to highly exothermic reaction conditions. A thorough analysis of fresh and spent catalysis reveals many interesting aspects of the catalyst, reaction mechanism etc. In fact, Mn_3O_4 supported on rutile titania is the

active form of the catalyst, although anatase form of $Mn_xTi_{1-x}O_2$ was the initial catalyst. Oxygen diffusion into the sub-surface and bulk of the catalyst was verified and it indicates the operative of Mars van Krevelen mechanism.

Chapter V. Chapter five includes the application of H–TiO_2 for two applications, namely water splitting and dye-sensitized solar cell. H-TiO_2 systems were prepared via reducing TiO_2 under hydrogen atmosphere, and the reduction conditions were varied such as reduction temperature and pressure. H-TiO_2 materials are thoroughly characterized for material properties and light absorption character. H-TiO_2 materials are used for hydrogen evolution reaction from water splitting with aqueous methanol solution under different photon sources. Second section gives details about the art of fabricating dye sensitized solar cell. Devices were characterized via JV plot, and impedance spectroscopy. Important features to increase the efficiency of solar light harvesting were analyzed.

1.7 References

1. J. J. Berzelius, *Årsberättelsen om framsteg i fysik och kemi*, *Royal Swedish Academy of Sciences*, (1835); J. A. Christiansen, *J. Phys. Chem.*, (1924) **28** 145–148; S. E. Denmark, H. M. Chi, *J. Am. Chem. Soc.* (2014) **136** 3655−3663.
2. B. Lindström, L. J. Pettersson, *Chem. Eng. Technol*, (2003) **26** 473-478; J. H. Barber, B. E. Conway, *J. Chem. Soc., Faraday Trans.,* (1996) **92** 3709-3717; E. Peris, R. H Crabtree, *Coord. Chem. Rew,* (2004) **248** 2239–2246.
3. W. Ostwald, *Energetische Grundlagen der Kulturwissenschaft* (1st ed.) Leipzig (1909); A. S. Zarkalis, C. Y. Hsu, B. C. Gates, *Catal. Lett.* (1994) **29** 235-239.
4. C. Elschenbroich, "*Organometallics*" Wiley-VCH: Weinheim (2006).
5. Foreword for the Gerhard Ertl Festschrift, *J. Phys. Chem. B*, (2004) ***108***14183–14186.
6. D. L. Nelson, M. M. Cox, *Lehninger, Principles of Biochemistry* (3rd ed.) New York (2000).

7. F. Schüth, K. S. W. Sing, J. Weitkamp, *Handbook of Porous Solids*, Wiley-VCH, Weinheim, (2002).
8. D. Zhao, J. Feng, Q. Huo, N. Melosh, G.H. Fredrickson, B.F. Chmelka, G.D. Stucky, *Science,*(1998) **279** 548–552.
9. P. Sharma, A. P. Singh**,** *RSC Adv.***,** (2014) **4** 43070-43079.
10. D. G. Kulkarni, A. V. Murugan, A. K. Viswanath, C. S. Gopinath, *J. Nanosci. Nanotechnol.,* (2009) **9** 371–377.
11. K. Nakata, A. Fujishima, *J. Photochem. and Photobio. C: Photochemistry Rev.,* (2012) **13** 169–189.
12. U. Diebold, *Surface Science Reports,* (2003) **48** 53-229.
13. M. Haruta, *Catal. Today,* (1997) **36** 153−166.
14. P. Panagiotopoulou, D. I. Kondarides, *Catal. Today,* (2006) **112** 49–52.
15. B. Jongsomjit, C. Sakdamnuson, J. G. Goodwin Jr, P. Praserthdam, *Catal. Letters,* (2004) **94** 3–4.
16. J. Ramırez, G. Macıas, L. Cedeno, A. G. Alejandre, R. Cuevas, P. Castillo, *Catal. Today,* (2004) **98** 19–30.
17. A. Fujishima, K. Honda, *Nature,* (1972) **238** 37-38.
18. K. Sivaranjani, C. S. Gopinath, *J. Mater. Chem.*(2011) **21** 2639-2647.
19. S. S. Negi, A. T. Venugopalan, T. Raja, A. P. Singh, C. S. Gopinath, *RSC Adv.,* (2014) **4** 57087-57097.
20. K. Sivaranjani, S. Rajaambal, T. Das, K. Roy, S. Bhattacharyya, C.S. Gopinath, *ChemCatChem*, (2014) **6** 522–530.
21. http://www.chemsys.t.u-tokyo.ac.jp/laboratory_domen-kubota_e.html
22. M. K. Nazeeruddin, A. Kay, I. Rodicio, R. H. Baker, E. Mueller, P. Liska, N. Vlachopoulos, M. Gratzel, *J. Am. Chem. Soc.*, (1993) **115** 6382–6390.
23. S. T. Martin, C. L. Morrison, M. R. Hoffmann, *J. Phys. Chem.*(1994) **98** 13695-13704; K. A. Griffin, A. B. Pakhomov, C. M. Wang, S. M. Heald, K. M. Krishnan, *Phy. Rev. Lett.* (2005) **94** 157204; A. K.Chandiran, F. Sauvage, M. C. Cabanas, P. Comte, S. M. Zakeeruddin, M. Graetzel, *J. Phys. Chem. C* (2010) **114** 15849–15856; A. Ghicov, M. Yamamoto, P.Schmuki, *Angew. Chem.*(2008) **120** 8052 –8055; N. Serpone, D. Lawless, *Langmuir* (1994) **10** 643-652.

Chapter II: Theory and Experimental Procedures

2. Theory and Experimental Procedures

In this chapter we have given an account of the preparation methods and different characterization techniques employed to explore the physicochemical properties of the materials. Preparation methods control physical, textural, optical and electronic properties of catalysts, thus control materials activity, selectivity in a catalytic process [1]. We have used solution combustion method for fast and simple synthesis of disordered mesoporous materials for unique catalytic properties, such as V doped titanium dioxide for partial oxidation reactions [2]. Incipient wet impregnation method, for preparation of 5% manganese oxide on titania was employed [3]. We have also used high temperature, high pressure reduction method to prepare H-TiO_2 materials for solar light harvesting application experiments [4]. Materials are analyzed for their textural properties using N_2 physisorption, structural features were studied using PXRD, Raman spectroscopy, and DRIFTs methods, electronic properties were explored using XPS and DRS, elemental composition analysis were made by SEM-EDAX studies, morphological analysis using HRTEM techniques. These techniques help us to explain the nature of Mn, V doped into rutile TiO_2. Also selected spent catalysts were analyzed to understand the active material under reaction condition.

2.1 Catalyst Preparation Method

2.1.1 Solution Combustion Method

The synthesis of solids having desired structures, composition and properties continues to be a major challenge to chemists, material scientists and engineers [5]. Combustion synthesis (CS) or self-propagating high-temperature synthesis (SHS) is an effective, low-cost method for synthesis of various industrially useful materials, for synthesizing single phase solid solutions, nanomaterials, porous materials, crystalline oxides, composites as well as complex mixed oxide phases and homogenous doping in metal oxides. The term ‘combustion’ covers flaming (gas-phase), smoldering (heterogeneous) as well as explosive reactions. The strategy of the technique adopts a self-persistent reaction between an oxidizer and fuels that are dissolved in water medium. The process makes use of extremely exothermic redox chemical reactions between metals and nonmetals, the metathetical (exchange) reaction between reactive compounds or reactions involves redox compounds/mixtures. The combustion method has been successfully used in the preparation of a large number of technologically

useful oxide (refractory oxides, catalysts, magnetic, semiconducting, insulators, dielectric, sensors, phosphors etc.) and nonoxide (carbides, nitrides, borides, silicides etc.) materials [6]. It was understood that the conventional solid state SHS being a gasless combustion process typically yields much coarser particles than solution combustion approach. Combustion synthesis is broadly classified into three types based on the nature of the initial reaction medium:

- Conventional SHS of nanoscale materials, i.e. initial reactants are in solid state (condensed phase combustion).
- Solution combustion synthesis (SCS) of nanosized powders, i.e. initial reaction medium is aqueous solution.
- Synthesis of nanoparticles in flame, i.e. gas-phase combustion.

Solution combustion synthesis (SCS) is a simple, rapid and versatile process, which allows effective synthesis of a variety of nanosize materials [7]. The solution processes have been increasingly used due to their peculiar and unique characteristics. This process not only yields nanosize oxide materials but also allows uniform (homogeneous) doping of trace amounts of metal ions in a single step. In recent years, there has been remarkable interest in the combustion synthesis of materials because of its simple, fast, energetically economic and yields high purity products compared to the conventional routes to prepare these materials.

SCS is a method based on the principle that once are action is initiated under heating, an exothermic reaction occurs that becomes self-sustaining within a certain time interval, resulting in a powder as final product. As it is a high-temperature process, only thermodynamically stable phases can be prepared. Solution combustion synthesis process involves a self-sustained reaction in homogeneous solution by use of salts, such as nitrates, metal sulfates and carbonates, as oxidants and, reducing reagents, fuels such as glycine, sucrose, urea, hydrazides or other water soluble carbohydrates. Nitrate acts as an oxidizer for the fuel during the combustion reaction. The powder can be a pyrolyzed product of a single phase, but usually it is a combination of metal oxides and in some cases it needs subsequent heat treatment to form single phase products, which are usually the results required in this process. The exothermic reaction begins at the ignition temperature and generates a certain amount of heat that is manifested in the maximum temperature or temperature of combustion. Solution combustion synthesis has the advantage of rapidly producing fine and

homogeneous powders. Since it is an exothermic, auto-propagated process, and with a high heat release rate, it can be explosive and should be undertaken with extra precautions. Depending on the type of the precursors, as well as the conditions used for the process organization, the SCS may occur as either volume or layer-by-layer propagating combustion modes.

a. Self-propagation mode: The reaction initiates locally and propagates a wave-like pattern throughout the medium. This type of mode takes longer time for completion. The slow but stepwise heating favors the growth of nanoparticles. The steady evolution of reactant gases produces wormhole mesoporous materials that are acclaimed for having the property of fast diffusion of charge carriers from the bulk to the surface. For an example, mesoporous V-doped TiO_2 is prepared by combustion synthesis via self propagation mode.

b. **Voluminous combustion mode**: There is uniform heating and concurrent reaction occurs throughout the reaction mixture. This mode is advantageous for producing crystalline materials. The feature of crystallinity in photocatalysts is one of the important factors for reducing recombination centers and in particular catalysts that are involved in water splitting reaction are expected to have good crystallinity. This is a fascinating preparation for wide variety of materials with excellent catalytic activities. The most attractive feature of this preparation method is that there is no need of any purification treatment required as well as high thermally stable catalysts. High thermal stability arises due to its preparation at high temperatures and generally they withstand harsh high temperature as well as pressure conditions adopted in real-world catalysis.

Relatively speaking combustion synthesis takes place at rapid kinetics. Due to the fast kinetics some disadvantages are also present, such as particle size, textural properties may not be controlled to the fullest desired extent. However, by varying the preparation parameters such as, different starting materials with same cations, different fuels, one is able to tune the material characteristics within a certain range. The combustion synthesis is an energy efficient process and requires simple instrumental facility of muffle furnace. The reaction takes place in a furnace chamber

that is preheated to the desired high temperature sufficient for the complete combustion of reactant mixture [8].

At elevated temperature, the water was evaporated first and the mixture becomes compact followed by a self-ignition route. After the combustion process takes place, the precursor materials are converted into fine crystallites accompanied with the evolution of plenty of gases. The reaction time and mode takes major role in deciding the growth of the crystallites either into bulk form or nanoparticles form. Also as the synthesis procedure is growing material particle from solution state, thus foreign atoms are easily incorporated into lattice. We introduced vanadium and manganese into the TiO_2 lattice positions. Same size cations with similar charge, as that of host cation, can only be introduced into the lattice. Similar charge makes the resulting material suitable for redox reactions, often encountered in catalysis. Also synthesis procedure is also growing material particle from solution state [9, 10].

2.1.2 Reduction Method

Hydrogen is a very small molecule, under high temperature and high pressure conditions when materials are treated with hydrogen gas, they are incorporated into the lattice, reduce the native lattice ions (cations). Because of reducing nature hydrogen atoms will create O vacancies, dangling bonds on the surface, hydrogen bond on surface. Surface of a perfectly crystalline material will get affected after hydrogen treatment [11]. We prepared materials by reducing under hydrogen atmosphere, reduction conditions were varied i.e. temperature and pressure of gas inside the autoclave. Catalysts are prepared at higher temperatures of 250, 300, and 400 °C under ambient hydrogen pressure and they are given codes of 25AP, 30AP and 40AP, respectively. 20 bar pressure was applied at 200 ^{0}C to understand the influence of high pressure treatment and it is termed as 20B.

Reduction of some amount of Ti^{4+} to Ti^{3+} is advantageous in terms of different catalyst and hence catalysis. When activities are evaluated, reduced catalyst shows better values than the pristine virgin catalyst [12]. Color of the materials changed drastically after treatment, indicating the generation of new species. Best methods for self doping i.e. Ti^{3+} species generation, materials were analyzed via other techniques also. Reduced materials show long term stability, and no change in color was observed even after six months.

2.1.3 Incipient Wet Impregnation Method

The impregnation method is useful to physically bind two materials. One of the components is taken as major constituent and act as support. There are two types of impregnation methods, namely dry impregnation method and incipient wet impregnation method. The dry method is that the gaseous vapor of minor component is sprayed over the major component. This method is very fast method and require small amount of components. The disadvantage associated with the method is that the nanomaterials are generally not dispersed well and the clusters are agglomerated. The interaction between the components remains poor due to poorly embedded minor components on the surface of major component [13].

The wet impregnation method is that the support material is suspended in aqueous solution of minor component. The selection of solvent is based in such a way that support is to be in the suspended state and the minor component is to be in well dissolved state. This method is advantageous for better dispersion of nanomaterial over the support and that is expected to help the photocatalysis for easy light penetration. The nanoparticle of the minor constituent is nucleating and growing into clusters on the support and thus, the nanoparticles is deeply buried into the matrix creating composites with fairly bound components. We prepared catalysts for ODH analysis by incipient wet impregnation, 5% Mn_3O_4 over TiO_2 [14].

2.2 Catalytic Activity Studies

Catalytic studies of material for various thermal conversions, photocatalytic processes were evaluated. Sulfide oxidation, ethylbenzene oxidative dehydrogenation, hydrogen evolution were analyzed and solar conversion techniques. The descriptions on the reactor designs followed by the details on reaction conditions of catalytic studies are given.

2.2.1 Sulfide Oxidation

Sulfide oxidation to sulfoxides was carried out in a batch reactor under continuous stirring. Liquid phase sulfoxidation was carried out in a round bottom flask (RBF), attached with a condenser. Fresh catalyst (50 mg), 30% H_2O_2 (1.5 mmol) used as oxidant for supplying oxygen, at 1.5 equivalent to substrates, different sulfide

substrates (1 mmol) were added into the RBF. Reactions were carried out at different temperatures, including sub-ambient temperatures. Reaction mixtures were collected after 6 h and analyzed via Agilent gas chromatograph (6890 N) equipped with an HP 5.5% phenyl methyl siloxane column and a flame ionization detector (FID). Products were also analyzed by using GC–MS. Acetonitrile was the solvent employed in all reactions [15].

2.2.2 Oxidative Dehydrogenation

The catalytic activity was evaluated using a continuous flow fixed bed reactor (FBR) having two furnace zones over a temperature range of 430–570 °C at atmospheric pressure (atm.). An inconel reactor tube with 13mm internal diameter and 510 mm length was used to pack the catalyst. Reactor system was prepared via settling a column of ceramic beads where sieved catalysts bed (1 mL or 0.76±0.04 g) is placed in the middle of reactor with quartz wool packed in the spaces on either side of the bed. Prepared catalysts pellet of 0.8 mm mesh size was filled into the reactor. The reactant flow was configured to operate in up-flow mode and the products were condensed using a chiller. The temperature on the wall of the reactor and in the catalyst bed was measured using a K-type coaxially centered thermocouple. EB flow was controlled using a high precision isocratic pump (Lab Alliance Series II) and the oxygen flow was controlled using a Brooks-make mass flow controller (5890 E series). Samples of reaction mixture were collected at regular interval via cold trap into vials; collected samples were then analyzed using an Agilent 6890N gas chromatograph with a BP-5 (5.5% phenyl methylsiloxane) column along with an FID detector. The optimized conditions for the reactions were: 500 – 530 °C, atmospheric pressure, LHSV (liquid hourly space velocity) of 1.8 h^{-1} with respect to EB, and air flow at GHSV (gas hourly space velocity) 10800 h^{-1}, i.e. O_2/EB molar ratio of 2.0. Liquid and gaseous products analysis was carried out separately. EB conversion, styrene selectivity and yield has been calculated from the GC analysis results and discussed in chapter 4, all data points were obtained in duplicate with an error of ±2% [16].

Figure 1. Multi fixed bed flow reactor on which ethylbenzene to styrene with $Mn_xTi_{1-x}O_2$ catalysts were studied.

2.2.3 Hydrogen Production via Water Splitting

Hydrogen production was studied for evaluation of photocatalytic activity of prepared H-TiO_2 materials. Catalysts were used under different light sources such as UV-Vis., and AM1.5. 20 mg catalyst was taken in quartz RB followed by sonication and degassing in argon gas to remove any dissolved oxygen; after this treatment, the solution was irradiated with required wavelength range photons. Water and methanol mixtures were used for hydrogen production [17]. Reactions were carried out via stirring the solution and collecting the hydrogen produced via water reduction in the presence of methanol electron donor. Gases were collected periodically via gas tight syringe over a reaction period of 6 h, and were analyzed by Agilent gas chromatograph (7890 N) equipped with a Carbo Sieve S-II packed column and a thermal conductivity detector.

2.2.4 Inorganic Solar Cell Fabrication

TiO_2 paste was prepared for different titania powders samples following method in literature [18]. Anode electrodes were fabricated with H-TiO_2 materials for solar cells. FTO glass plates were cleaned in a detergent solution using an ultrasonic bath

for 30 min and rinsed with water and ethanol. The FTO glass plates were immersed in 40mM $TiCl_4$ (aqueous) at 70°C for 30 min and washed with water and ethanol. The photoanode was prepared by doctor blade method using the TiO_2 paste on FTO plate. The TiO_2 electrodes were gradually heated under an air flow at 325°C for 5 min, at 375 °C for 5 min, at 450 °C for 15 min, and at 500 °C for 15 min. A paste of TiO_2 for the scattering layer containing 400 nm sized anatase TiO_2 particles was deposited by doctor blade printing on photo anode and again gradually heated under an air flow at 325 °C for 5 min, at 375 °C for 5 min, at 450 °C for 15 min, and at 500 °C for 15 min. The photo anodes were treated again by $TiCl_4$ at 70 °C for 30 min and sintered at 500 °C for 30 min. The working electrode was composed of a 12-13µm thick TiO_2 film (active area 0.16 cm^2), composed of an 8-9 µm layer with H-TiO_2 particle and a 4-5 µm scattering layer composed of 400 nm sized TiO_2 particles. The dye solutions were prepared with N719 dye in methanol. 0. 5 mM concentration of N719 dye in methanol was prepared. The photo anodes underwent dipping for different time interval to complete the loading with sensitizer. The dye-adsorbed TiO_2 electrode and Pt-counter electrode were assembled into a sealed sandwich-type cell by heating at 100 °C for 10 min. A drop of electrolyte solution (electrolyte of 0.6 M 1,2-dimethyl-3-propylimidazolium iodide, 0.05 M I_2, 0.1 M LiI, and 0.5 M tert-butylpyridine in acetonitrile) was poured in to the counter electrode of the assembled cell [19-21]. Completed solar cells were kept under solar simulator and different analyses were done (JV plot, impedance measurement).

2.3 Physiochemical Characterization Methods

2.3.1 Introduction

To understand the material we have to analyze materials with various physiochemical techniques such as PXRD, surface area determination by BET method, UV-Visible spectroscopy (DRS), DRIFTs, X-Ray photoelectron spectroscopy(XPS), Raman spectroscopy, transmission electron microscopy, scanning electron microscopy (SEM), energy dispersive analysis of X-rays (EDAX), LSV, CV, NMR, thermo gravimetric analysis (TGA) etc. Instrumentation and experimental methods for these techniques are explained in detail below.

2.3.2 Theory and Experimental Procedures

2.3.2.1 X-Ray Diffraction

Powder X-ray diffraction (PXRD) data were collected from PANalytical X'pert Pro dual goniometer diffractometer. A proportional counter detector was used for low angle experiments. The data point were collected with a step size of 0.02° and a scan rate of 0.5°/min. The sample was spun slowly throughout the scan for better counting statistics. The radiation used was Cu K α (1.5418 Å) with Ni filter and the data collection was carried out using a sample holder in Bragg–Brentano geometry [22]. Scherrer equation is used to calculate particle sizes of crystallites. The equation is:

$$\tau = \frac{K\lambda}{\beta \cos\theta}$$

where:

$\boldsymbol{\tau}$ is the mean size of the ordered (crystalline) domains, which may be smaller or equal to the grain size;

$\boldsymbol{K}$ is a dimensionless shape factor, with a value close to unity. The shape factor has a typical value of about 0.9, but varies with the actual shape of the crystallite;

$\boldsymbol{\lambda}$ is the X-ray wavelength;

$\boldsymbol{\beta}$ is the line broadening at half the maximum intensity (FWHM), after subtracting the instrumental line broadening, in radians. This quantity is also sometimes denoted as $\Delta(2\theta)$;

$\boldsymbol{\theta}$ is the Bragg angle.

2.3.2.2 Nitrogen Physisorption

Nitrogen adsorption/desorption isotherms for the materials were obtained from quantachrome autosorb automated gas sorption system (NOVA 1200). The Brunauer–Emmett–Teller (BET) equation was used to calculate the surface area from the adsorption branch. The pore size distribution was calculated by analyzing the adsorption branch of the nitrogen sorption isotherm using Barrett–Joyner–Halenda (BJH) method [23-24]. BET is based on the physical adsorption of gases on the material surface. The equation is:

$$\frac{1}{V_a\left(\frac{P_0}{P}-1\right)} = \frac{C-1}{V_m C} * \frac{P}{P_0} + \frac{1}{V_m C} \quad \ldots\ldots\ldots \quad \text{eq 1.}$$

Where P and P_0 are the equilibrium and the saturation pressure of adsorbates at the temperature of adsorption, V is the adsorbed gas quantity (for example, in volume units), and V_m is the monolayer adsorbed gas quantity. C is the BET constant,

$$C = \exp\left(\frac{E_1 - E_L}{RT}\right)$$

Where E_1 is the heat of adsorption for the first layer, and E_L is that for the second and higher layers and is equal to the heat of liquefaction.

Equation 1 is an adsorption isotherm and can be plotted as a straight line with $\frac{1}{V_a\left(\frac{P_0}{P}-1\right)}$ on the y-axis and $\phi = \frac{P}{P_o}$ on the x-axis according to experimental results. This plot is called a *BET plot*. The linear relationship of this equation is maintained only in the range of $0.05 < \frac{P}{P_o} < 0.35$. The value of the slope A and the y-intercept I of the line are used to calculate the monolayer adsorbed gas quantity V_m and the BET constant C. The following equations can be used:

$$V_m = \frac{1}{A + I}$$

$$C = 1 + \frac{A}{I}$$

The BET method is widely used in surface science for the calculation of surface area's of solids by physical adsorption of gas molecules. The total surface area S_{total} and the specific surface area S_{BET} are given by

$$S_{total} = \frac{(V_m N s)}{V},$$

$$S_{BET} = \frac{S_{total}}{a}$$

where:

$\boldsymbol{V_m}$ is in units of volume which are also the units of the molar volume of the adsorbate gas,

$\boldsymbol{N}$ is avogadro's number,

$\boldsymbol{s}$ the adsorption cross section of the adsorbing species,

$\boldsymbol{V}$ the molar volume of the adsorbate gas, and

$\boldsymbol{a}$ is the mass of the solid sample or adsorbent.

2.3.2.3 UV-Visible Spectroscopy (DRS)

UV-Visible Spectroscopy of powder materials doesn't show specular reflection as shown in figure 2, thus uv-visible measurements were carried out in diffuse reflectance mode (DRS). UV visible reflectance measurements were carried out on Shimadzu spectrophotometer UV2700 [25].

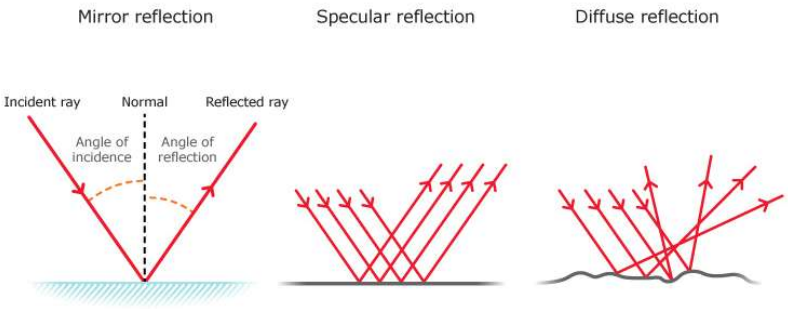

Figure 2.showing specular reflection and diffuse reflection over different surfaces.

A Tauc plot is used to determine the optical gap, or Tauc gap, in semiconductors. The Tauc gap is often used to characterize practical optical properties of powder materials.

$$\alpha h\upsilon = A(h\upsilon - E_g)^{\frac{1}{n}}$$

h, Planck's constant,

v, frequency of vibration,

α, absorption coefficient,

Eg, band gap,

A, proportional constant.

The value of the exponent ***n*** denotes the nature of the sample transition

For direct allowed transition, ***n*** = 1/2

For direct forbidden transition, ***n*** = 3/2

For indirect allowed transition, ***n*** = 2

For indirect forbidden transition, ***n*** = 3

2.3.2.4 DRIFTs

Diffuse Reflectance Infrared Fourier Transform spectroscopy means a special technique of infrared spectroscopy. DRIFTs powder materials dosen't show specular reflection rather than diffuse reflection. DRIFT'S studies the surface chemistry of high surface area powders, notably for heterogeneous catalysis, where the temperature

and environment of the catalyst can be controlled in-situ in the DRIFTS cell. DRIFT measurements were carried out on Shimadzu make FTIR-8201PC [26]. The particle size should be smaller than the wavelength of the incident light, so this would infer that it should be less than 5 μm for mid-range infrared spectroscopy.

Alternative plots of Kubelka-Munk units can be used, which relate reflectance to concentration using a scaling factor, expressed in linear units Kubelka-Munk roughly correspond to absorbance in transmission KBr pellet technique.

$$f(R) = \frac{(1 - R_\infty)^2}{2R\infty} = \frac{k}{s}$$

Where:

f(R)… is called Kubelka-Munk function

$\boldsymbol{R\infty}$ … absolute reflectance of the sampled layer

k… molar absorption coefficient

a … absorptivity - proportional to the fraction of transmitted light

s … diffusion (scattering) coefficient - proportional to the fraction of diffused light

2.3.2.5 Raman Spectroscopy

Raman spectra were recorded on a Horiba JY LabRAM HR 800 Raman spectrometer coupled with microscope in reflectance mode with 633 nm excitation laser source and a spectral resolution of 0.3 cm^{-1} [27].

2.3.2.6 X-ray Photoelectron Spectroscopy

XPS measurements were performed in a laboratory based custom built ambient pressure photoelectron spectrometer (APPES from Prevac, Poland) under UHV condition. XPS measurements were made with Mg Ka X ray source for X-ray generation and R3000HP (VG Scienta) analyzer for energy analysis [28].

$$E_{binding} = E_{photon} - (E_{kinetic} + \phi)$$

Where:

$\boldsymbol{E_{binding}}$ is the binding energy (BE) of the electron,

$\boldsymbol{E_{photon}}$ is the energy of the X-ray photons being used,

$\boldsymbol{E_{kinetic}}$ is the kinetic energy of the electron as measured by the instrument and

$\boldsymbol{\phi}$ is the work function dependent on both the spectrometer and the material.

This equation is essentially a conservation of energy equation. The work function term $\boldsymbol{\phi}$ is an adjustable instrumental correction factor that accounts for the few eV of

kinetic energy given up by the photoelectron as it becomes absorbed by the instrument's detector. It is a constant that rarely needs to be adjusted in practice.

2.3.2.7 Transmission Electron Microscopy

A FEI TECNAI 3010 electron microscope operating at 300 kV (Cs = 0.6 mm, resolution 1.7 Å) was used for recording high resolution transmission electron microscope (HRTEM) of all materials. Samples were crushed and dispersed in isopropanol before depositing onto a holey carbon grid [29]. Different X-rays and electrons generated by interaction with the matter are shown in the diagram.

2.3.2.8 Scanning Electron Microscope

SEM-Energy Dispersive Analysis of X-rays (EDAX) measurements were carried in SEM system (FEI, Model Quanta 200 3D) equipped with EDX attachment. EDX spectra were recorded in the spot-profile mode by focusing the electron beam onto specific regions of the sample [30].

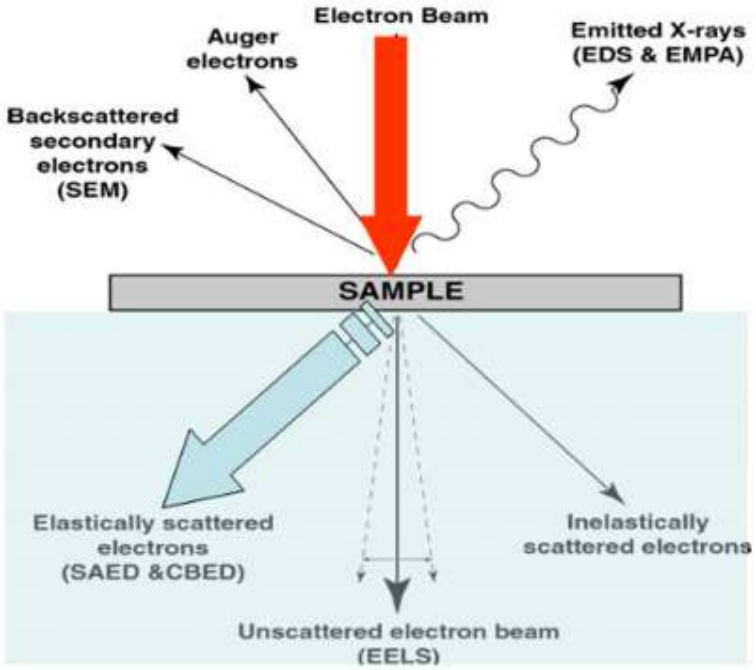

Figue 3, Interaction of incident electron rays on matter, generating various x rays and electrons.

2.3.2.9 Thermo Gravimetric Analysis

TGA to understand the coke deposition or change in catalyst we have done gravimetric analysis. Thermal analyses of these adducts were conducted on Perkin–Elmer Diamond's thermogravimetry (TG) and differential thermal analysis (DTA) using alumina as the internal standard [31].

2.3.2.10 Linear Sweep Voltammetry

LSV to monitor the change in current, this technique is used using the principle of voltammetric method in a conventional three electrode system immersed in the electrolyte bath. The current of the working electrode is measured while the potential between reference electrode and counter electrode are sweeping from positive potential to negative potential. Linear sweep voltammogram is the half the cycle of the cyclic voltammetry and redox potential of the elements in the catalyst can be identified. In case of photocurrent generation experiment, the catalyst should not be allowed to undergo both oxidation and reduction reactions because faradiac current should not be confused with the current generated by the conversion of light energy absorbed into excited electron/hole carriers. The window of the potential sweep is to maintain in the range that does not cause corrosion of the catalyst [32].

2.3.2.11 Chronoamperometry

This technique is used to analyze the sustainability of the current generation over a period of time. In case of electrochemical applications, the change concentration of electroactive species with respect to time or in other words, the reaction kinetics is monitored using chronoamperometry technique. However, in case of photocatalytic applications, the photocurrent generation is expected only due to the photofunctional behavior not the faradiac process. In that case, the plot of current Vs time is done along with the light irradiating shutter on/off operations. When the shutter for light irradiation is opened, current rises and maintains at the same value. The value of current generation drops on closing of the shutter [33]. Chronoamperometric studies were carried over Gamry 300 reference potensiostat.

2.3.2.12 Photoluminescence Spectroscopy

PL spectroscopy is a complimentary technique to UV-Visible spectroscopy that gives information on the electronic structure from the emission process (fluorescence) of the excited electron to the ground state [34]. Photoluminescence (PL) measurements

were performed using Horiba Jobin Yvon Fluorolog 3 spectrophotometer with a 450 W xenon lamp at room temperature under the excitation light of 330 nm. The conditions are maintained to compare the photocatalytic conditions.

2.3.2.13 JV plot

JV plot were measured on Photo emission technology inc. (PET) instruments solar simulator model #CT200AAA, Jsc and Voc shows the maximum current, maximum voltage that can be drawn from the cell at short circuit and open circuit condition respectively [35]. Series and shunt resistance were calculated correspondingly at Voc and Jsc. Maximum power output of the cell is denoted by Fill factor, which is ratio of actual power output to theoretical maximum power output of solar cell. Solar energy conversion efficiency of the cell is also calculated from the plot [36].

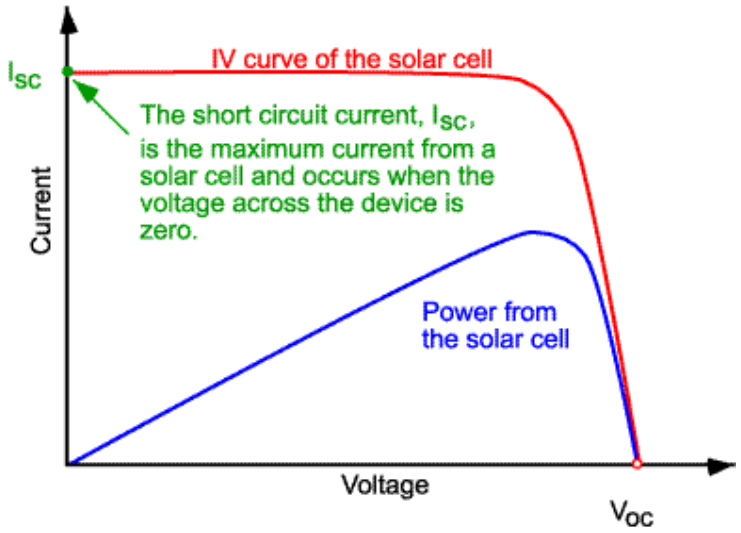

Figure 4. Typical JV plot for solar cells, showing various characteristics parameters of the cell [37].

2.3.2.14 Electrochemical Impedance spectroscopy

EIS was done on Bio-Logic make SP-300 instrument to understand ionic and electronic processes in DSSC. Frequency response of the device is recorder. High frequency response is attributed to the charge transfer at the counter electrode while intermediate frequency response is attributed to electron transport in the mesoporous TiO_2 film and TiO_2/electrolyte interface. The low frequency region reflects for diffusion in the electrolyte. Electron transport rate and electron lifetime are measured

for the device. Bias potential studies were done at 0.5, 0.6, and 0.7 V. to calculate the resistance at various barriers [38].

2.4 Conclusion

Characterization methods were summarized in this chapter. The aspects of preparation methods, reaction conditions, experimental reactor set up are explained in detail. The plausible mechanism for the formation of the product is also described with suitable illustration. The characterization methods which are adopted in thesis chapters are summarized along with instrumental conditions.

2.5 References

1. K. S. Thushara, R. Mathew, T. G. Ajithkumar, P. R. Rajmohanan, S. Bhaduri, C. S. Gopinath, *J. Phys. Chem. C*, (2009) ***113*** 8556–8559.
2. K. Sivaranjani, C. S. Gopinath, *J. Mater. Chem.*, (2011) **21** 2639-2647.
3. M Götz, H. Wendt, *Electrochemica Acta,* (1998) **43** 3637–3644.
4. X. Chen, L. Liu, P. Y. Yu, S. S. Mao *Science,* (2011) **331** 746-750.
5. T. Rajesh, A. K. Rajarajan, C. S. Gopinath, R. N. Devi, *J. Phys. Chem. C*, (2012) **116** 9526–9532.
6. A. S. Prakash, P. Manikandan, K. Ramesha, M. Sathiya, J-M. Taracson, A. K. Shukla, *Chem. Mater.*, (2010) ***22*** 2857–2863.
7. *K.* Sivaranjani, S. Agarkar, S. B. Ogale, C. S. Gopinath, *J. Phys. Chem. C*, (2012) **116** 2581–2587.
8. M. Mapa, C. S. Gopinath, *Chem. Mater.*, (2009) **21** 351–359.
9. S. S. Negi, A. T. Venugopalan, T. Raja, A. P. Singh and C. S. Gopinath, *RSC Adv.*, (2014) **4** 57087-57097.
10. S. S. Negi, K. Sivaranjani, A. P. Singh, C. S. Gopinath, *App. Catal. A: General,* (2013) **452** 132– 138.
11. S. Wendt, P. T. Sprunger, E. Lira, G. K. H. Madsen, Z. Li, J. Hansen, J. Matthiesen, A. B. Rasmussen, E. Laegsgaard, B. Hammer, F. Besenbacher, *Science,* (2008) **320** 1755-1759.
12. S. Hoang, S. P. Berglund, N. T. Hahn, A. J. Bard, C. B. Mullins, *J. Am. Chem. Soc.,* (2012) **134** 3659−3662.

13. Y. Tao, S. Schwartz, C. Y. Wu, D. W. Mazyck, *Ind. Eng. Chem. Res.,* (2005) **44** 7366-7372.
14. D. P. Debecker, M. Stoyanova, U. Rodemerck, E. M. Gaigneaux, *J. Molecular Catal. A: Chemical,* (2011) **340** 65–76.
15. V. Ayala, A. Corma, M. Iglesias, F. Sanchez, *J. Molecular Catal. A: Chemical,* (2004) **221** 201–208.
16. K. Sivaranjani, A. Verma, C. S. Gopinath, *Green Chem.*, (2012) **14** 461–471.
17. K. Sivaranjani, S. RajaAmbal, T. Das, K. Roy, S. Bhattacharyya, C. S. Gopinath, *ChemCatchem*, (2014) **6** 522-530.
18. S. Ito, P. Chen, P. Comte, M. K. Nazeeruddin, P. Liska, P. Pechy, M. Gratzel, *Photovolt: Res. Appl.*, (2007) **15** 603–612.
19. K. Sivaranjani, S. Agarkar, S. B. Ogale, C. S. Gopinath, *J. Phys. Chem. C*, (2012) **116** 2581–2587.
20. M. Grätzel, *J. Photochem. and Photobio. A: Chemistry,* (2004) **164** 3–14.
21. M. M. Lee, J. Teuscher, T. Miyasaka, T. N. Murakami, H. J. Snaith, *Science,* (2012) **338** 643-647.
22. J. L. V. Heerden, R. Swanepoel, *Thin Solid Films*, (1997) **299** 72–77.
23. S. Brunauer, P. H. Emmett, E. Teller, *J. Am. Chem. Soc.*, (1938) **60** 309–319.
24. E. P. Barrett, L. G. Joyner, P. P. Halenda, *J. Am. Chem. Soc.*, (1951) **73** 373–380.
25. X. Gao, I. E. Wachs, *J. Phys. Chem. B*, (2000) ***104*** 1261–1268.
26. D. Gamarra, A. Martinez-Arias, *J. Catal.* (2009) **263** 189–195.
27. N. Colthup, *Introduction to infrared and Raman spectroscopy*. Elsevier Chicago (2012).
28. K. Roy, C. S. Gopinath, *Anal. Chem.*, (2014) **86** 3683–3687.
29. X. Nie, E. I. Meletis, J. C. Jiang, A. Leyland, A. L. Yerokhin, A. Matthews, *Surface and Coatings Technology,*(2002) **149** 245–251.
30. A. Laskin, J. P. Cowin, *Anal. Chem.*, (2001) ***73*** 1023–1029.
31. Y. Chen, S. mori, W. P. Pan, *Thermochimica Acta.* (1996) **275** 149–158.
32. L. Nadjo, J. M. Saviant, *Electroanalytical Chemistry and Interfacial Electrochemistry*, (1973) **48** 113- 145.
33. J. M. Saveant, E. Vianello, *Electrochimica Acta*, (1965) **10** 905-920.
34. S. A. Empedocles, D. J. Norris, M. G. Bawendi, *Phy. Rev. Lett.*, (1996) **77** 3873-3876.

35. J. D. Servaites, M. A. Ratner, T. J. Marks, *Energy Envir. Sci.,* (2011) **4** 4410-4422.
36. L. Tao, Z. Huo, Y. Ding, Y. Li, S. Dai, L. Wang, J. Zhu, X. Pan, B. Zhang, J. Yao, M. K. Nazeeruddin, M. Gratzel, *J. Mater. Chem. A*, (2015) **3** 2344–2352.
37. http://www.pveducation.org/pvcdrom/solar-cell-operation/short-circuit-current
38. F. F. Santiago, J. Bisquerta, G. G. Belmonte, G. Boschloo, A. Hagfeldt, *Solar Energy Materials & Solar Cells,* (2005) **87** 117–131.

Chapter III: Disordered Mesoporous $V_xTi_{1-x}O_2$ System for Ambient Oxidation of Sulfides to Sulfoxides

3.1 Introduction

The oxidation reaction in organic chemistry is an omnipresent transformation, and several oxidizing agents are available to effect this conversion [1–6]. In the mainstream of industrial organic oxidation reactions, the use of toxic or hazardous inorganic oxidants, such as persulfate, bromate, and particularly metal reagents such as chromic acid and permanganate entails cumbersome and demanding isolation and purification procedures. As a result, safer and simple protocols are required, [7] towards selective products, such as the efficient conversion of sulfide to sulfoxides [8,9]. Various oxidizing agents are being used for oxidation purpose, and unfortunately, most of them are not satisfactory for medium to large scale operations for several reasons. Some of them exhibit a low content of effective oxygen for the oxidation, generation of environmentally unfavorable by products and high cost [10]. In this direction, use of aqueous hydrogenperoxide as oxidizing agent is highly preferred as it is an environmentally benign oxidant [11,12]. We report on H_2O_2/V–TiO_2 system that can be used for efficient and selective oxidation catalysis for a wide range of sulfides under ambient conditions. The route for the synthesis of sulfoxides is shown in Scheme 1 Selective oxidation of sulfide to sulfoxides remains a challenge and is of interest because of the importance of sulfoxides and sulfone as synthetic intermediates towards the synthesis of various pharmaceutical and agrochemical products such as, sulfolane, sulfolene, bisphenol S (BPS) and biologically active molecules, e.g. dapsone, (sodium glucosulfone) promin, esomeprazole and armodafinil [13–17]. Several catalysts such as; $Sc(OTf)_3$, vanadyl complexes of N-salicylidene-amino acids have been utilized for oxidation of sulfides by aqueous H_2O_2. While oxidation of sulfide to sulfoxide/sulfone requires long reaction time (24 h) [18–20] at RT and 328 K and lengthy treatment with the use of toxic materials such as homogeneous heavy metal salts e.g. H_2WO_4, CH_3ReO_3, 2-$NO_2C_6H_4SeO_2H$, Na_2MoO_4 + $(n\text{-}C_4H_9)_3PO$ [21]. Indeed oxidation of sulfide to sulfoxides/sulfone constitutes an active research on its own, particularly with the emphasis on ‘green chemistry’ [22]. Textural properties are one of the most important properties of heterogeneous catalysts that govern the adsorption, desorption and diffusion [23]. Not only the surface reactivity but also the mass transfer of reactants and products can be tuned by modifying the pore structure. Generating porosity in metal oxides by different synthesis procedure is generally aimed at the production of materials with

enhanced or very large surface area. In contrast to ordered hexagonal mesoporous materials [24], disordered mesoporous materials have pore depth of few nanometres (usually <10 nm) and hence reactants and products can easily diffuse to and from the active sites [25]. These types of disordered mesoporous materials are known as pseudo 3D (p3D) mesoporous materials. This disordered p3D framework provides an easy route for the diffusion of reactants due to less diffusion barriers. Isolated vanadium is a prerequisite for the selective partial oxidation reactions. Using solution combustion method we were able to introduce vanadium into the disordered mesoporous titania lattice framework [26]. Presence of isolated V^{5+} has been identified by physicochemical methods. Hydrogen peroxide has been employed as a benign oxidizing agent [27] for sulfoxidation of sulfides with V/TiO_2 and H_2O_2. Indeed this reaction requires small reaction time at ≤RT, and stable and high product yield has been obtained. To extend the scope of the reaction and to generalize the procedure, we investigated the sulfoxidation of diaryl, dialkyl and sulfides under wide reaction conditions. Both sulfides bearing electron-donating and electron-withdrawing substituents gave the desired sulfoxides in high yields at ambient conditions.

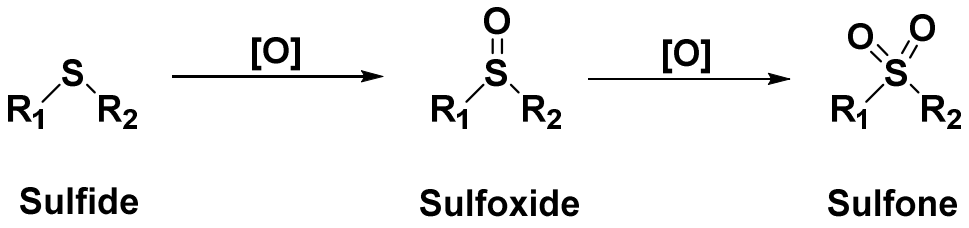

Scheme 1. Sulfide oxidation to corresponding sulfoxide and sulfone.

3.2 Results and Discussion

3.2.1 X-Ray Diffraction

Structural features of the vanadium incorporated mesoporous titania$Ti_{1-x}V_xO_2$ materials were explored by PXRD. PXRD pattern of as prepared materials are shown in Fig. 1 at low angle and wide angle. PXRD pattern of $Ti_{1-x}V_xO_2$ materials could be indexed to anatase phase of titania with small amount of rutile phase (JCPDS file 21-1272, 21-1276). No vanadium oxide peak was observed for any of the $Ti_{1-x}V_xO_2$ materials. Broad peaks observed in wide angle XRD suggests nanocrystallanity of TVx material. Crystallite size was calculated from Debye–Scherrer equation, for all

TVx material and shown in Table 1. Crystallite sizes observed to be around 7 nm are irrespective of V-content. Similarly, all TVx materials exhibit a pore diameter of about 5 nm. A peak in low angle XRD around 2θ = 0.8° confirms the disordered mesoporous nature of $Ti_{1-x}V_xO_2$. Like conventional ordered mesoporous materials no higher ordered peaks are observed for disordered TVx materials.

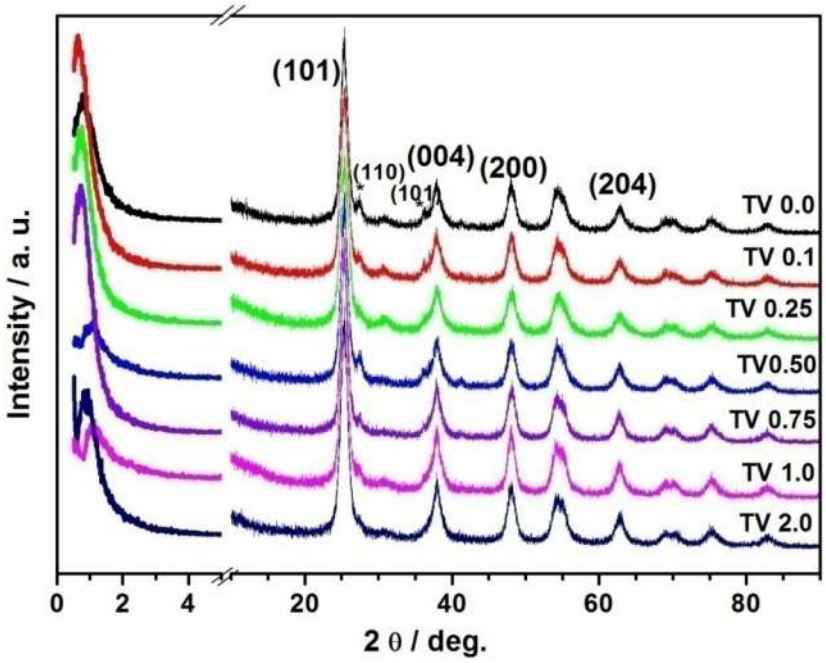

Figure 1. Low and Wide angle XRD pattern of $Ti_{1-x}V_xO_2$(TVx) materials. Rutile features are denoted by #.

3.2.2 Energy Dispersive Analysis of X-rays

SEM analysis of $Ti_{1-x}V_xO_2$ catalysts were carried out to find the V-distribution and composition of $Ti_{1-x}V_xO_2$materials. EDX analysis is shown for TV1.0 in Fig. 2 with colour coding for different elements. Fig. 2a shows the distribution of all three elements (Ti, O and V) in a uniform manner. Small and uniform yellow dots indicates the distribution of V. Fig. 2b show the vanadium and titanium mapping of TV1.0 to show the homogeneous distribution over a large area confirming uniform distribution of, vanadium at the microscopic level for the series of material prepared. To understand the textural properties of the $Ti_{1-x}V_xO_2$ materials, N_2 adsorption–desorption studies has been carried out. N_2physisorption results and BJH pore size

distribution are shown in Fig. 3. Pore size and surface area for the TVx materials is calculated and shown in Table 1. All materials show type IV adsorption–desorption isotherm with typical H2 hysteresis loop characteristic of disordered mesoporous material. Bimodal pore size distribution was observed in the mesoporous regime from BJH plot for $Ti_{1-x}V_xO_2$ materials.

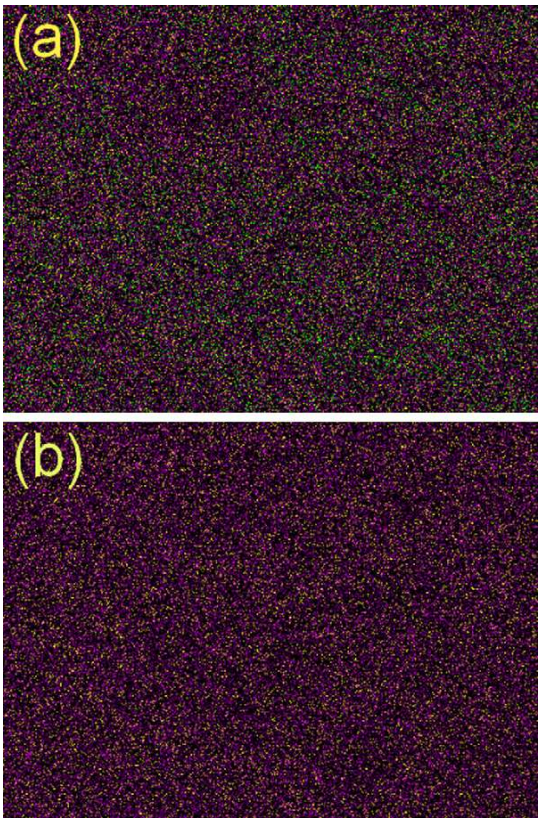

Figure 2. Representative elemental mapping of TV1.0 (O – green, V – yellow, Ti – pink) by EDX. A uniform distribution of vanadium could be seen over 1 × 1.3 mm^2.

3.2.3 Raman Spectroscopy

Fig. 5 shows the Raman spectra of TVx materials. Raman spectrum of V_2O_5 was also recorded and shown in Fig. 5 for comparison. All six Raman active fundamental modes for anatase phase are observed viz. 145 (Eg), 198 (Eg), 398 (B1g), 516 (A1g + B1g), 640 (Eg) cm^{-1} in Fig. 5 [20,26]. Broad Raman features confirms the nanosize crystallites. Even though amount of vanadium doping is upto 2%, no V–O feature was observed in Raman spectra, as well as in XRD, suggests a homogeneous V-doping in

TiO_2lattice. Likely the incorporation and distribution of vanadium into the lattice is very high and hence no features that corresponds to V_2O_5 (285, 703, and 997 cm^{-1}) was observed in Raman spectra of TVx materials. Particularly, the intensity of all the Raman features decreased drastically up to an order of magnitude, with increasing V-content. This decrease in the peak intensity is attributed to the symmetry breaking of TiO_2 lattice due to the incorporation of vanadium. This symmetry breaking could occur only if vanadium was incorporated into the titania lattice. Further, a characteristic blue shift in Eg band is observed from 145 to 154 cm^{-1}on introducing V into the titania lattice, indicating a structural distortion. Due to the small V-doping percentage (≤2%), the probability of finding two V atoms in the nearneighbor environment is very less and this leads to monomeric vanadium species from the present preparation conditions.

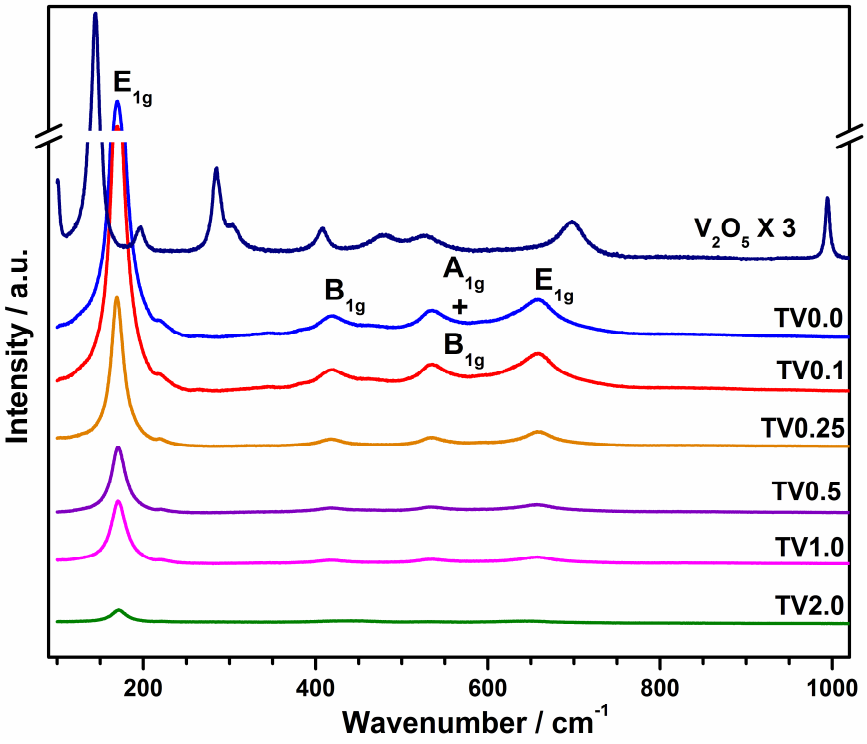

Figure 3. Raman spectra of TVx materials. V_2O_5 spectral data is given for comparison. Note the blue shift in Eg from 145 to 154 cm^{-1} upon V introduction into the titania lattice.

3.2.4 Transmission Electron Microscopy

Particle morphology and textural properties of TVx catalysts has been studied carefully by HRTEM. Representative HRTEM images recorded for $Ti_{1-x}V_xO_2$ materials (x = 0.0, 0.25, 0.5 and 1.0) are shown in Fig. 4. All $Ti_{1-x}V_xO_2$materials exhibit spherical morphology with particle diameter in the range of 8–10 nm. It is to be noted that the particle size remains the same irrespective of V-doping. Disordered (or wormhole like) mesopores can be seen in all TEM images. It is likely that the disordered mesoporosity arises due to intergrowth of fundamental particles and the same leads to aggregates with significant extra framework void space [28,29]. It is also to be noted that a predominant (101) faceted particles are observed with lattice fringes corresponding to (101) (d(101) = 0.352 nm) crystallographic planes of anatase phase. Selected area electron diffraction pattern (SAED) shows the crystalline nature of $Ti_{1-x}V_xO_2$materials and (101) diffraction pattern is observed predominantly.

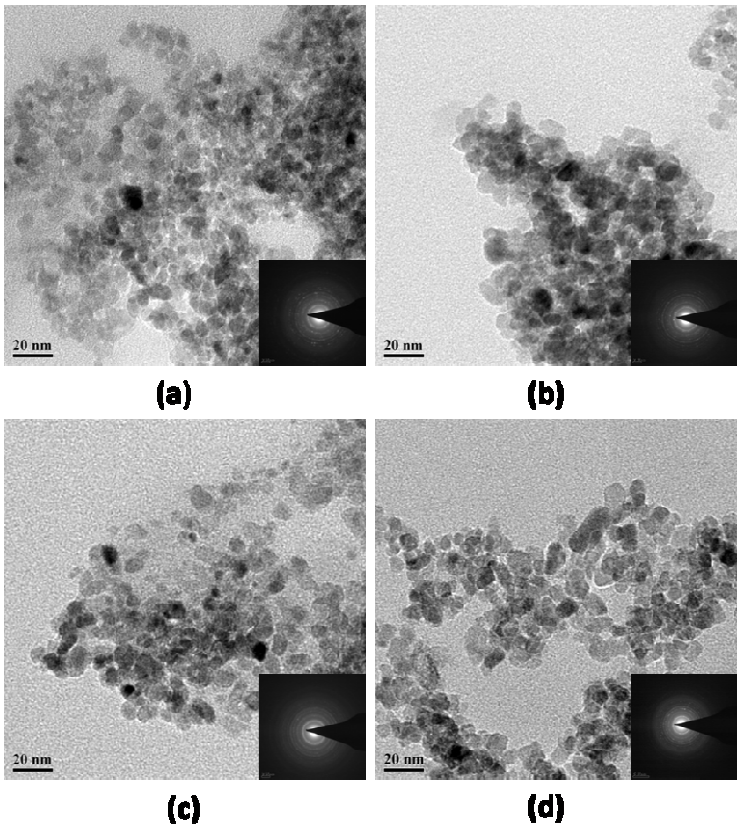

Figure 4. TEM image of (a) TiO_2 (b) TV0.5 (c) TV0.25 and (d) TV1.0. SAED is given in inset.

These observations are in excellent agreement with XRD as well as with N_2 adsorption isotherm results. Similar disordered mesoporous phosphate titania has been prepared using coblock polymers as template [30]; however, no such templating agents has been used in the present preparation method is to be underscored. Further, such disordered mesoporous nature also exhibit advantages, such as low diffusional barriers for reactants and products, since the depth of mesopores are just a few nanometers, unlike several hundred nanometers in conventional ordered mesoporous materials, like SBA-15. This type of mesopores are known as psuedo 3D mesopores [26, 31, 32].

3.2.5 Nitrogen Physisorption

To understand the textural properties of the $Ti_{1-x}V_xO_2$ materials, N_2 adsorption–desorption studies has been carried out. N_2 physisorption results and BJH pore size distribution are shown in Fig. 3. Pore size and surface area for the TVx materials is calculated and shown in Table 1. All materials show type IV adsorption–desorption isotherm with typical H_2 hysteresis loop characteristic of disordered mesoporous material. Bimodal pore size distribution was observed in the mesoporous regime from BJH plot for $Ti_{1-x}V_xO_2$ materials.

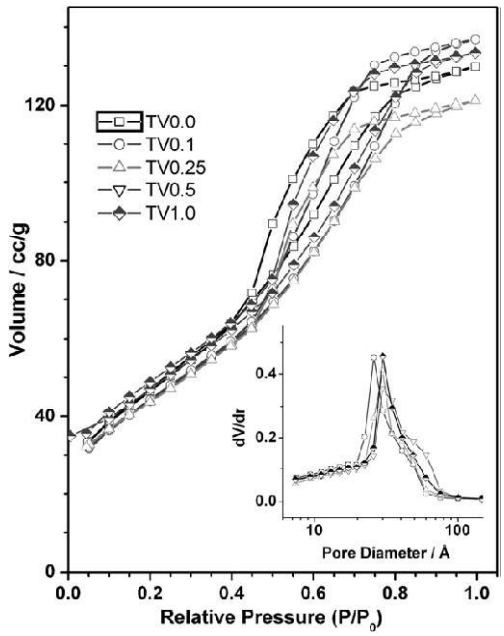

Figure 5. N_2 adsorption–desorption isotherms of $Ti_{1-x}V_xO_2$materials. BJH pore size distribution given in the inset.

3.3 Catalytic Activity Studies

TVx materials were used for oxidation of different sulfides. All TVx compositions were evaluated to understand the effect of vanadium concentration for sulfoxidation. To understand the temperature effect on the oxidation, the reaction was carried out at ambient and sub ambient (278 K) temperatures.

3.3.1 Effect of Composition

Catalytic conversion of different sulfides with TVx materials (x = 0.1, 0.5, 1.0) at room temperature are shown in Fig. 6. With lowest vanadium composition TV0.1 material after 6 h at ambient conditions ethylmethylsulfide (EMS), diethylsulfide (DES) and thioanisole gives 80%, 67% and 85% conversion with 99% selectivity for corresponding sulfoxides. Certain reactivity trend emerges out clearly from the results presented in Fig. 6. (a) Irrespective of V-content, DES shows 100% or close to 100% selectivity for diethyl-sulfoxide. (b) Generally higher V content (V = 1) leads to more sulfone with overall decrease in conversion of sulfoxides. (c) EMS with x = 1 shows more than 98% selectivity to sulfone.

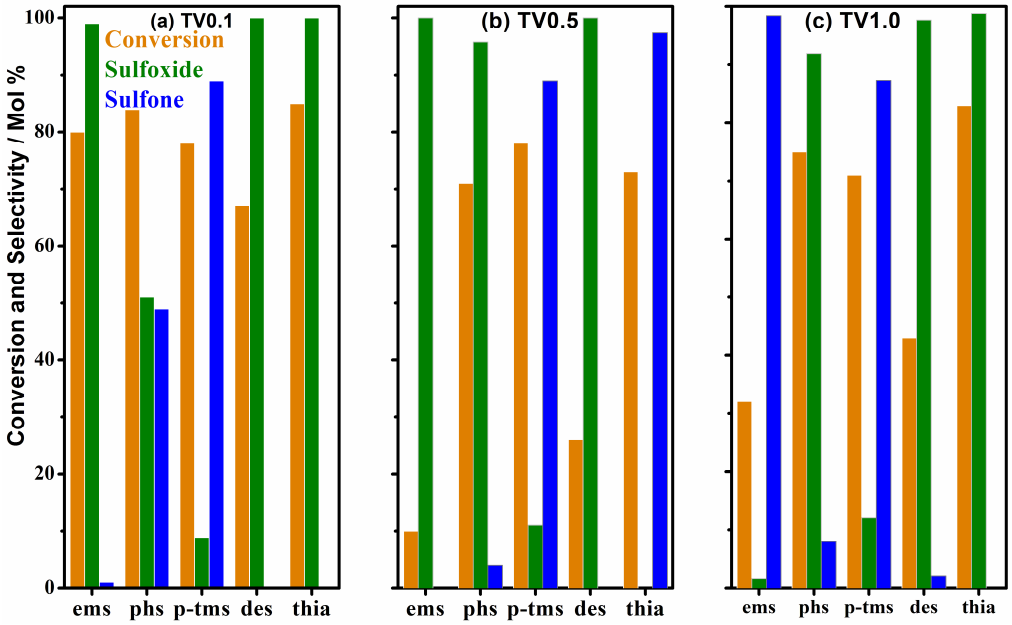

Figure 6. Catalytic activity dependence on vanadium content in $V_xTi_{1-x}O_2$ materials studied with ethylmethylsulfide, phenylsulfide, methyl-p-tolylsulfide, ethylsulfide and thioanisole for sulfoxidation reaction.

(d) Indeed it is strange to observe that sulfoxidation of thioanisole to corresponding sulfoxide with high yield for x = 0.1 and 1; however x = 0.5 leads to high yield of sulfone. We are yet to understand this abnormal change in reactivity pattern with x = 0.5. (e) Irrespective of V-content, methyl-p-tolylsulfide leads to similar conversion level around 75–80%; however high selectivity towards corresponding sulfone indicates the oxidation of sulfoxide to sulfone is likely to be fast. Sulfide oxidation was carried out on representative sulfides (EMS and DES) at RT and the results are shown in supporting information (Fig. SI). Indeed without V, pure TiO_2 shows very less activity and this demonstrates the importance of V for oxidation reactions. Especially the isolated V^{5+} incorporated in the TiO_2lattice, as demonstrated in the Raman spectra (Fig. 5), is likely to be the active species [33] for the sulfide oxidation reaction.

3.3.2 Effect of Temperature

Temperature plays an important role in affecting the conversion. To understand the effect of temperature we have studied reactions at 278, 298 and 328 K with TV0.1 material for 6 h. Fig. 7 shows conversion of sulfide and selectivity for corresponding sulfoxide/sulfone. Ethylmethylsulfide, phenylsulfide (PhS) and thioanisole gives 68%, 100% and 51% conversion with 100%, 99.9% and 92.15% selectivity for corresponding sulfoxides at 278 K. Indeed sulfide to sulfoxide at 278, 298 and 328 K on x = 0.1 indicates the following trend. (1) Generally a marginal decrease in conversion of all sulfides occurs with decreasing temperature. However, PhS shows a reverse trend that 278 K lead to the highest PhS conversion with 100% sulfoxide selectivity. (2) Increasing temperature also increases the extent of oxidation from sulfoxide to sulfone. This observation underscores the sequential oxidation of sulfide to sulfoxide to sulfone. Indeed sulfoxide formation is kinetically controlled and sulfone is thermodynamically controlled. PhS and p-TMS leads to more sulfones. Generally an increase in reaction temperature and V-content leads to more sulfones and hence it is suggested to a mild condition at RT (or 298 K) with x = 0.1 content of V for preferential sulfoxide formation. However more studies are required to explore with different substrates to generalize the above conclusion. Results reported in this communication is superior to the results found in the literature, in terms of either easy synthesis procedure of catalyst, smaller amount of oxidant or the reaction temperature. Ayala et al. [19] showed long synthesis procedure of catalyst with 24 h

reaction time in the presence of organic oxidants and low sulfoxide yield compared to our catalyst. Karimi et al. [20] reported phenylsulfide and other sulfides to sulfoxide in the presence of upto 8 equivalents of oxidant, whereas we used 1.5 eq. of oxidant. Varma and Naicker [8] achieved good sulfoxide yield, but at a reaction temperature 358 K, while our catalyst demonstrates similar activity at ambient and sub-ambient conditions.

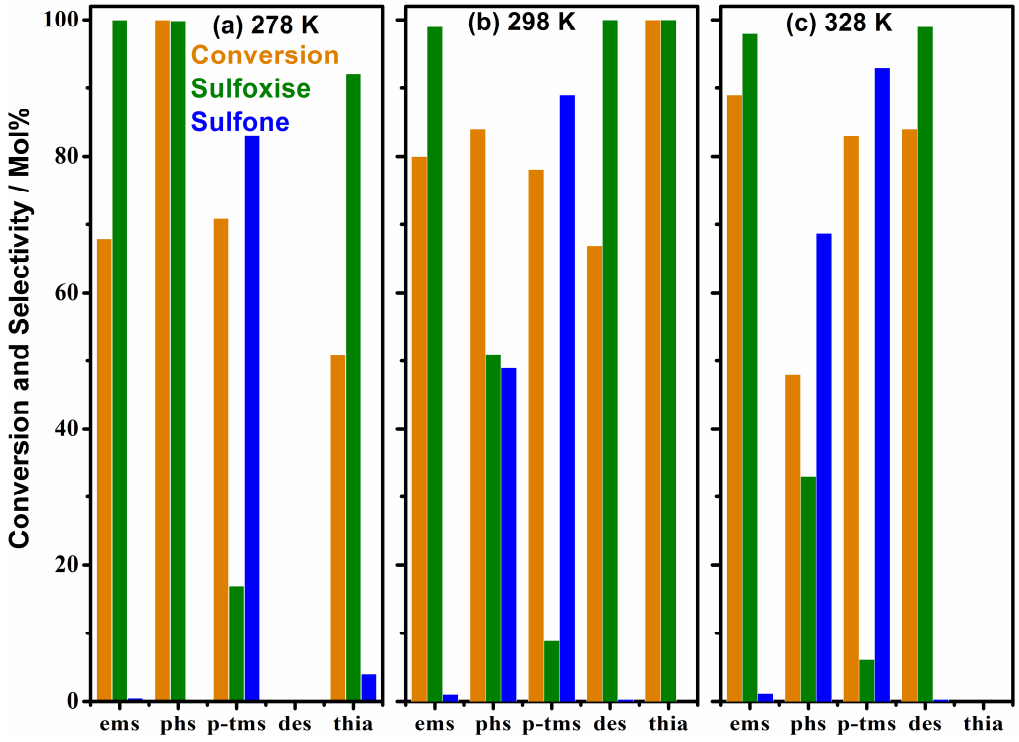

Figure 7. Catalytic activity dependence on temperature for ethylmethylsulfide, phenylsulfide, methyl-p-tolylsulfide, ethylsulfide and thioanisole with TVx (x = 0.1) material at (a) 278 K, (b) 298 K and (c) 328 K.

3.3.3 Recycle Studies

Recycle studies were carried out upto three cycles at ambient temperature with different substrates for 6 h each. After first cycle the reaction mixture is filtered and catalyst is separated dried and then used for 2nd cycle; similarly for 3rd cycle. The results are plotted in Fig. 8, and it shows no significant change in reaction pattern observed between first and third cycle studies. Product selectivity remains the same for all three cycles. Indeed recycle studies demonstrate a good stability of the catalyst.

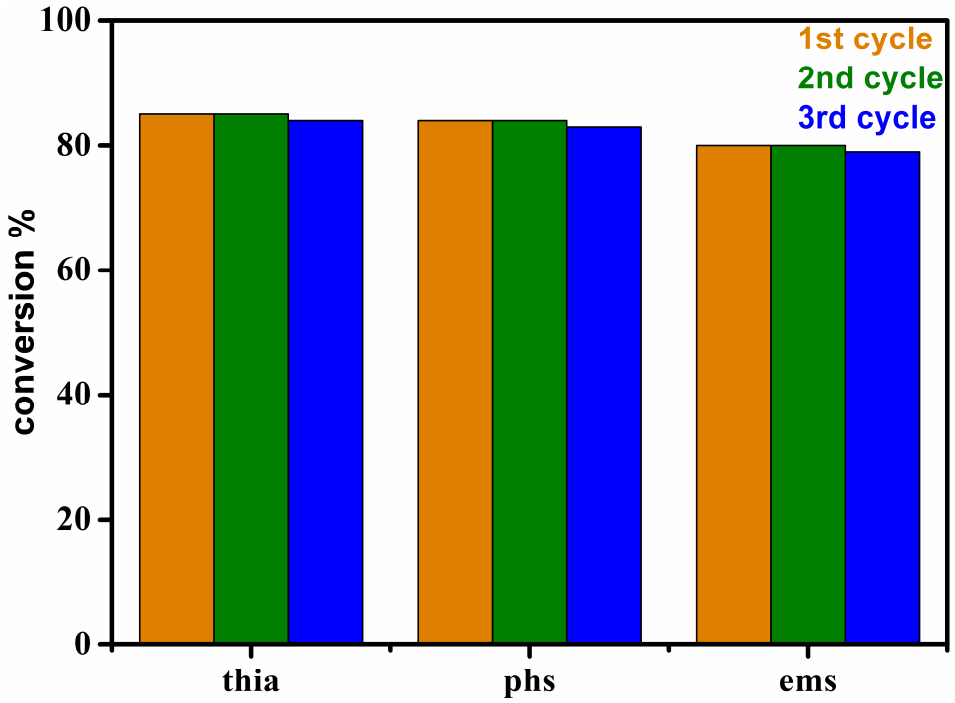

Figure 8. Recycle studies for TV0.1 upto three cycles with ethylmethylsulfide, thioanisole and phenylsulfide.

3.4 Conclusions

Vanadium incorporated in disordered mesoporous nanocrystallinetitania catalysts were prepared by simple solution combustion method. Incorporation of vanadium ions in the titania lattice framework was confirmed by XRD, Raman, EDX and HRTEM techniques. Sulfide oxidation was carried out with 30 wt.% aqueous hydrogen peroxide at ambient and sub-ambient temperatures (278 K) with high yield for various sulfoxides. Isolated V in TiO_2 is responsible for sulfoxidation activity.

3.5 References

1. R. C. Larock, *Comprehensive Organic Transformation*, Wiley-VCH, New York, (1989).
2. R. A. Sheldon, J. K. Kochi, *Metal-Catalyzed Oxidations of Organic Compounds, Academic Press*, New York, (1981).
3. G. Procter, S. V. Ley, *Comprehensive Organic Synthesis*, Pergamon Press, Oxford, UK, (1991).

4. W. P. Griffith, J. M. Joliffe, L. L. Simandi, *Dioxygen Activation and Homogeneous Catalytic Oxidation*, Elsevier, Amsterdam, (1991).
5. P. Maity, C. S. Gopinath, S. Bhaduri, G. K. Lahiri, *Green Chem.* (2009) **11** 554–561.
6. P. Brougham, M. S. Cooper, D. A. Cummerson, H. Heaney, N. Thompson, *Synthesis* (1987) **11** 1015–1016.
7. F. L. Fire Sr., *The Common Sense Approach to Hazardous Materials*, third ed., Pennwell Corporation, USA, (2009).
8. R. S. Varma, K. P. Naicker, *Org. Lett.* (1999)**1**189–191.
9. S. P. Das, J. J. Boruah, N. Sharma, N. S. Islam, *J. Mol. Catal. A: Chem.* (2012) **356** 36–45.
10. M. M. Khodaei, K. Bahrami, A. Karimi, *Synthesis* (2008) **11** 1682–1684.
11. C. W. Jones, *Applications of hydrogen Peroxide and Derivatives*, Royal Society of Chemistry, Cambridge, UK, (1999).
12. G. Strukul, *Catalytic Oxidations with Hydrogen Peroxide as Oxidant*, Kluwer Academic, Dordrecht, The Netherlands, (1992).
13. E. N. Prilezhaeva, *Russ. Chem. Rev.* (2000) **69** 367–408.
14. E. N. Prilezhaeva, *Russ. Chem. Rev.* (2001) **70** 897–920.
15. D. H. Rich, J. P. Tam, *J. Org. Chem.* (1977) **42** 3815–3820.
16. S. Burrage, T. Raynham, G. Williams, J. W. Essex, C. Allen, M. Cardno, V. Swali, M. Bradley, *Chem. Eur. J.* (2000) **6** 1455–1466.
17. A. Padwa, M. D. Danca, *Org. Lett.* (2002) **4** 715–717.
18. K. S. Ravikumar, J. P. Begue, D. B. Delpon, *Tetrahedron Lett.* (1998) **39** 3141–3144.
19. V. Ayala, A. Corma, M. Iglesias, F. Sanchez, *J. Mol. Catal. A* (2004) **221** 201–208.
20. B. Karimi, M. G. Nezhad, J. H. Clark, *Org. Lett.* (2005) **7** 625–628.
21. K. Sato, M. Hyodo, M. Aoki, X. Q. Zheng, R. Noyori, *Tetrahedron* (2001) **57** 2469–2476.
22. M. Lancaster, *Green Chemistry: An Introductory Text*, Royal Society of Chemistry, Cambridge, (2002).
23. F. Schüth, K. S. W. Sing, J. Weitkamp, *Handbook of Porous Solids*, Wiley-VCH, Weinheim, (2002).

24. D. Zhao, J. Feng, Q. Huo, N. Melosh, G. H. Fredrickson, B. F. Chmelka, G. D. Stucky, *Science* (1998) **279** 548–552.
25. D. G. Kulkarni, A. V. Murugan, A. K. Viswanath, C. S. Gopinath, *J. Nanosci. Nanotechnol.* (2009) **9** 371–377.
26. K. Sivaranjani, A. Verma, C. S. Gopinath, *Green Chem.* (2012) **14** 461–471.
27. X. Ye, Y. Yue, C. Miao, Z. Xie, W. Hua, Z. Gao, *Green Chem.* (2005) **7** 524–528.
28. K. Sivaranjani, C. S. Gopinath, *J. Mater. Chem.* (2011) **21** 2639–2647.
29. S. S. Kim, T. R. Pauly, T. Pinnavaia, *Chem. Commun.* (2000) 835–836.
30. J. C. Yu, L. Zhang, Z. Zheng, J. Zhao, *Chem. Mater.* (2003) **15** 2280–2286.
31. T. Mathew, K. Sivaranjani, E. S. Gnanakumar, Y. Yamada, T. Kobayashi, C. S. Gopinath, *J. Mater. Chem.* (2012) **22** 13484–13493.
32. K. Sivaranjani, S. Agarkar, S. B. Ogale, C. S. Gopinath, *J. Phys. Chem. C* (2012)**116** 2581–2587.
33. N. R. Shiju, M. Anilkumar, S. P. Mirajkar, C. S. Gopinath, B. S. Rao, C. V. Satyanarayana, *J. Catal.* (2005) **230** 484–492.

Chapter IV: A Green Chemistry Approach to Styrene from Ethylbenzene and Air on $Mn_xTi_{1-x}O_2$ Catalyst

4 $Mn_xTi_{1-x}O_2$

4.1 Introduction

Styrene (ST) is one of the important products in the petrochemicaland polymer industries and is a precursor to severalresins, plastics, rubbers and other copolymers [1]. Since 1940's, theindustrial production of ST has been done using ironoxide promoted by potassium catalysts, by the dehydrogenation of ethylbenzene (EB) with steam, at 700 °C [2, 3]. This dehydrogenation mechanism [4, 5] is endothermic (ΔH = 124.9 kJ mol^{-1}) in nature and hence it requires high reaction temperature. Although hydrogen is available as a side product, steam-based processes utilize a large amount of latent heat and they have thermodynamic limitations [6]. In addition, coke formation on the catalyst leads to severe catalyst deactivation, and EB conversion of less than 16% was achieved per pass [7].

Different materials have been used for ST synthesis, such as, metal oxides, carbon. Makkee et al. used Al_2O_3 calcined between 500 and 1200 °C, and achieved 42% EB conversion and 87% ST selectivity at 475 °C for 62 h [8]. Qui et al. employed ozonated multiwalled carbon nanotube (MWCNT) in range of 350–450 °C at atmospheric pressure, O_2/EB molar ratio varied from 1:1 to 3:1 with best EB conversion and ST selectivity values of 80% and 92%; however, above high activity occurs at a very low low rate of 2.3 mL vol% in 55 mL min^{-1} of EB + O_2 + N_2 [9]. Sekine et al. used pervoskite and reactions were conducted at 510 or 540 °C at atmospheric pressure in the presence of steam; molar ratio of steam to EB was 2 or 12 with 22% ST yield for 30 min [10]. Venugopal et al. has shown ceria containing hydrotalcite at 450 °C at atmospheric pressure a marginally decreasing styrene yield from 47 to 45% over a period of 72 h [11]. Shin et al. fed a balancing gas of water and EB in helium, over V_2O_5/CeO_2–MgO and achieved EB conversion of 43% and ST selectivity of 91% at 600 °C; prior to the activity measurement, the catalyst was activated in the steam low of 50 mL min^{-1} by heating up to 650 °C at the rate of 2.5 °C min^{-1} [12]. Sivaranjani et al. employed V-doped titania with molecular oxygen at 500 °C and obtained about 50% ST yield initially; however it continuously decreases at higher time on stream [13]. Various oxidants such as O_2, [13, 14] air, [15] N_2O [16] and CO_2 [17] have been used, and indeed, air as oxidant is cost effective and preferred green way of oxidation. Above literature reports demonstrates the wide open area of

styrene synthesis with better and sustainable yield. Design of catalysts which are stable, gives high selectivity (>90%) with conversion >50% for EB to ST conversion at lower temperatures around 500 °C or lower is one of the challenge in the field of heterogeneous catalysis [8–18]. Constant efforts have been made to develop catalysts, operating via oxidative dehydrogenation (ODH) mechanism route which is also exothermic in nature [19] to lower operating temperature for EB to ST conversion [20, 21].

Manganese is known for its superior catalytic properties for various redox processes in heterogeneous catalysis. MnOx supported on silica have been also used for EB to ST conversion [22]. Titania is known as excellent reducible catalytic support, but limited with low surface area. Nonetheless, disordered mesoporous materials [23] with pseudo-three-dimensional (p3D) nature have smaller diffusion lengths [24, 25] thus reactants and products can easily diffuse to and from the active sites of disordered mesoporous materials, which increases the selectivity and yield of the preferred product by decreasing the secondary reactions and hence the overall rate of the reaction. For the present manuscript, we have synthesized large surface area Mn-doped titania ($Mn_xTi_{1-x}O_2$) catalysts via solution combustion method [26–29]. We used $Mn_xTi_{1-x}O_2$ materials for EB to ST conversion in a fixed-bed reactor. These catalysts were evaluated between 430 and 570 °C for ST synthesis from ET using air or oxygen as an oxidant. Present disordered mesoporous $Mn_xTi_{1-x}O_2$ materials exhibits about 57% ST yield with high selectivity (>95%) under optimized conditions for long durations without undergoing deactivation under reaction condition. The current report is a part of ongoing investigations from our group towards broad understanding of metaloxide catalysts for oxidation and ODH heterogeneous catalytic reactions [30–38].

4.2 Results and Discussion

4.2.1 X-ray Diffraction

To understand structural features of the materials wide and low angle powder X-ray diffraction (XRD) were recorded for $Mn_xTi_{1-x}O_2$ materials. XRD results shown in Fig. 1 exhibits diffraction features of 101, 004, 200 and 204 facets of anatase phase of titania present in $Mn_xTi_{1-x}O_2$ materials. Diffraction pattern is indexed to JCPDS file no.: 21-1272, 21-1276 for anatase phase of titania with small amount of rutile phase.

About 2–9 % of rutile phase, (6.2 for TiO_2, 3.8 for MT2, 8.7 for MT5, 5.8 for MT7, 7.9 for MT10, 6.8 for MT12 and 2.1 for MT15) was also observed (# mark in Fig. 1) along with predominant anatase phase in the fresh catalysts. No manganeseoxide diffraction peaks were observed up to 15% of Mn content; indicating high dispersion of manganese ions into TiO_2 lattice. Broad peaks indicate the nanocrystalline nature of the catalysts. Crystallite size was calculated using Debye–Scherrer equation for all materials and shown in Table 1. Low angle XRD recorded for all xMT materials show a single broad peak between 2θ = 0.8 and 1.3° (Fig. 1 – inset) indicating a disordered mesoporous nature of materials.

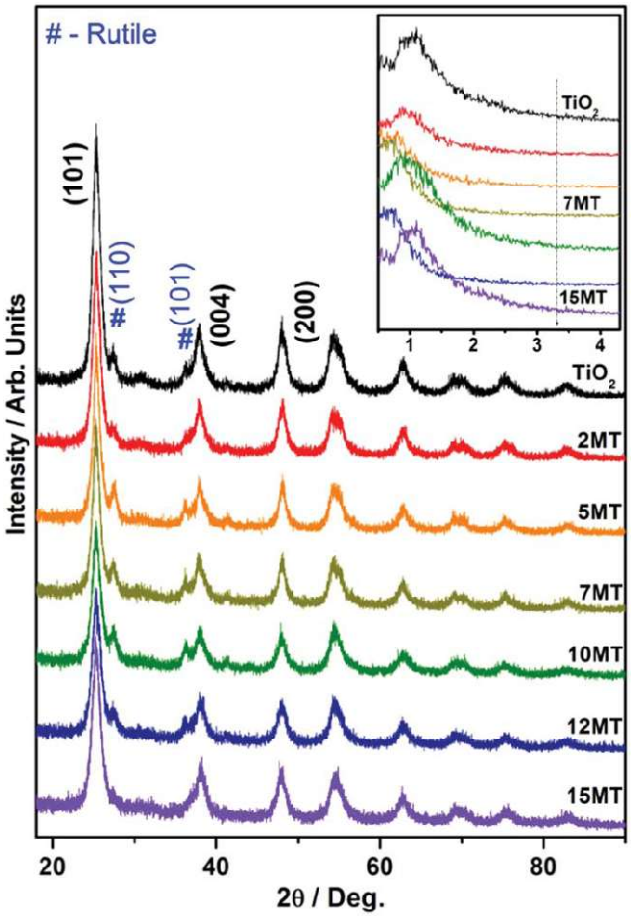

Figure 1. Wide angle XRD patterns recorded from $Mn_xTi_{1-x}O_2$ catalysts with different Mn content up to 15 atom %. XRD of TiO_2 prepared by SCM is also shown for comparison. Low angle XRD pattern is given in the inset indicates the disordered mesoporosity.

4.2.2 Transmission Electron Microscopy

Transmission electron microscopic images recorded are given for representative xMT materials in Fig. 2. TEM images exhibit particles with spherical morphology of 7–8 nm size, with high porosity associated with $Mn_xTi_{1-x}O_2$ materials. It is to be underscored that present set of disordered mesoporous materials were prepared without any surfactant or template molecules, compared to ordered mesoporous materials [41–43] that employ molecules like P123 copolymer, CTAB etc. as surfactant. HRTEM images exhibits d spacing for various planes of TiO_2. Selected area electron diffraction (SAED) patterns were recorded and shows predominantly 101 plane of anatase phases of titania. Similar porous structure was observed for TiO_2, 7MT and 12MT.

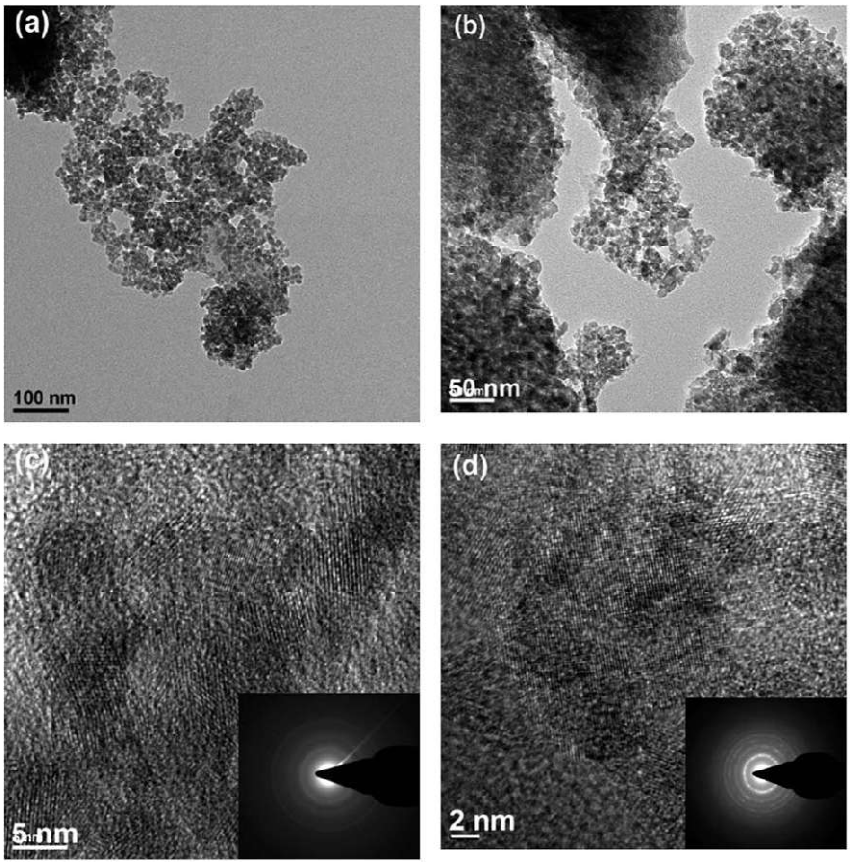

Figure 2. TEM image of (a) 2MT, (b) 5MT, (c) 10MT and (d) 15MT materials are shown; SAED pattern is shown in inset. Spherical morphology of TiO_2 with (101) facets were found to be predominantly present, for all $Mn_xTi_{1-x}O_2$ materials.

4.2.3 Raman Spectroscopy

Raman spectral analysis of xMT materials are shown in Fig. 5. Typical vibrational features of anatase was observed at 145 (Eg), 198 (Eg), 398 (B1g), 516 (A1g +B1g) and 640 (Eg) cm^{-1}. There is shift in position of peak from 145 to 159 cm^{-1} with an increase in Mn-content in xMT materials. Intensity of all typical features decreased drastically due to Mn incorporation into the titania lattice. The above decrease in the intensity of Raman features is due to the symmetry breaking of Ti–O–Ti by Ti–O–Mn structural features due to incorporation of Mn-ions in TiO_2. XRD and TEM analysis reveals no change incrystallinity and morphology of $Mn_xTi_{1-x}O_2$ materials compared to that of pure TiO_2. Albeit its small percent of rutile phase (Fig. 1), the same was observed with few compositions prominently (5MT) in Fig. 3.

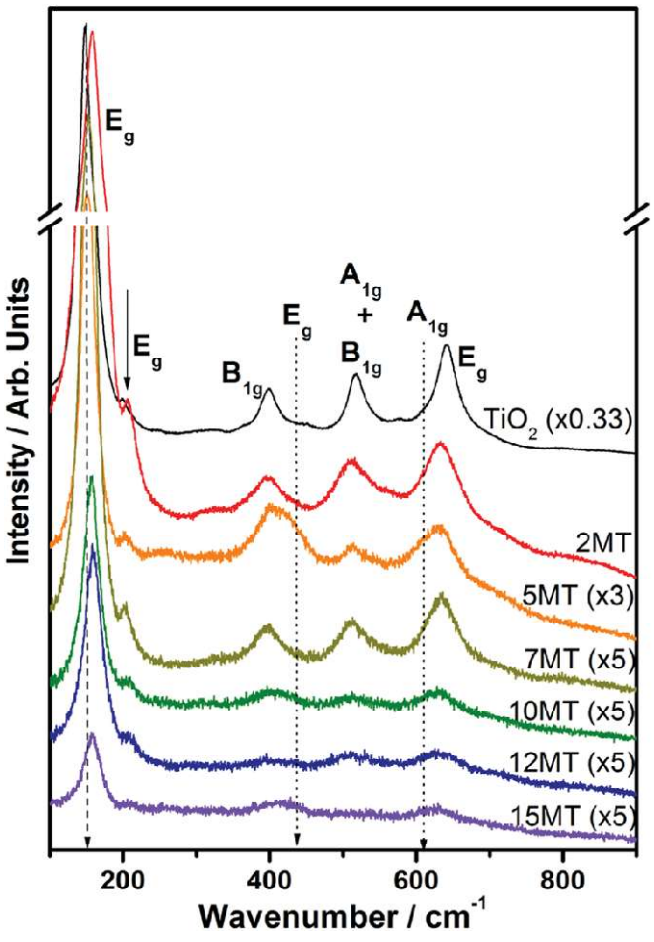

Figure 3. Raman spectra for xMT materials, multiplied with suitable factors for clarity. No manganese oxide feature was observed up to15% Mn loading, and

broadening of peaks on Mn-doping indicating the symmetry breaking of regular Raman features of anatase phase. Note the blue shift in Eg from 145 on TiO_2 (dashed line) to 159 cm^{-1} alongwith line broadening upon Mn introduction into the titania lattice. Rutile phase features are indicated by two dotted arrows.

4.2.4 X- Ray Photoelectron Spectroscopy

Electronic structure of xMT materials was explored via X-ray photoelectron spectroscopy of all xMT materials. Fig. 4 shows XPS spectra of Ti2p, and Mn2p (inset) core level spectra of xMT materials. Ti2p3/2 core level appears at a binding energy (BE) around 459 eV for all xMT materials. This is in good agreement with the BE reported for Ti^{4+} in literature reports [44]. BE of Mn2p3/2 and O1s (not shown) core levels appear around 641.3 ± 0.1 and 529 ± 0.2 eV, respectively, for all $Mn_xTi_{1-x}O_2$ materials. Observed BE of Mn2p3/2 core level around 641.3 eV for all xMT materials indicate the oxidation state of Mn to be 3+ [45, 46].

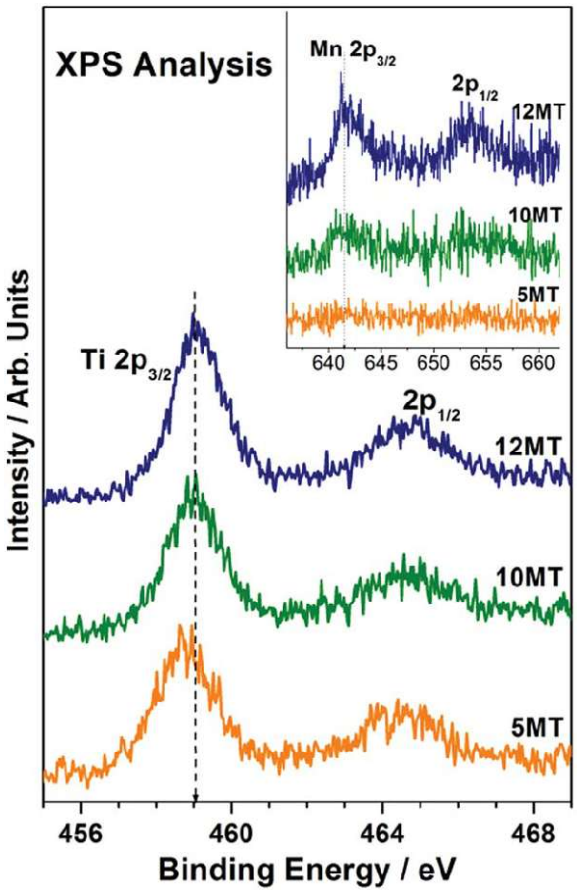

Figure 4. XPS of Ti2p and Mn2p (inset) core levels of xMT materials.

BE of Mn^{4+} state was reported to appear at 642.5 eV, which is significantly higher than the BE in XPS spectra, confirming that Mn is not present in 4 + oxidation state in xMT materials. A comparison of ionic sizes of Ti^{4+} (0.68 Å), Mn^{3+} (0.645 Å) and Mn^{4+} (0.53 Å) also suggest the possibility of Mn^{3+}, rather than Mn^{4+} oxidation state. Indeed, Mn^{3+} oxidation stateis likely to enhance the lattice oxygen storage/release properties under ODH reaction conditions.

4.2.5 Scanning Electron Microscopy

Elemental mapping of $Mn_xTi_{1-x}O_2$ materials were studied to understand the distribution of different elements in the materials. Representative images recorded for different elements from SEM are given in Fig. 5. Manganese and titanium are present and their distribution is shown in yellow and blue colors in separate images, along with the particle image. Homogeneous distribution of Mn in $Mn_xTi_{1-x}O_2$ lattice was observed for all compositions. Mn percentage for all $Mn_xTi_{1-x}O_2$ materials were measured and shown in Table 1.

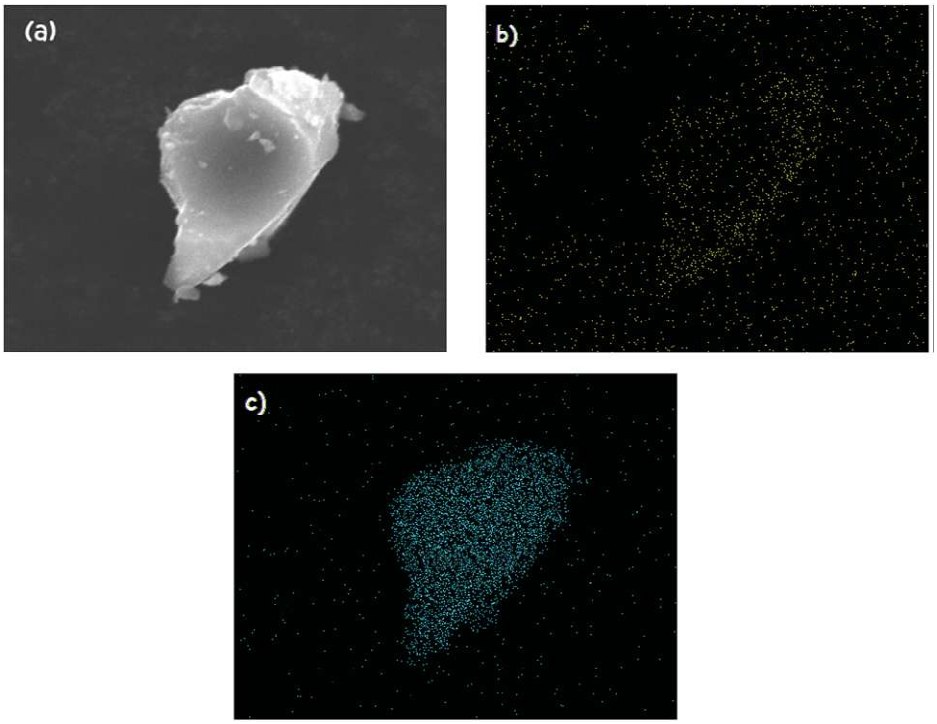

Figure 5. (a) SEM image of a 5MT catalyst particle, corresponding elemental mapping of (b) Mn in yellow colour, and (c) Ti in blue colour through EDAX analysis. Results indicate a uniform distribution of Mn in titania.

4.2.6 Nitrogen Physisorption

Textural features of xMT materials were studied via nitrogen adsorption–desorption isotherms and the results are shown in Fig. 6a; Barrett–Joyner–Hallenda (BJH) pore size distribution plots are shown in Fig. 6b. Mesoporous nature of material can be inferred as all materials exhibit type IV adsorption–desorption isotherm with H2 hysteresis loop, which is characteristic of mesoporous materials. Surface area of material was calculated from Brunauer–Emmett–Teller (BET) equation, and shown in Table 1. BJH pore size distribution for xMT materials exhibits bimodal (2MT and 7MT) or unimodal (all compositions except 2MT and 7MT) pore size distribution. xMT materials exhibits average pore diameter of around 3.5 ± 0.5 nm. Calculated pore volume for $Mn_xTi_{1-x}O_2$ materials are also shown in Table 1.

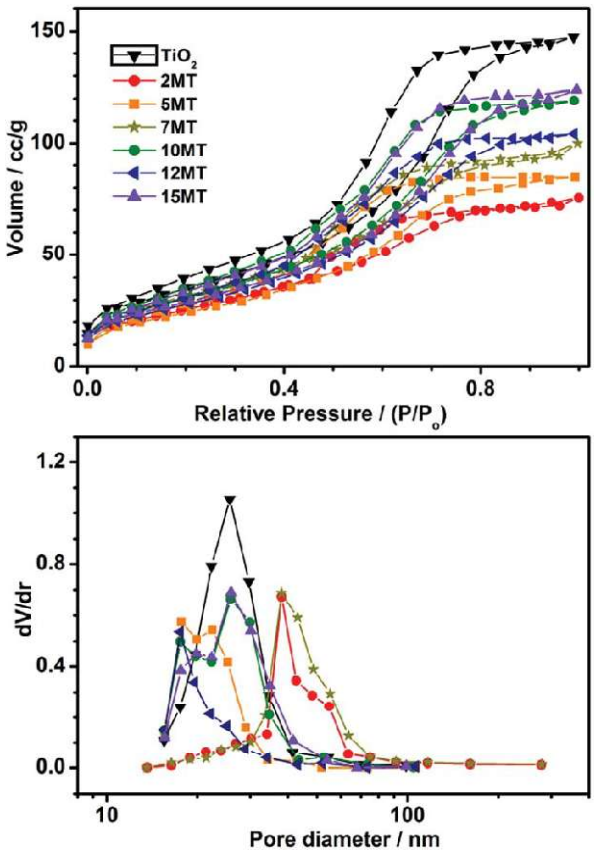

Figure 6. (a) N_2 adsorption–desorption isotherms, and (b) BJH pore-size distribution of xMT catalysts.

Table 1. Physicochemical properties of $Mn_xTi_{1-x}O_2$ catalysts

Catalyst	bulk Mn Content	BET surface Area(m^2/g)	Pore size(nm)	pore volume(cc/g)	crystalline size (mm)
TiO_2	0	125	3.80	0.2281	8.8
2.0MT	1.38	79	3.89	0.1121	7.4
5.0MT	4.10	87	2.25	0.1311	8.5
7.0MT	6.61	101	3.89	0.1513	8.9
10MT	7.43	110	2.57	0.1811	7.9
12MT	11.04	102	1.87	0.0874	6.8
15MT	14.30	104	2.59	0.1917	7.4

4.3 Catalytic Activity Studies

EB to styrene ODH reaction with air or molecular oxygen has been investigated as a probe reaction to investigate the catalyticactivity of xMT materials. This is primarily to investigate the influence of Mn^{3+} introduced in TiO_2 lattice framework. However, caution must be exercised due to the exothermic nature of the reaction with combustible reactant and products in the presence of air or oxygen. Reactions were carried out at comparatively low temperature, relative to conventional endothermic reaction, [4, 5] and at atmospheric pressure. Various factors such as flow rates of EB, air/oxygen, catalyst composition and temperature were varied to understand their effects on EB conversion and selectivity to styrene.

4.3.1 Effect of Composition

For selective EB conversion to ST, and to minimize the chances of over oxidation of easily combustible EB and ST, active catalytic centers have to be optimized. To find optimum Mn-content for the highest selective oxidation, reactions were carried out with different Mn-content, from TiO_2 to 15 mol% Mn into TiO_2 lattice. Reaction studies were carried out with xMT materials for 12 h on time on stream (TOS) and at EB flow rate of 1.8 mL h^{-1}, and 40 mL min^{-1} O_2 flow at 500 °C. Conversion, selectivity and yield values were measured for different xMT and are plotted in Fig. 7. Except TiO_2, all xMT catalysts show an increase in ST yield with increase in TOS. TOS data with bare TiO_2 is plotted for reference to underscore the effect of Mn content. TiO_2 exhibited about 20% ST yield, and 72–82% ST selectivity. With

increase in Mn-content, EB conversion and ST yield also increased. 15MT shows the best ST yield (55%) and 90–95 % styrene selectivity for 12 h, and this catalyst composition shows a sustainable activity for 45 h, which will be discussed later. Although an increase in catalytic activity was observed from TiO_2 to 2MT, with further increasing Mn-content the activity does not increase linearly. 2–10% Mn doped titania shows comparable yield. This suggests the availability of Mn on the surface is limited due to bulk doping in titania lattice. However, a comparison of Mn-content to catalytic activity, indicates the decline in specific activity from 2 to 10% Mn, and then it marginally increases at 12 and 15% Mn. We also caution the readers, to take a note on changes in the catalyst nature in the first few hours from anatase phase xMT to Mn_3O_4 supported on rutile titania (vide infra). Apart from ST, benzene is a main side product (<5%); toluene and styrene oxide are also formed as minor products with selectivity below 2%.

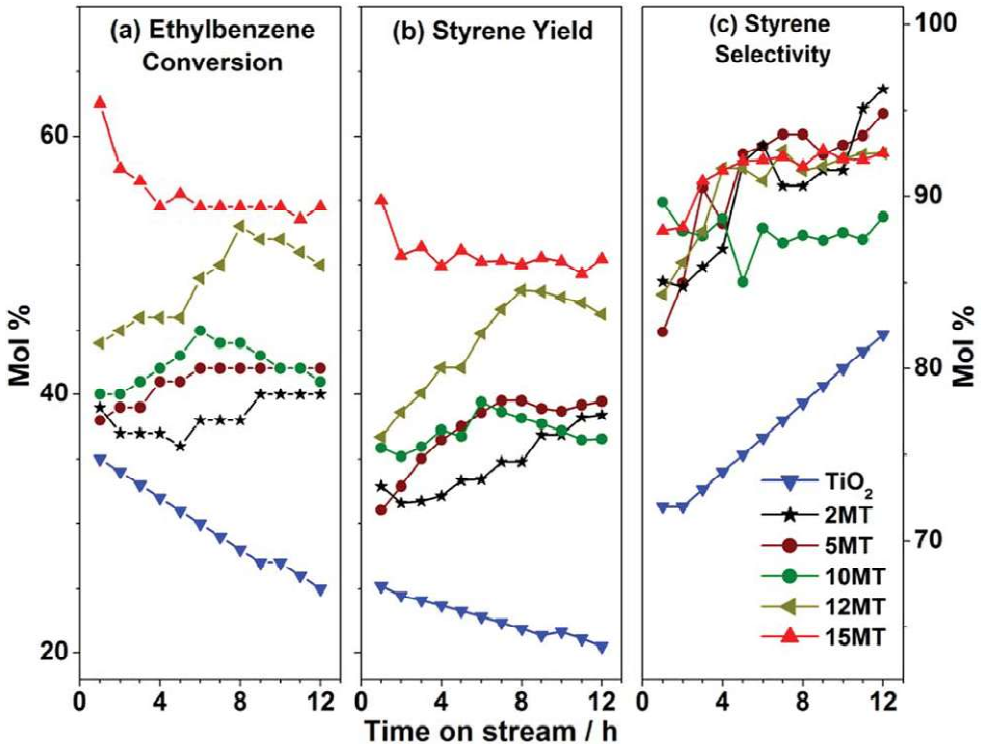

Figure 7. (a) EB conversion, (b) ST yield and (c) selectivity at 500 °C are plotted for xMT compositions. Oxygen and EB flow rate was 40 mL min^{-1} and 1.8 mL h^{-1} respectively. 15MT exhibits the highest conversion of EB and yield of ST.

From the above results, it can be inferred that Mn-doped titania centers are the actual catalytic centers for conversion. Selectivity for ST increases with TOS. 12MT, 10MT and 5MT showed gradual increase, 2MT and 7MT showed steady conversion. 15MT exhibits two fold higher yield value than TiO_2. 15MT catalyst exhibits better yield than intermediate xMT catalysts. 15MT is the best composition among all the compositions that are evaluated. Any further increase in doping of Mn-content resulted in a mixed phase of Mn_3O_4 and $Mn_xTi_{1-x}O_2$ indicating the solid solubility limit of Mn in titania.

4.3.2 Effect of Oxygen Flow

O_2 supply was optimized to get the highest ST yield and selectivity. EB flow was fixed at 1.8 mL h^{-1} over fixed bed of 15MT catalysts at 500 °C, and O_2 flow was varied at 20, 40 and 60 mL min^{-1} and the reaction was studied. Measured values of conversion, yield and selectivity are plotted for these studies, and the results are shown in Fig. 8. Conversion increased with increase in oxygen flow rates. Styrene yield increased with time due to a gradual increase in EB conversion at 20 mL min^{-1} O_2 flow. O_2 flow at 20 and 40 mL min^{-1} after 6 h show constant conversion values at 35 and 50 mol%, respectively, indicating the steady state attained in 5–6 h. However, 60 mL min^{-1} O_2 flow shows a constant yield at 45 mol%; nevertheless, 60 mL min^{-1} O_2 flow shows a steadily declining (increasing) selectivity (conversion). At the end of 12 h, 60 mL min^{-1} O_2 flow exhibits 48% EB yield, and 72% styrene selectivity; in contrast, at 15 h on TOS, conversion decreased to 21% indicating the onset of deactivation (result not shown). EB conversion increases from 25 to 35 mol% with 20 mL min^{-1} O_2 flow in the initial hours indicating a possibility of restructuring of catalyst in the transient state. 40 mL min^{-1} O_2 flow was observed to an optimum rate for high ST yield. Benzene formed as side product along with toluene and styrene oxide with less than 1% selectivity. It is also to be mentioned that the gas product analysis demonstrating the formation of significant amount of CO_2 suggesting the combustion of reactant and/or product, especially at high oxygen flow (Fig. 8).

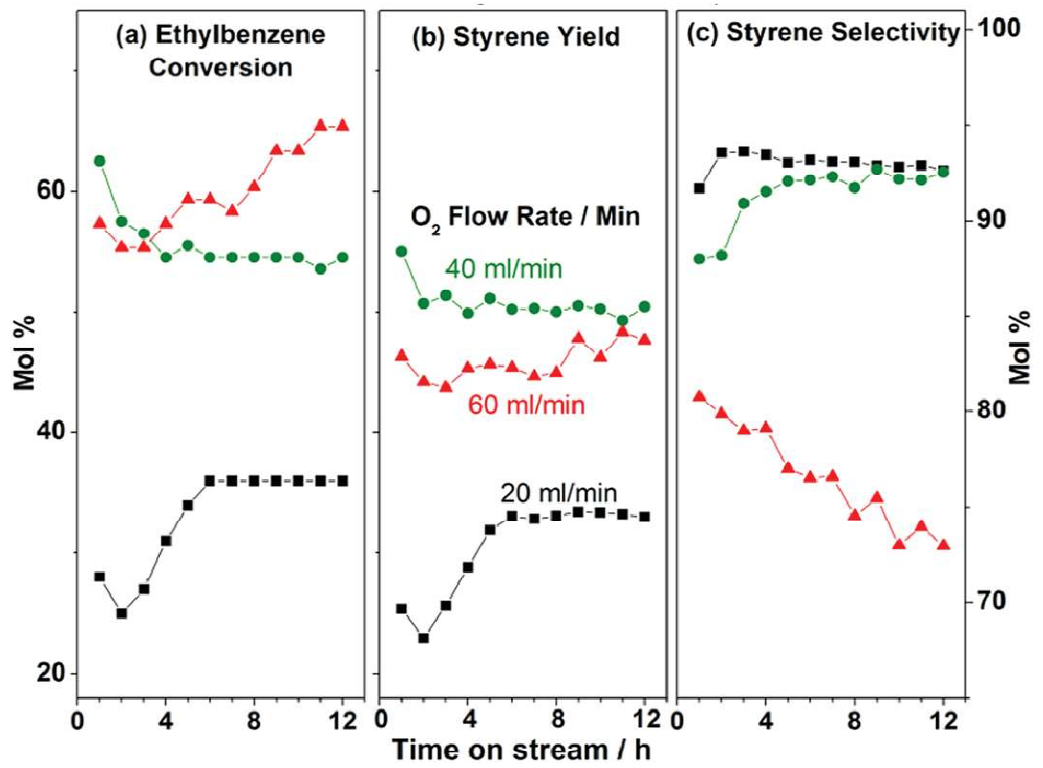

Figure 8. Effect of oxygen flow on catalytic activity is shown for 20, 40 and 60 mL min^{-1} flow. EB flow rate was maintained at 1.8 mL h^{-1} over fixed bed of 15MT catalysts at 500 °C.

4.3.3 Effect of Air Flow

O_2 was replaced by air to minimize the explosion hazard. Air contains diluted oxygen (21%), and hence a higher flow rate is required to simulate the equivalent amount of oxygen used in the results shown in Fig. 7 and 8. Due to diluted O_2 better activity and ST selectivity was expected. Studies at different air flow rates were carried out to understand the effect of air flow. Air flow at 60, 120, 180 and 240 mL min^{-1} were carried out at fixed EB flow rate of 1.8 mL h^{-1} over 15MT at 530 °C, and the results are shown in Fig. 9. With 60 mL min^{-1} flow there is a steady ST yield at 19%; however, the yield increased steadily at 120 and 180 mL min^{-1} flows. However, yield decreases at 240 mL min^{-1}, due to facile combustion of EB and ST too, towards CO_2 and water. With increase in flow rates the ST yield increases and the optimum yield was obtained at an air flow rate of 180 mL min^{-1}. 180 mL min^{-1} air flow exhibit 57% ST yield >9 h with 95% selectivity. A gradual increase in conversion and yield was observed in the first eight hours of reaction at 120 and 180 mL min^{-1} flow indicating a

possible change in the nature of catalyst. Air flow exhibits higher selectivity for ST compared to O_2 low, always above 95%. Mainly benzene is formed (<3%) as side product.

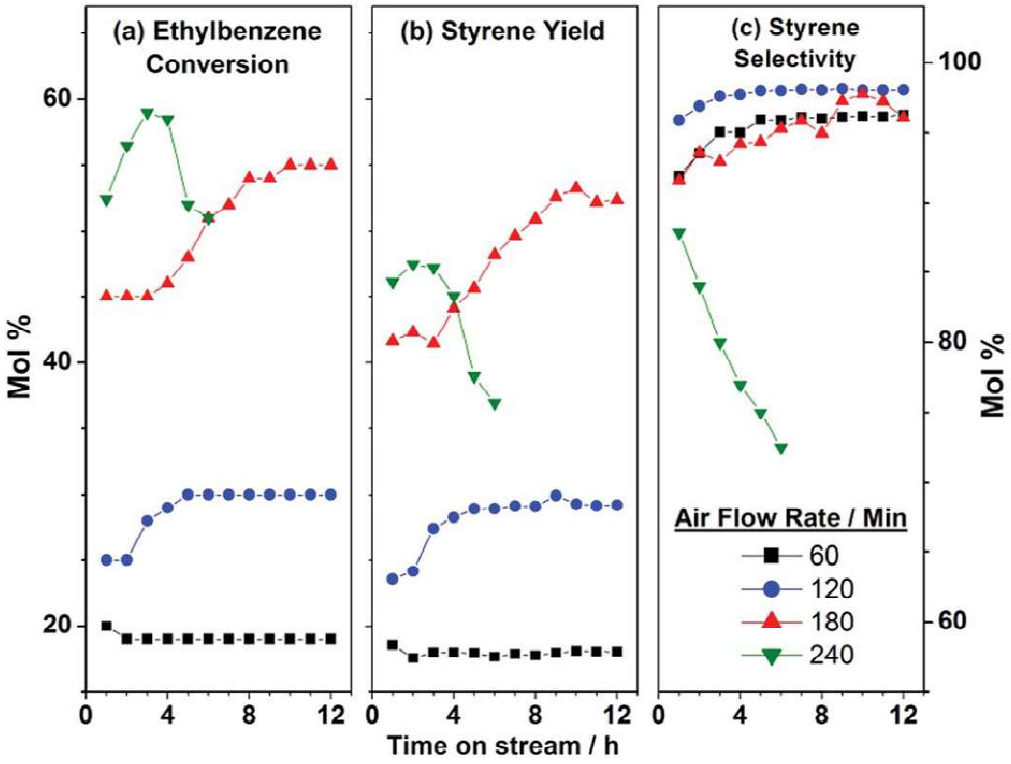

Figure 9. Air flow rate at 60, 120, 180 and 240 mL min^{-1} were evaluated. EB at 1.8 mL h^{-1}, and air at 180 mL min^{-1} flow rate on 15MT catalyst at 530 °C gives highest ST yield.

4.3.4 Effect of Reaction Temperature

Temperature plays a significant factor for EB to ST conversion. Although EB conversion increases with increase in reaction temperature, above an optimum temperature, combustion is favored due to favorable oxidizing conditions; this tends to decrease the ST yield. To optimize temperature for ST yield, reactions were carried out between 440 and 570 °C at 180 mL min^{-1} air flow rate. Measured EB conversion, styrene yield and selectivity values for above reactions are plotted in Fig. 10. Generally conversion increases with increasing reaction temperature. 530 °C shows optimum temperature for EB to ST conversion. The highest ST yield was observed at 530 °C with ST selectivity at 97%. Conversion values increased marginally even up

to 12 h for 500 and 530 °C, but steady state was reached at TOS = 5 h at 440 and 470 °C. 570 °C demonstrates a fast increase in conversion up to 8 h, followed by a decline; selectivity was also observed below 90% indicating the increasing contribution from combustion. For all temperatures about 3–5% of side products, such as benzene and toluene are also produced; CO_2 mol% increases from 5 to 10% confirms increasing combustion at higher temperatures (Fig. 10).

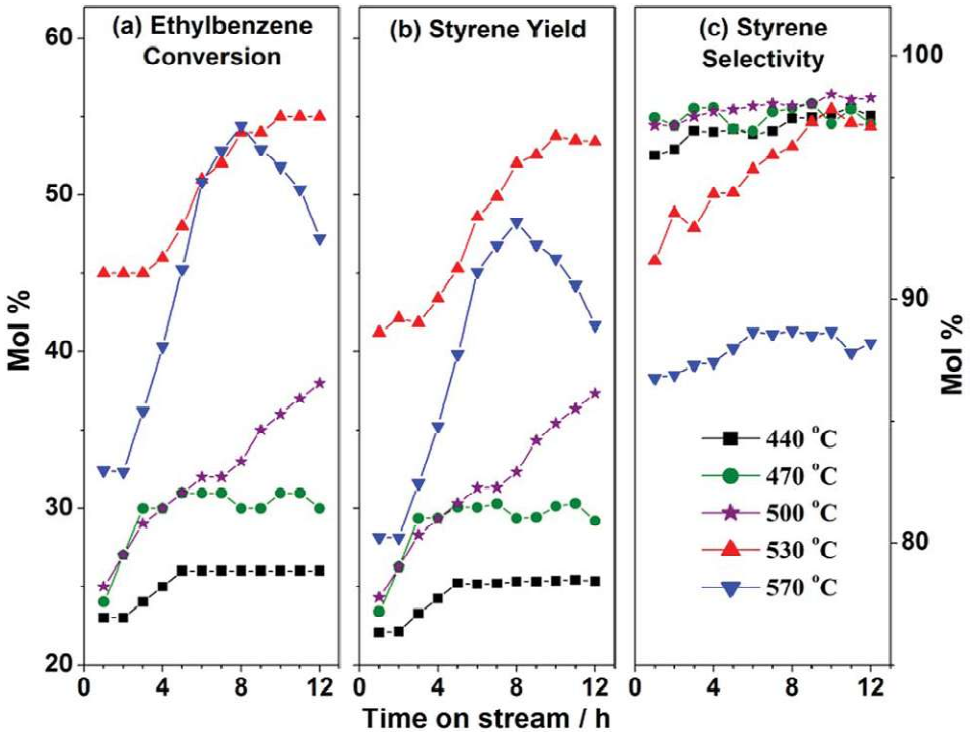

Figure 10. Effect of reaction temperature; on activity trend at 1.8 mL h^{-1} EB flow, and 180 mL min^{-1} air flow over 15MT catalysts, between 440 and 570 °C. 530 °C shows the optimum results.

4.3.5 Effect of EB Flow Rate

Rate of reactant flow over catalyst bed determines the residence time of substrate thus controls catalysts reactivity, and hence overall product distribution. Effect of EB flow rates over 15MT catalysts bed were studied at air flow rate of 180 mL min^{-1} at 530 °C. To optimize EB flow, different flow rates of 1.2, 1.8, 3.0 and 4.2 mL h^{-1} were studied, and the results are shown in Fig. 11. 1.2 mL h^{-1} EB flow shows EB conversion at 38%; however it deteriorates very fast and no conversion was observed at higher TOS, likely due to coke deposition and hence deactivation of the catalyst. TG-DTA

analysis further confirms the amount of coke was about 10% (result not shown). 1.8 mL h^{-1} flow exhibits the highest yield of ST; EB conversion increases gradually between 3 and 9 h, and reaches steady state at 9 h and thereafter the reactivity was maintained. Higher flow rates at 3 and 4.2 mL h^{-1} shows lower, but steady EB conversion, 97–99 % ST selectivity and ST yield for 12 h TOS. ST selectivity observed to be increasing from 90 to 97% at 1.8 mL h^{-1} EB flow, whereas the same decreases from 90 % at 1.2 mL h^{-1} EB flow. 1.8 mL h^{-1} flow rate provides optimum EB flow rate for high ST yield.

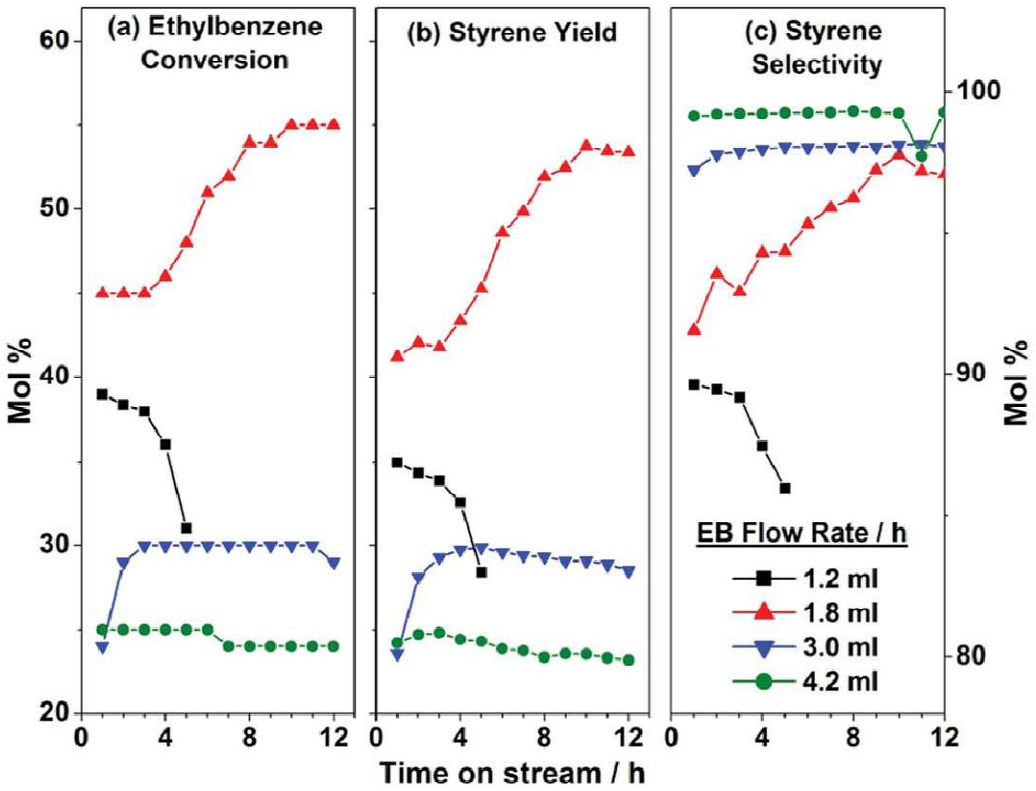

Figure 11. EB flow rate studied at 1.2, 1.8, 3.0 and 4.2 mL h^{-1}; with optimized air flow at 180 mL min^{-1} at 530 °C over 15MT catalysts. 1.8 mL h^{-1} EB flow shows the highest EB conversion and ST yield.

4.3.6 Catalyst Stability

Optimization studies of reaction parameters for high ST yield were demonstrated earlier and optimum values are 1.8 mL h^{-1} EB flow, 180 mL min^{-1} air flow at 530 °C with 15MT catalyst. Possible industrial application of xMT catalyst can be evaluated

by subjecting catalytic studies for longer TOS under the above reaction conditions, to ensure robust nature of material and obtaining constant ST yield. 15MT catalysts stability for longer duration (45 h) was studied, and the results are shown in Fig. 12. EB conversion increases from 45 to 58% at 15 h TOS, and thereafter a steady 58% EB conversion was maintained. ST yield also gradually increased from 41 to 55% and afterwards there is no decrease in ST yield up to 45 h thus demonstrating the sustainable nature of catalyst and reaction. Gradual increase in catalyst activity in the first few hours observed underwide variety of reaction conditions demonstrates a change in the nature of catalyst under reaction conditions towards higher active form of the catalyst. Both conversion and selectivity linearly increases, till the reaction reaches a steady state. ST selectivity during whole steady state was observed to be >95%.

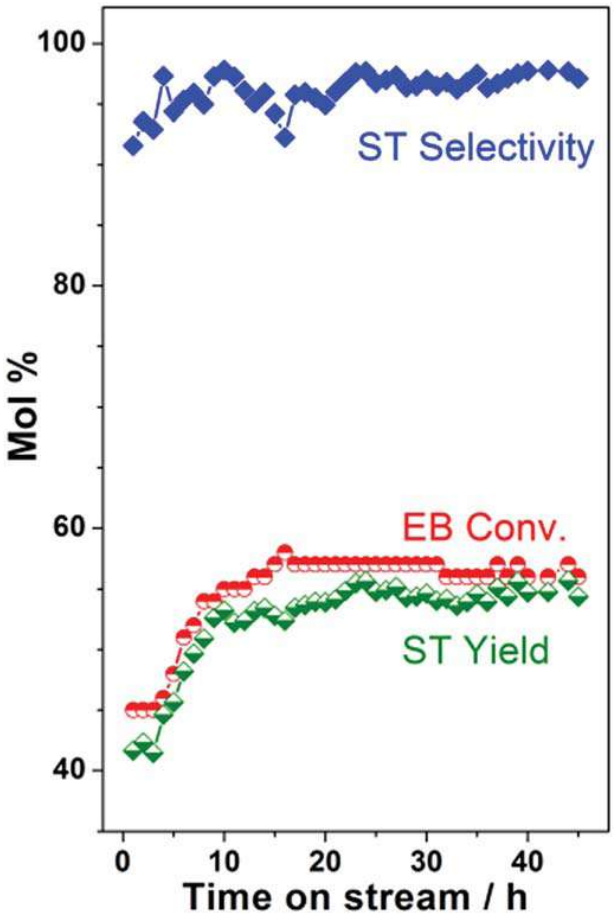

Figure 12. Catalyst stability was evaluated over 45 h; EB flow at 1.8 mL h^{-1} with optimized air flow at 180 mL min^{-1} at 530 °C over 15MT catalyst. Catalyst showed steady ST yield for whole duration without undergoing deactivation.

4.4 Spent Catalyst Analysis

After reaction, spent catalysts, those are still active and exhibit the high catalytic activity, were collected and analyzed with various physiochemical techniques, such as XRD, Raman spectroscopy, SEM, TEM, thermogravimetric and differential thermal analysis (TG-DTA). This is mainly to explore the nature of changes that happened to catalysts, especially under transient state conditions which shows an induction period. This is important, since the ODH is known to be an exothermic reaction and local hot spots on the catalyst is likely to occur, which could influence the catalyst.

4.4.1 Powder XRD

Wide angle powder XRD of spent catalysts was analyzed to understand changes in catalysts due to catalytic conversion of EB to ST. For comparison Mn_3O_4 and 5% Mn_3O_4 impregnated on TiO_2 (5% Mn_3O_4/TiO_2) catalysts powder WXRD were also recorded and shown in Fig. 13. Narrow and high intense peaks due to rutile phase of TiO_2 at 2θ = 27.5 (110), 36.3 (101), 40.9 (111), 56.8 (211) are observed due to phase change of anatase TiO_2 lattice at reaction temperatures. Mn_3O_4 (JCPDS-ICDD #24-0734) at 2θ = 37.28 and 56.90, and MnO(OH) (JCPDS-ICDD #88-0649) (an intermediate phase of Mn_3O_4), at 2θ = 23.67, 32.21, 35.07, 37.28, 39.17, 40.125, 43.932, 60.7, 64.33, 65.45 and 69.57 are also observed due to precipitation of manganese ions from TiO_2 lattice due to reaction conditions. Spent catalysts exhibit sharp narrow peaks, hinting a growth of large crystallites due to aggregation. Indeed, rutile phase grow at the cost of anatase phase, and the same is observed up to 10% Mn; MT15 shows complete conversion of anatase to rutile phase. Conversion of anatase to thermodynamically stable phase, [47] underscores the role of exothermic nature of the reaction and its influence in changing the nature of surface and bulk properties of catalyst. Nonetheless, stable catalytic activity observed for 45 h (Fig. 12) suggesting the changes cease to occur under steady state conditions. Thus it can be inferred that catalytic activity is due to Mn_3O_4 and its intermediate MnO(OH) supported over rutile titania.

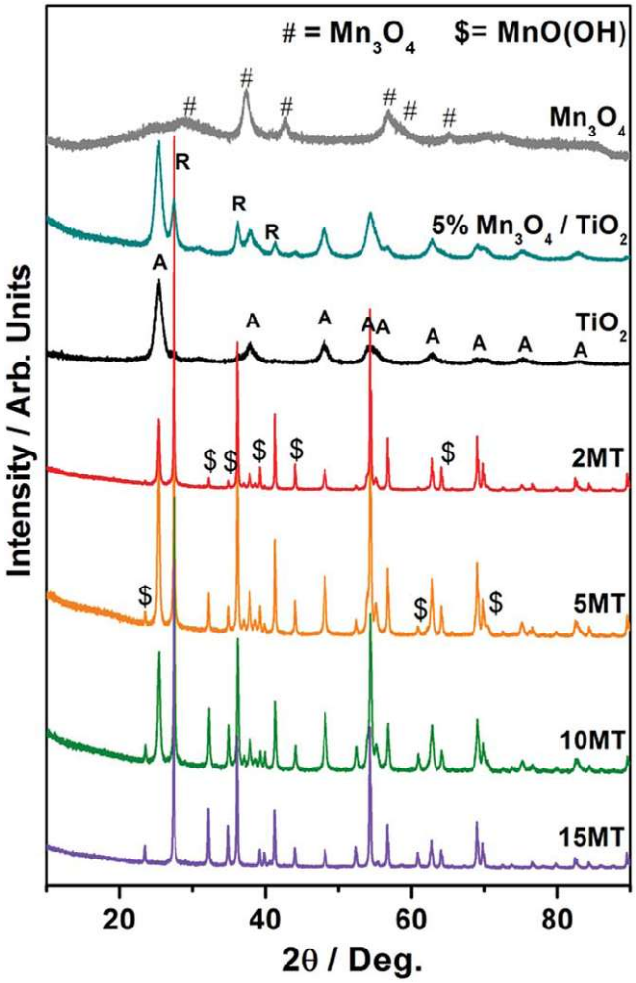

Figure 13. Powder XRD of spent catalysts and fresh TiO_2, Mn_3O_4 and 5%Mn_3O_4/TiO_2 are shown. Spent catalysts exhibits features of Mn_3O_4, MnO(OH) and rutile phase of titania and this is attributed to the exothermic nature of reaction.

4.4.2 Raman Spectra

Raman spectroscopy analyses of spent xMT catalysts were carried out and the results are shown in Fig. 14. All spent catalysts exhibited a predominant rutile phase along with minor anatase phase features of TiO_2. TiO_2 and 5% Mn_3O_4/TiO_2 catalyst's Raman spectra are given for reference. Spent catalysts exhibits significantly higher intensity compared to fresh catalysts indicating the growth of crystallites to bigger size and hence increase in crystallinity. However, no manganese oxide features appeared in spectra of any catalysts, suggesting a uniform distribution of them on the surface of titania.

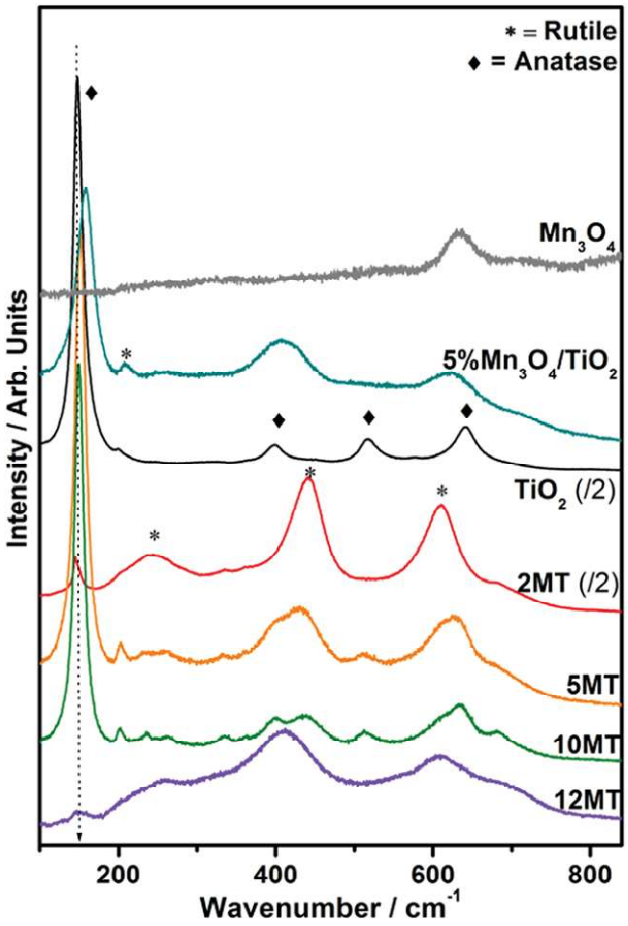

Figure 14. Raman spectra of spent catalysts exhibits peaks due to anatase and additional rutile phases of TiO_2 supporting XRD results.

4.4.3 TG-DTA

TG-DTA of spent catalysts was measured and the results are shown in Fig. 15. TG plots exhibits weight loss of 1– 3% between 200 and 400 °C, and 1–2% weight gain between 500 and 950 °C; this is in addition to the initial weight loss due to water removal below 200 °C. DTA exhibited exothermic peaks, which are due to carbon burning, that was deposited during catalytic reactions over catalysts surface. MT15 catalysts tested for 45 h shows maximum weight loss, highest peak intensity in DTA results indicating the maximum carbon deposition of 3% due to reaction. Other compositions tested for 12 h show approximately the similar amount of weight loss in TGA (Fig. 15a). In spite of some coke deposition, sustainable activity observed with 15MT at 530 °C demonstrates the utilization of air/O_2 not only towards ODH reaction, but to minimize the coked deposition. Weight gain at high temperatures is

attributed to the oxidation of manganese oxides to MnO_2. Indeed, a systematic increase in weight gain with increasing Mn-content supports the above.

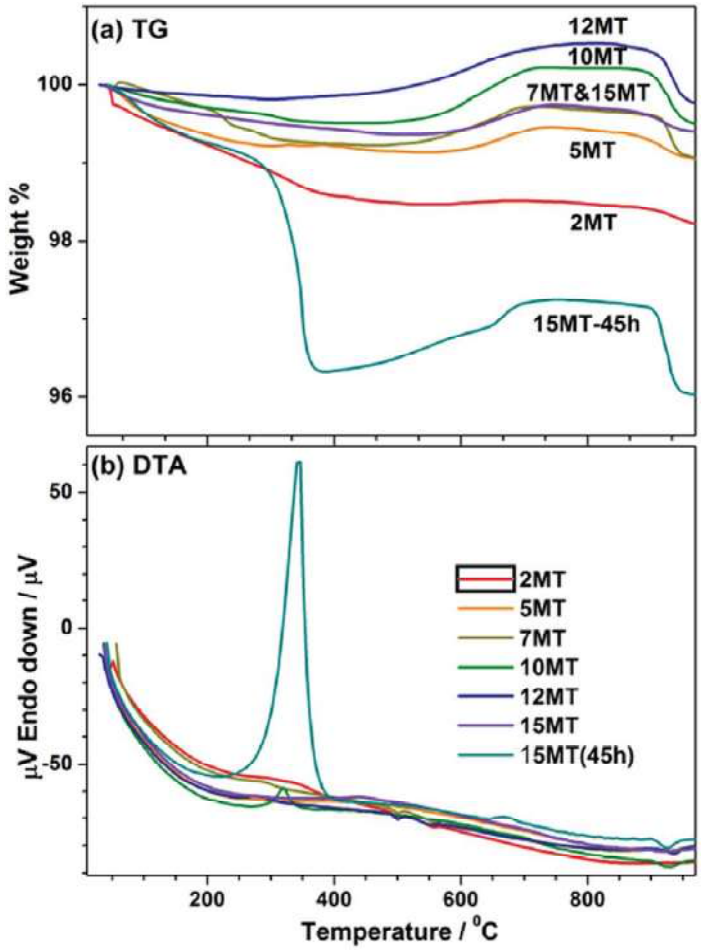

Figure 15. TG-DTA results for spent catalysts showed exothermic peaks for coke removal up to 400 °C, weight loss followed by weight gain at 700 °C. Catalysts were initially subjected to the following reaction condition at T = 500 °C; EB flow rate = 1.8 mL h^{-1}; oxygen flow rate = 40 mL min^{-1} for 12 h on TOS.

4.4.4 TEM-SEM

To understand morphological changes withthe catalyst due to reaction, electron microscopy analysis was conducted and the results are shown in Fig. 16. TEM results of spent (5MT) catalyst demonstrate agglomeration to bigger particles, compared to virgin 5MT (Fig. 2b). SEM images show random morphology, with micron size aggregates. TEM and SEM results are further supported by XRD analysis of spent

catalysts (Fig. 13) exhibiting sharp peaks due to bigger agglomerated particles of spent catalyst.

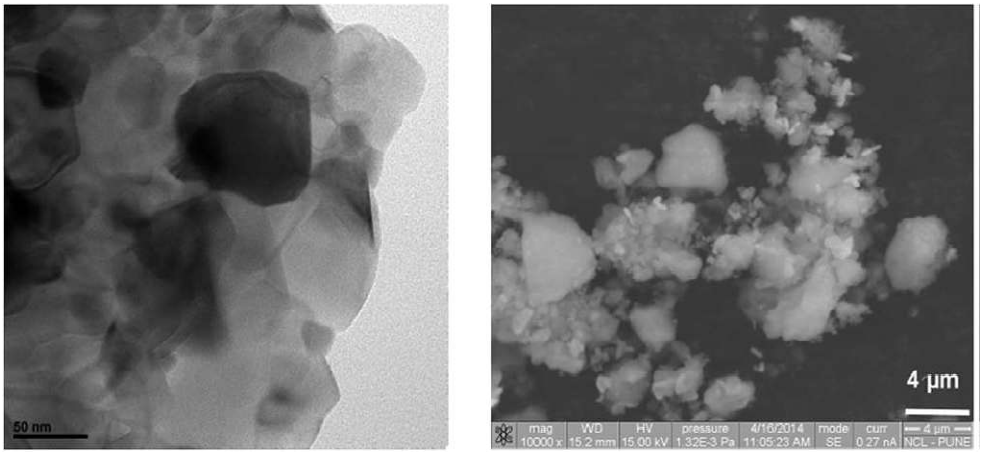

Figure 16. (a) TEM, and (b) SEM image of spent 5MT catalyst. Compared to the TEM results shown in Fig. 2, particle agglomeration is evident. Scale bar length is 50 nm for panel (a).

4.5 Mechanism For The Reaction

4.5.1 ODH with Mn_3O_4 Supported on TiO_2

In view of the above findings with spent catalysts, few control experiments were carried out with Mn_3O_4 supported on anatase phase TiO_2. Representative result is given in Fig. 17 for 5% Mn_3O_4 loaded on TiO_2 by wet impregnation method and EB to ST conversion was carried out under optimized conditions of 180 mL air per min, EB flow of 1.8 mL h^{-1} at 530 °C. Comparable ST yield observed in Fig. 7 for 5MT and Fig. 17 demonstrates the active nature of catalyst is the same in both cases. In fact, the spent catalyst analysis results are in good correlation with that of 5MT results shown in Fig. 13 and 14. It is also to be noted that the change in conversion and selectivity in Fig. 7 and 17 indicates the role of gradual change in interaction between Mn_3O_4 and titania and the conversion of anatase to rutile phase of titania. Although textural properties of nanocrystalline xMT and relatively bigger size particle of Mn_3O_4 on titania varies to a significant extent, they exhibit comparable catalytic activity indicating the minor role of textural properties for the reaction.

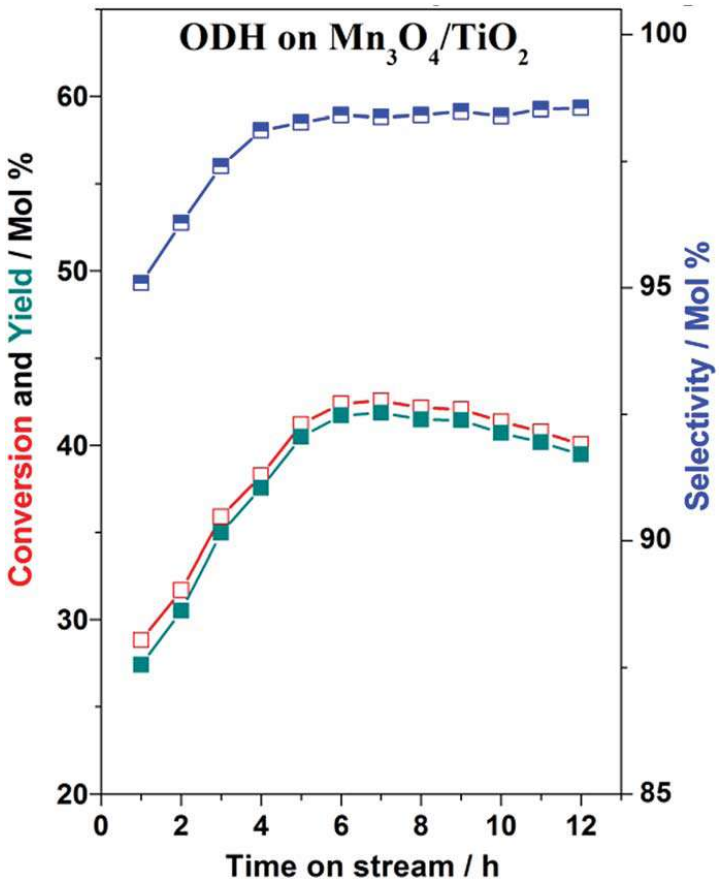

Figure 17. 5% Mn_3O_4 supported on TiO_2 evaluated for EB to ST under optimized condition with air.

4.1.1 Mars-van Krevelen (MvK) Mechanism

Kinetics and mechanism of the reaction determines the rate and distribution of products for any catalysis reaction. Different physiochemical and analytical tools helps to understand the above aspects of catalysis. In the present case, the role of lattice oxygen of xMT catalyst was explored by measuring the ODH reaction in the absence and presence of oxygen/air and a representative result is shown in Fig. 18. Surprisingly, 15MT exhibited catalytic activity of about 15% EB conversion and styrene selectivity of 95%, even in the absence of oxygen/air.

A decrease in conversion was observed from the initial 16% conversion to 14% at TOS = 8–9 h. In contrast to the general expectation of steep decline in activity in the first few hours, sustenance of catalytic activity indeed indicates the supply of lattice oxygen towards the ODH reaction. After demonstrating the sustenance of reaction for nine hours, the catalyst was calcined in oxygen (20 mL min^{-1} flow rate) at

530 °C, and EB conversion was continued with oxygen flow. An immediate jump in conversion from 14 to 35 % in the next three hours, indeed, demonstrates the sustainability of the catalyst system and ODH reaction. Above all, this observation demonstrates the lattice oxygen role in ODH reaction. This clearly indicates xMT catalysts do follow Mars–van Krevelen (MvK) mechanism [48, 49] for EB to ST conversion.

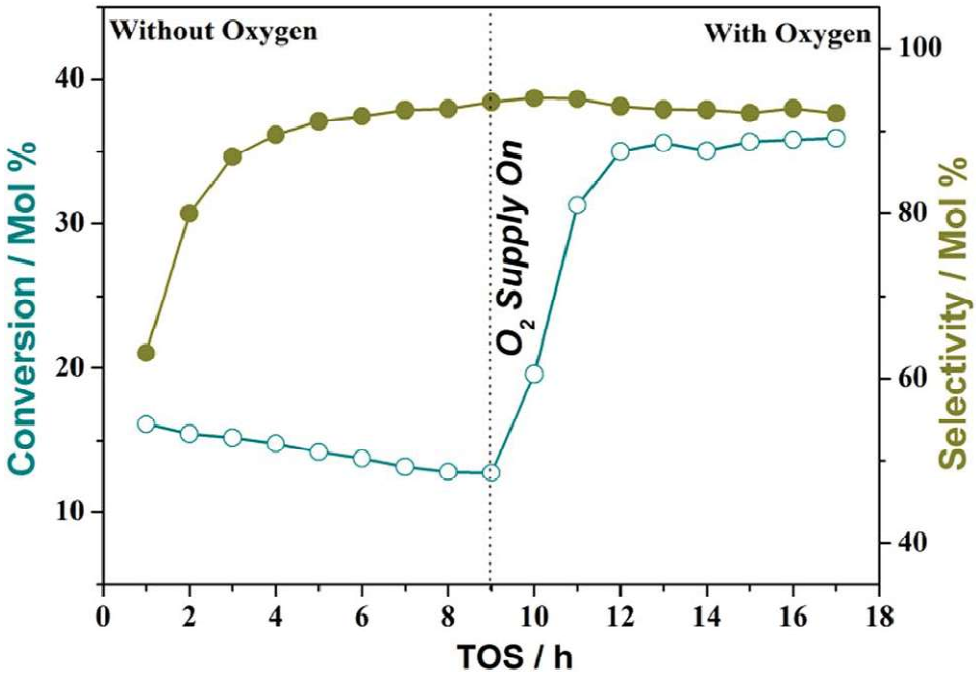

Figure 18. MT15 catalysts have been tested in absence of air for catalytic reaction at 1.8 mL EB, over 15MT catalyst at 530 °C. The MT15 catalysts regained its activity after calcination in oxygen at reaction temperature for 20 min oxygen treatment. 20 mL min^{-1} oxygen flow rate was introduced at TOS = 9 h.

4.2 Conclusions

Manganese incorporated in disordered mesoporous nanocrystalline titania catalysts were synthesized by simple solution combustion method. $Mn_xTi_{1-x}O_2$ materials were characterized via XRD, EDX, Raman spectroscopy and HRTEM techniques. $Mn_xTi_{1-x}O_2$ catalysts were evaluated for EB to ST conversion by ODH route. The green chemistry approach using air or O_2 as oxidant was adopted and also it's more economical and safer approach for the conversion. Optimum air flow and EB flow for EB to ST conversion was found to be 180 mL min^{-1} and 1.8 mL h^{-1}, respectively, with

15MT composition exhibiting the highest and sustainable activity at optimum reaction temperature of 530 °C. Robust and sustainable nature of the catalyst was demonstrated by activity for 45 h. Conversion temperature is lowered for ST synthesis with high and sustainable yield. Catalyst is stable and active for long period of time. $Mn_xTi_{1-x}O_2$ materials operate via Mars–van Krevelen mechanism as confirmed by catalytic studies in absence/presence of oxygen.

Spent catalyst analysis shows that active phase of catalyst is Mn_3O_4 supported over rutile TiO_2. Indeed, there is a structural change occurs from anatase to rutile in the first few hours of reaction, due to exothermic nature of reaction. Nonetheless, the sustainable activity observed for 45 h demonstrates the importance of thermodynamically stable rutile phase as support with Mn_3O_4 as the active catalyst. Compared to the systems reported in the literature, [8–21] Mn_3O_4 supported over rutile TiO_2 is attractive, especially in terms ofstability, and yield.

4.3 References

1. M. Chanda, S. K. Roy, *Industrial Polymers, Specialty Polymers and Their Applications,* CRC Press 305 (2008).
2. H. A. Wittcoff, B. G. Reuben, J. S. Plotkin, *Industrial Organic Chemicals*, John Wiley and sons, Hoboken, New Jersey, (2013)180.
3. H. H. Szmant, *Organic Building Blocks of the Chemical Industry*, John Wiley and sons, (1989) 431.
4. M. Muhler, J. Schutze, M. Wesemann, T. Raymant, A. Dent, R. Schlogl, G. Ertl, *J. Catal.*, (1990) **126** 339-360.
5. G. P. Chiusoli, P. M. Maitlis, *Metal-catalysis in industrial organic processes*, 109 (2008).
6. Y. She, J. Han, Y.H. Ma, *Catal. Today*,(2001) **67** 43-53.
7. J. C. S. de Araujo, C. B. A. Sousa, A. C. Oliveira, F. N. A. Freire, A. P. Ayala, A. C. Oliveira, *Appl. Catal., A*, (2010) **377** 55-63.
8. C. Nederlof, V. Zarubina, I. Melian-Cabrera, H. J. Heeres, F. Kapteijn, M. Makkee, *Catal. Sci. Technol.*, (2013)**3** 519-526.
9. N. V. Qui, P. Scholz, T. F. Keller, K. Pollok, B. Ondruschka, *Chem. Eng. Technol.*, (2013) **36** 300-306.

10. R. Watanabe, M. Ikushima, K. Mukawa, F. Sumomozawa, S. Ogo, Y. Sekine, *Front. Chem.*, (2013) **21** 1-11.
11. A. K. Venugopal, A. T. Venugopalan, P. Kaliyappan, T. Raja, *Green Chem.*, (2013) **15** 3259-3267.
12. V. K. Nguyen, J. H. Park, C. H. Shin, *Korean J. Chem. Eng.*, (2014) **31** 582-586.
13. K. Sivaranjani, A. Verma, C. S. Gopinath, *Green Chem.*, (2012) **14** 461-471.
14. C. Nederlof, V. Zarubina, I. V. M. Cabrera, E. H. J. Heeres, F. Kapteijn, M. Makkee, *Appl. Catal., A*, (2014) **476** 204-214.
15. N. T. Thao, H. H. Trung, *Catal. Commun.*, (2014) **45** 153-157.
16. P. Kustrowski, L. Chmielarz, R. Dziembaj, P. Cool, E. F. Vansant, *J. Phys. Chem. A,*(2005) **109** 330-336; K. Thirunavukkarasu, K. Thirumoorthy, J. Libuda, C.S. Gopinath, *J. Phys. Chem. B*, (2005) **109** 13272-13282.
17. M. C. Rangel, A. P. M. Monteiro, S. G. Marchetti, S. B. Lima, M. S. Ramos, *J. Mol. Catal. A: Chem.*, (2014) **387** 147-155.
18. S. S. Negi, K. Sivaranjani, A. P. Singh, C. S. Gopinath, *Appl. Catal., A*, (2013) **452** 132-138.
19. Q. Wang, X. Li, W. Li, J. Feng, *Catal. Commun.*,(2014) **50** 21-24.
20. D. Sannino, V. Vaiano, P. Ciambelli, *Res. Chem. Intermed.*, (2013) **39** 4145-4157.
21. N. R. Shiju, M. Anilkumar, S. P. Gokhale, B. S. Rao, C. V. V. Satyanarayana, *Catal. Sci. Technol.*, (2011) **1** 1262-1270.
22. R. Crăciun, N. Dulămită, *Ind. Eng. Chem. Res.*, (1999) **38** 1357–1363.
23. D. G. Kulkarni, A. V. Murugan, A. K. Viswanath, C. S. Gopinath, *J. Nanosci. Nanotechnol.*, (2009) **9** 371-377.
24. T. Mathew, K. Sivaranjani, E. S. Gnanakumar, Y. Yamada,T. Kobayashi, C. S. Gopinath, *J. Mater. Chem.*, (2012) **22** 13484-13493.
25. K. Sivaranjani, S. RajaAmbal, T. Das, K. Roy, S. Bhattacharyya, C. S. Gopinath, *ChemCatChem*, (2014) **6** 522-530.
26. M. Mapa, C. S. Gopinath, *Chem. Mater.*, (2009) **21** 351-359.
27. M. Mapa, K. Sivaranjani, D. S. Bhange, B. Saha, P. Chakraborty, A. K. Viswanath, C. S. Gopinath, *Chem.Mater.*, (2010) **22** 565-578.

28. M. Mapa, K. S. Thushara, B. Saha, P. Chakraborty, C. M. Janet, R.P. Viswanath, C. M. Nair, K. V. G. K. Murty, C. S. Gopinath, *Chem. Mater.*, (2009) **21** 2973-2979.
29. K. Sivaranjani, C. S. Gopinath, *J. Mater. Chem.*, (2011) **21** 2639-2647.
30. S. Velu, N. Satoh, C. S. Gopinath, K. Suzuki, *Catal. Lett.*,(2002) **82** 145-152.
31. S. Velu, K. Suzuki, C. S. Gopinath, *J. Phys. Chem. B*, (2002) **106** 12737-12746.
32. M. K. Dongare, V. Ramaswamy, C. S. Gopinath, A. V. Ramaswamy, S. Scheurell, M. Brueckner, E. Kemnitz, *J. Catal.,*(2001) **199** 209-216.
33. S. Velu, K. Suzuki, M. Vijayaraj, S. Barman, C. S. Gopinath, *Appl. Catal., B*, (2005) **55** 287-299.
34. N. R. Shiju, M. Anilkumar, S. P. Mirajkar, C. S. Gopinath, C.V. Satyanarayana, B. S. Rao, *J. Catal*., (2005) **230** 484-492.
35. T. Mathew, Y. Yamada, A. Ueda, H. Shioyama, T. Kobayashi, C. S. Gopinath, *Appl. Catal., A*, (2006) **300** 58-66.
36. P. Maity, C. S. Gopinath, S. Bhaduri, G. K. Lahiri, *Green Chem.*, (2009) **11** 554-561.
37. T. Rajesh, A. K. Rajarajan, C. S. Gopinath, R. N. Devi, *J. Phys. Chem. C*, (2012) **116** 9526-9532.
38. A. C. S. Sekhar, K. Sivaranjani, C. S. Gopinath, C. P. Vinod, *Catal. Today*, (2012) **198** 92-97.
39. K. Roy, C. P. Vinod, C. S. Gopinath, *J. Phys. Chem. C*,(2013) **117** 4717; K. Roy, C. S. Gopinath, *Anal. Chem.*,(2014) **86** 3683-3687.
40. P. Devaraji, N. K. Sathu, C. S. Gopinath, *ACS Catal.*, (2014) **4** 2844-2853
41. N. Maity, P. R. Rajamohanan, S. Ganapathy, C. S. Gopinath, S. Bhaduri, G. K. Lahiri, *J. Phys. Chem. C*, (2008) **112** 9428-9433.
42. A. Lazar, W. R. Thiel, A. P. Singh, *RSC Adv.*, (2014) **4** 14063-14073.
43. E. S. Gnanakumar, J. John, T. Raja, C. S. Gopinath, *J. Nanosci. Nanotechnol.*, (2013) **13** 2682-2688.
44. M. Satish, R. P. Viswanath, C. S. Gopinath, *J. Nanosci. Nanotechnol.*, (2009) **9** 423-432.
45. S. Bag, K. Roy, C. S. Gopinath, C. R. Raj, *ACS Appl.Mater. Interfaces*, (2014) **6** 2692-2699.

46. B. Murugan, D. Srinivas, C. S. Gopinath, V. Ramaswamy, A. V. Ramaswamy, *Chem. Mater.*, (2005) **17** 3983-3993.
47. C. S. Gopinath, T. Raja, *J. Phys. Chem. B*, (2001) **105** 12427-12428; B. Naik, K. M. Parida, C. S. Gopinath, *J. Phys.Chem. C*, (2010) **114** 19473-19482.
48. P. Mars, D. W. V. Krevelen, *Chem. Eng. Sci.*, (1954) **3** 41-59.
49. C. Doornkamp, V. Ponec, *J. Mol. Catal. A: Chem.*, (2000) **162** 19-32.

Chapter V: Synthesis Characterization and Photocatalytic Studies of H-TiO_2 Materials

5.1 Introduction

Energy demands by human kinds are ever increasing, and the extent of energy requirement is increasing very rapidly in the last couple of decades. Conventional fossil fuels are used to its fullest possibility; however, this leads to its depletion at a steep rate. This demands a lot of pressure on all alternate fuels or nonconventional energy sources to meet the increasing power demands of present as well as future [1]. Abundant solar radiation is falling on the earth surface and can be used as one of the sustainable alternate energy resource for future [2]. Solar light falling on the earth surface is composed of 4 - 5% UV, 45 % visible and 50 % infrared (Near IR, IR and Far IR) fraction of spectrum [3]. Hydrogen production via photocatalytic splitting of water will be an excellent option for setting up much talked about future hydrogen economy [4]. We believe, any breakthrough development in the area of solar light to energy/fuel conversion will be immediately and very likely considered for the Nobel Prize [5]. Dye sensitized solar cell is also a simple energy conversion alternate to be used increasingly in the future [6]. Many efforts are going on various aspects of solar cell, to improve the efficiency of devices [7].

Unprecedented research efforts are deployed to convert major fraction of solar energy, mainly of visible and near IR radiation, to energy/fuel with variety of materials [8]. A simple literature search shows the number of research articles and patents based on TiO_2 are much higher than any other material [9]. Among the semiconductor photocatalysts, TiO_2 has been acknowledged to be the best due to its chemical stability towards photocorrosion and holes produced by photons in titania have high oxidizing ability [10]. TiO_2 is known to be an excellent semiconductor photocatalyst for water splitting via ultraviolet (UV) light. Indeed, Fujishima and Honda demonstrated the first water splitting by photoelectrochemical means, as early as 1972 [11]. TiO_2 is apt semiconducting material because of its favorable band-edge positions, strong optical absorption, readily available, bio compatible, photo stable; but due to its large band gap, and fast electron-hole recombination due to a high density of trap states most of the sunlight is left unused [12]. Many techniques are used, such as use of co-catalysts [13], quantum dots for sensitization [14], forming composites [15] and band gap reduction [16] to use visible and IR region photons of solar spectrum by these wide band gap materials [17]. However, these methods have drawbacks as defect sites are generated due to foreign materials and solar light

conversion efficiency has not increased sufficiently to move towards practical applications [18]. Instead of adding many different components to titania, can we enhance the visible light absorption and hence water splitting activity of titania. In this direction, Chen and Mao on 2011 showed that hydrogen treatment of TiO_2 leads to band gap reduction [19]. Ambient and high pressure hydrogen treatment to titania leads to partial reduction, which creates oxygen vacancies and Ti^{3+} also appears. Indeed, the colour drastically changes from color-less for virgin titania to blue-black colour titania upon reduction treatment. Due to the colour associated, it is popularly known as blue or black titania in the literature [20].

Water splitting and DSSC are excellent solar harvesting techniques. H_2 is carbon free fuel with very high energy density and water as only combustion product [21]. Currently hydrogen is produced via reforming of fossil fuels; however, the alternate green method of water splitting is yet to mature with significant efficiency [22]. Highly efficient photocatalysts are urgently needed to be developed. A thorough understanding of the photocatalysis should also be parallelly made. Currently silicon solar cells are used for solar to electricity conversion but are of significantly high cost, along with the disposal problems of silicon after its lifetime [23]. Alternate cheaper, simple, better and efficient energy conversion technique are needed. DSSC is comparatively cheap and easy technology to use for conversion of solar energy to electrical energy. Better fabrication techniques with newer functional materials are sought after for higher efficiencies. Efforts are made to develop understanding of device problems to increase efficiency of DSSC [24].

For the present chapter, we have synthesized reduced and self-doped, disordered mesoporous titania TiO_2 by hydrogen gas treatment at high temperatures, and at ambient to high pressures. This material is denoted as H-TiO_2. H-TiO_2 materials were characterized via various physiochemical techniques to understand structural and textural features. Generated Ti^{3+} has electronic configuration of $Ti3d^1$, which indicates an electronic state should be available within the band gap of titania. Conduction band of titania is mainly made of Ti 3d levels and hence the $3d^1$ state is expected to be close to the conduction band. H-TiO_2 materials were used for hydrogen production under AM1.5, and UV light sources. H-TiO_2 shows better results for hydrogen production than commercial P25 via water splitting. DSSC, were fabricated using reduced titania as anode material, various cell parameters are optimized. Prepared solar cells were characterized using various techniques such as JV plot,

electrochemical impedance spectroscopy, FESEM and incident photon conversion efficiency (IPCE). Present work demonstrates that hydrogen treatment is a simple and general strategy which can considerably improve their (anode material) features such as, absorbance in visible light region. Prepared materials have high donor density, high current density, and low recombination/trap centers with lower electron-hole recombination correlated to show higher performance.

5.2 Results and Discussion

5.2.1 X-Ray Diffraction

Materials are prepared at high temperature conditions under ambient and high H_2 pressures, the materials are denoted as 20B, 25AP, 30AP, 40AP and T0. T0 represent unmodified TiO_2 prepared via solution combustion synthesis with 1:1 ratio of titanium nitrate: urea. 25AP, 30AP and 40AP are prepared via modified T0 under ambient pressure H_2 treatment at 250, 300 and 400 °C temperatures respectively, for 8 hours, while 20B was prepared at 20 bar Hydrogen pressure under 200 °C for 10 hours.

To understand the structural characteristics of hydrogenated titania, powder XRD analysis was carried out for the materials. For comparison XRD of untreated TiO_2 is also shown in the figure 1. Peaks at 25.2, 37.8, 48.2, 54.2, 55.2, 62.8, 68.9, 75.2, and 82.7 2θ corresponds to (101), (004), (200), (105), (211), (204), (116), (220) and (215) facets of anatase structure as indexed to JCPDS file no 21-1272, 12-1276. As the reduction temperature increases from 250 (25AP) to 400 °C (40AP) at ambient H_2 pressure, the percent of rutile phase increases. Indeed 40AP exhibit sharp, narrow and intense rutile peaks at 27.3, 36.0, 41.2, and 56.6° 2θ values, indicating the growth of rutile phase at the expense of anatase under the preparation conditions. New rutile peaks features also appeared for 25AP, 30AP, and 20B materials. Although rutile content did not increase quite dramatically at twenty bar H_2 pressure at 200 °C, a significant broadening of many anatase features can be seen in Figure 1. Anatase and rutile phase percentages for the materials were calculated and shown in Table 1. 25AP, 30AP, 20B exhibits broad natured peaks, while 40AP exhibit sharp peaks.

Particle sizes were calculated using Scherer equation for H-TiO_2 materials, and shown in table 1.

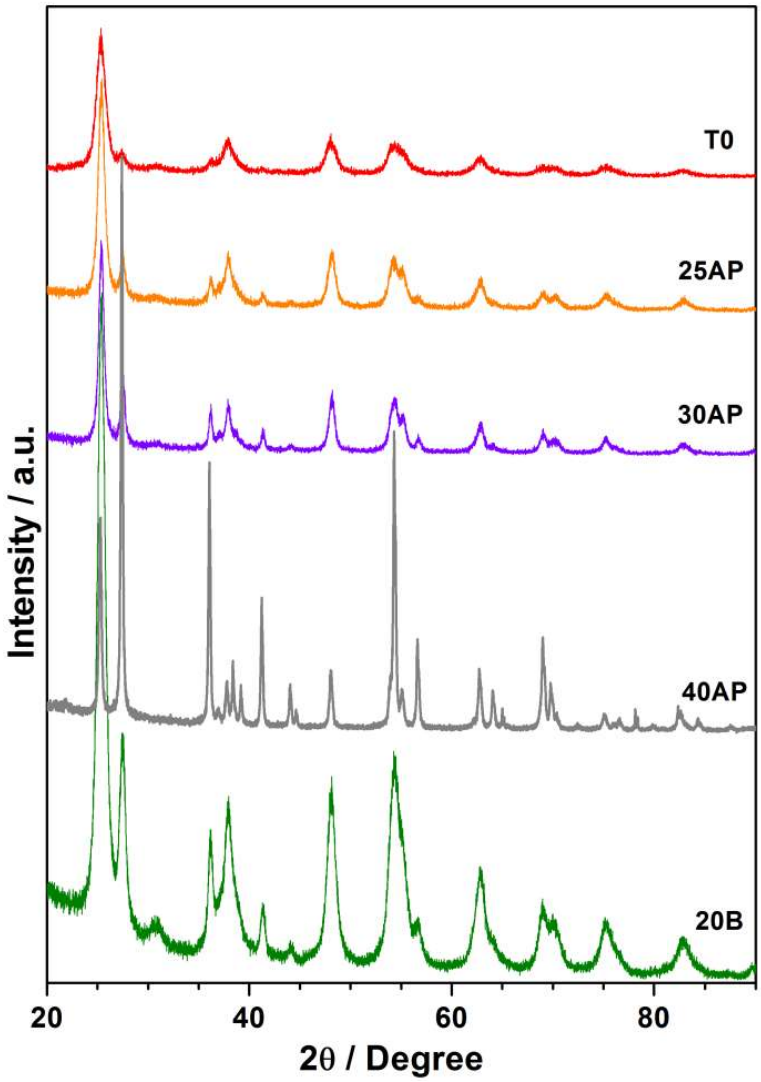

Figure 1. Wide angle powder X-ray diffraction for H-TiO_2 catalysts is shown; XRD pattern of parent TiO_2 is also shown for comparison. After H_2 treatment prepared 20B material exhibits broad peaks, 40AP have predominantly rutile phase, 30AP and 25AP have developed few percentage of rutile phase.

5.2.2 **Raman Spectroscopy**

To understand the vibrational features and the structural and/or coordination features, Raman spectra of all materials were recorded. Raman spectra are shown in figure 2; for comparison TiO_2 spectra is also included. No significant effect on peak intensity of H-TiO_2 materials is observed; in fact, this indicates no break in the long range

ordering of Ti-O-Ti feature even after H_2 treatment. All Raman features are observed at the same wave number as that of parent P25 titania. This also indicates a partial reduction of titania do not seem to affect the structure significantly. New rutile features appeared for H-TiO_2 materials after hydrogen treatment; also all five anatase modes are observed. Raman modes of rutile phase increased significantly for 25AP, 30AP and 20B materials; 40AP material exhibit very high rutile phase intensity at the expense of anatase phase peaks. This is in very good agreement with XRD results, suggesting the phase change occurs on reduction treatment.

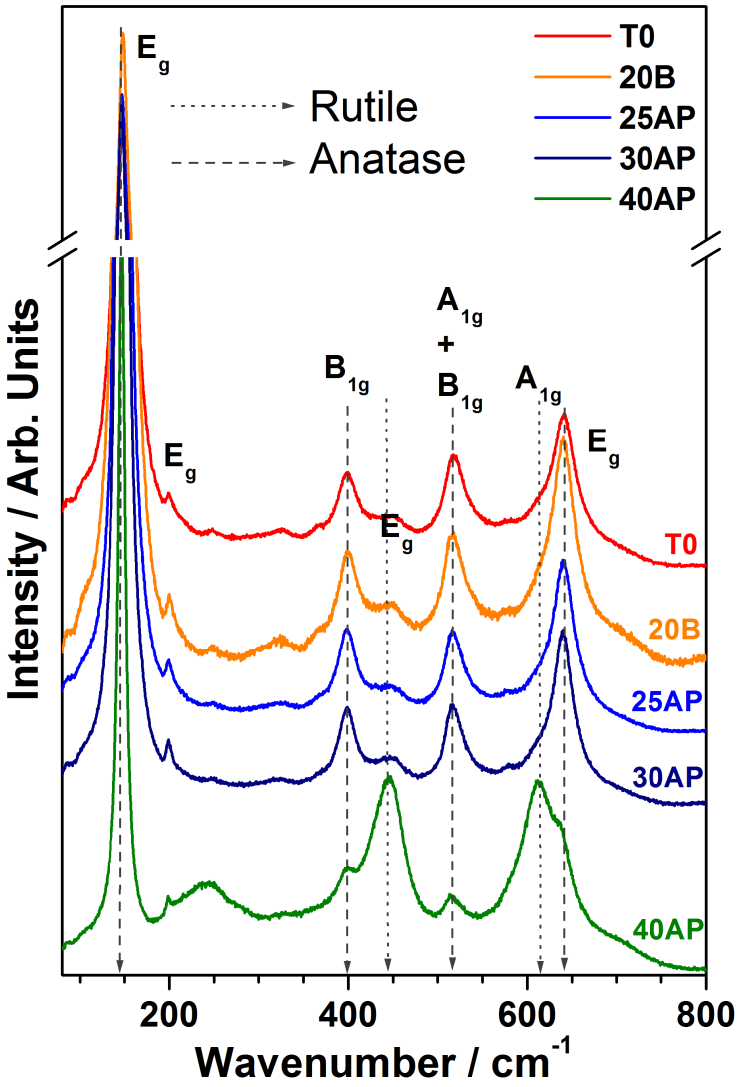

Figure 2. Raman spectra of H-TiO_2 materials are taken; Raman spectrum of TiO_2 is included for comparison. 40AP exhibits mostly rutile phase, for 30AP, 25AP, and 20B materials also rutile percentage increased after H_2 treatment. Rutile and anatase features are indicated by dotted and dashed arrows, respectively.

5.2.3 X- Ray Photoelectron Spectroscopy

Electronic structures of H-TiO_2 materials were analyzed via X-ray photoelectron spectroscopy. XPS spectra are plotted in Figure 3. Binding energy (BE) of Ti 2p and O 1s for T0, 25AP, 30AP, 40AP and 20B were measured. $Ti2p_{3/2}$ core level BE appears at 459.1 eV for TiO_2, which is in agreement with many literature studies [25]. However, upon hydrogen reduction treatment, there is a gradual shift in the BE is observed up to 458.2 eV for 20B sample. Ti $2p_{3/2}$ BE shifts gradually with increasing hydrogen treatment temperature at ambient pressure. Typical Ti $2p_{3/2}$ BE for titanium nitride has been reported to be 457 eV [26]. However, a gradual shift towards lower BE in the present case, suggests a significant decrease in the average oxidation state and it is between 3+ and 4+.

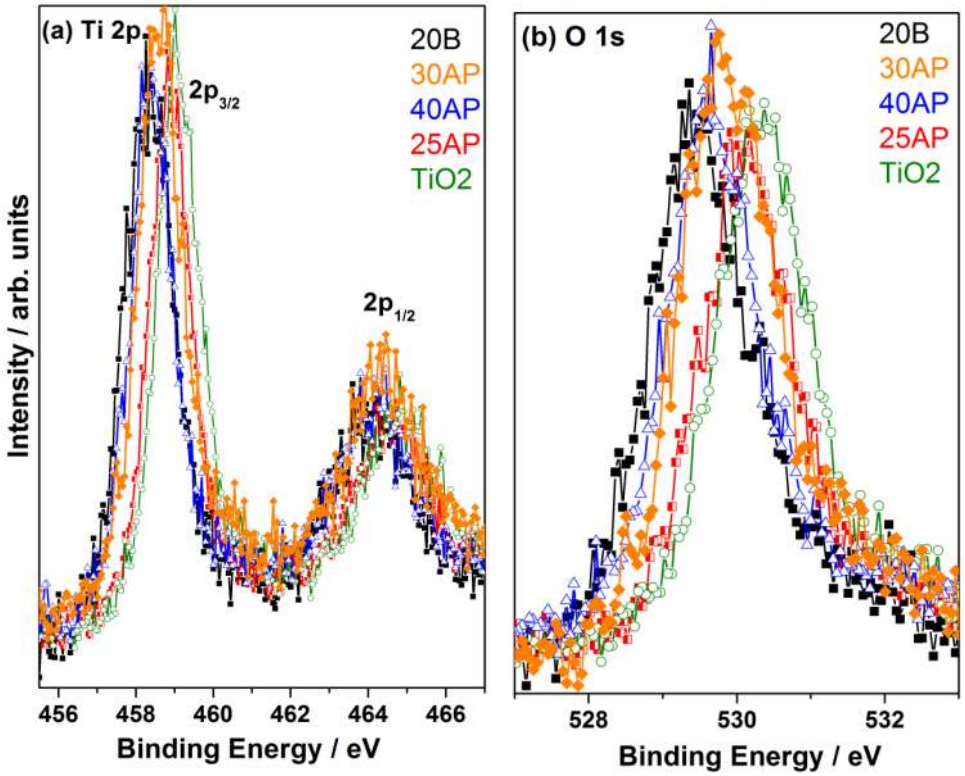

Figure 3. XPS recorded for **(a)** Ti2p and **(b)** O1s core level orbitals of H-TiO_2 materials. A gradual shift in BE towards lower energy has been observed from T0 to 20B for both Ti 2p and O 1s core levels.

It is also interesting to note that the O1s BE shifts gradually as in the case of Ti 2p. Although Ti and O are cation and anion, respectively, shift in BE towards lower BE in both cases indicates an overall increase in electron density around both the ions. O 1s

BE was observed at 530.3 eV for T0, while that of 20B appears at 529.5 eV. Due to the hydrogen reduction, there is a systematic removal of oxygen anions leading to an overall increase in charge density around the whole system.

5.2.4 UV-Visible Spectroscopy

UV-Visible diffuse reflectance spectroscopy (DRS) analysis was carried out to understand the light absorption characteristics and to calculate the band gap for hydrogenated (H-TiO_2) catalyst materials. Tauc's plots (Kubelka-Munk unit) were drawn from DRS (UV visible) data for the materials in Figure 4. Band gap for H-TiO_2 catalysts were estimated via drawing tangent on vertical section of spectrum, energy where the tangent are cutting on x axis are calculated. H-TiO_2 materials show extended continuous absorption into visible region. Calculated band gap from the plot for T0 is 3.10 eV, 2.94 eV for 30AP, 2.97 eV for 25AP, 2.82 eV for 20B and 2.89 eV for 40AP. In addition to this, certain observations are interesting and worth to be underscored.

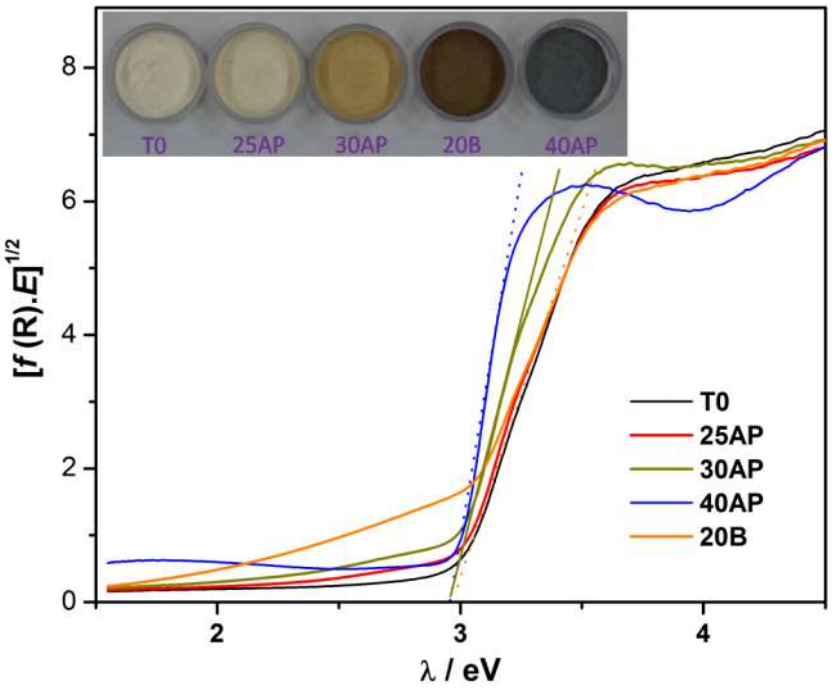

Figure 4. Tauc's plots of all H-TiO_2 catalysts are shown; H-TiO_2 materials exhibits enhanced absorption in the visible region of spectra. Inset shows a digital photograph to show the change in color associated with different materials.

20B material exhibits visible light absorption up to 1.7 eV or λ = 730 nm. All ambient H_2 pressure treated materials at different temperatures also show visible light absorption between the photon energy of 2 and 3 eV. A wide change in color associated with different H-TiO_2 materials underscores the changes in electronic states. Above analysis indicates the possibility of electronic state(s) lying between the valence and conduction bands with different density of states created due to reduction. These are the states responsible for visible light absorption and likely to help for water splitting activity.

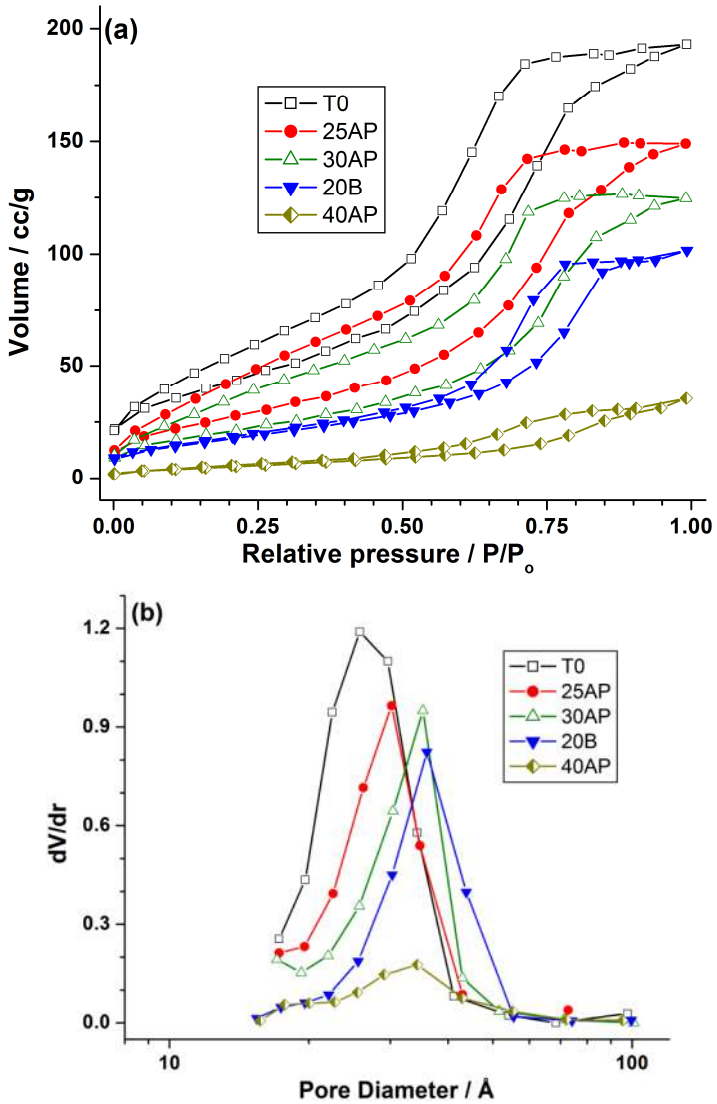

Figure 5. N_2 physisorption analyses were made for H-TiO_2 catalysts; (a) BET isotherms and (b) BJH pore size distribution are plotted. H-TiO_2 materials exhibit type IV isotherm with H2 hysteresis loop.

5.2.5 N_2 Physisorption

Textural features of the materials were analyzed via N_2 absorption-desorption isotherm studies. Isotherm and pore size distribution of T0 is also included in Figure 5 for comparison. All materials exhibited type IV isotherm with H2 hysteresis loop, indicating all of the materials exhibiting mesoporosity. Surface areas were also calculated for the materials via using BET method are shown in table 1. 40AP and 20B generated after hydrogenation of T0 shows decrease in surface area, other materials i.e. 25AP and 30AP also shows decrease in surface area. Pore size distribution was calculated by BJH method, and the results are shown in Figure 5 and Table 1. Pore volume also decreased for H-TiO_2 materials. A detailed analysis of adsorption isotherms and pore size distribution indicates the following: As the severity of hydrogen treatment pressure and temperature increases, the surface area decreases along with an increase in pore diameter. 40AP exhibits the lowest surface area and 20B and 40AP shows the highest pore diameter. Highest crystallite size observed with 40AP explains the reason for reduction in surface area; due to the highly crystalline nature and bigger crystallite as well as particle sizes, there is a reduction in surface area. 20B also shows next significantly lower surface area and this is also attributed to the severity of high pressure reduction at 20 bar. Nonetheless, in spite of the severity of hydrogen treatment, unimodal pore size distribution is observed. Partly it is due to conversion of anatase to rutile.

Table 1. Physicochemical properties of H-TiO_2 catalysts.

Catalyst	Rutile %	Surface Area **(m^2/g)**	Pore size **(nm)**	Pore volume **(cc/g)**	Crystalline size **(nm)**
T0	3.7	154	2.5	0.29	8.8
20B	14.2	68	3.6	0.15	10.8
25AP	8.5	97	3.0	0.23	15.4
30AP	18.0	77	3.5	0.19	23.7
40AP	68.0	21	3.4	0.05	33.2

5.2.6 Linear Sweep Voltammetry

Linear sweep voltammetry (LSV) has been studied for all materials, in dark as well as in the presence of light (AM1.5) radiation on the materials. Electrodes were prepared via drop casting of isopropanol solution of catalyst materials over FTO glass plates;

LSV studies were carried out by dipping electrodes into 0.5 M NaOH electrolyte solution. Potential was varied between the electrodes from -0.4 to 0.4 V and scanned at a rate of 2 mV/s. Recorded LSV results are shown in Figure 6. All materials show an increase in current with voltage ramping. No current was observed in dark for T0; a small amount of current observed in simulated sunlight (AM1.5 light) for T0 is attributed to current generation from rutile phase. At zero applied bias also materials exhibited significant current density for all materials. 20B shows the highest photocurrent generation in the entire range of voltage ramping highlighting the relevance of hydrogen treated materials for light harvesting.

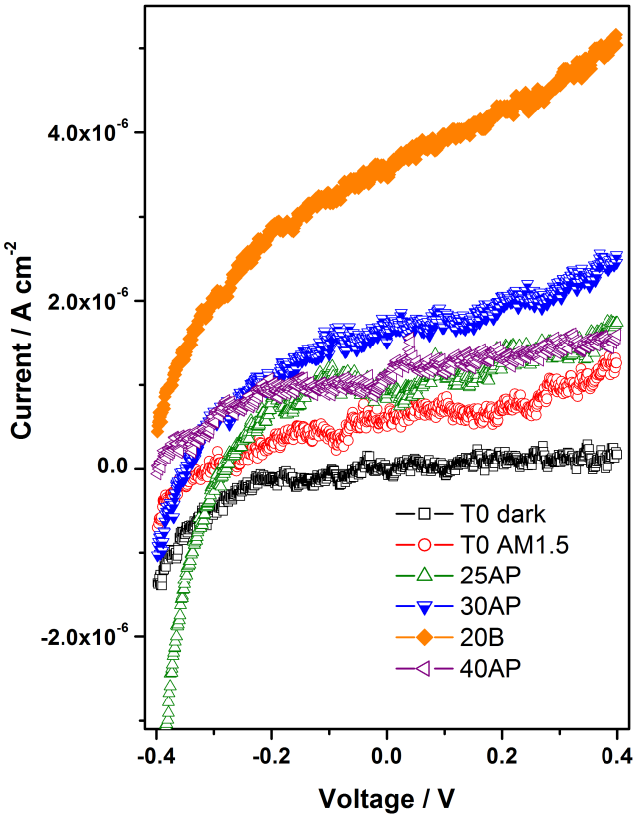

Figure 6. Linear sweep voltammetry results for untreated and H-TiO_2 materials are recorded under dark and AM1.5 light. H-TiO_2 materials exhibit significant photocurrent in the scan region of -0.4 to 0.4 V. 20B material shows the highest photocurrent generation and the highest photocurrent value at zero applied bias.

5.2.7 Photoluminescence

Steady-state fluorescence studies were conducted on a Horiba Jobin Yvon Fluorolog 3 spectrophotometer with a 450 W xenon lamp. Throughout the experiments, emission and excitation slit width was maintained at 1 nm, and the data were collected in "S1/R1" mode. Samples were powder in nature. PL was recorded to understand the charge recombination of H-TiO_2 materials. A broad emission peak at 440 nm were observed for all materials, but intensity decreases in the order of T0>20B>25AP>30AP>40AP. A huge intense and additional peak at 520 nm was observed for 20B indicating generation of oxygen vacancy after the H_2 treatment. Indeed, a similar but minor peak was observed at 520 nm for 40AP.

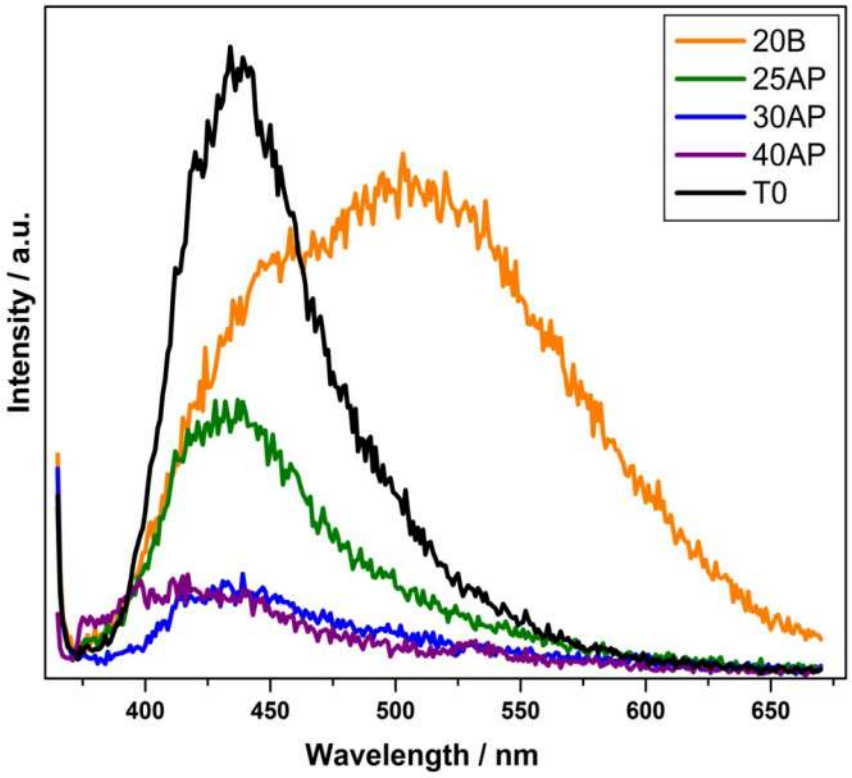

Figure 7. Emission spectra for H-TiO_2 materials.

It is to be noted that the oxygen vacancy sites are expected due to hydrogen reduction treatment. Recombination is reduced for the modified materials thus affecting the lifetime of generated charge carriers and thus photocatalytic activity of the materials.

5.3 Solar Harvesting Techniques

5.3.1 Water Splitting Studies for Hydrogen Production

Various H-TiO_2 catalysts were evaluated for H_2 production in order to understand their catalytic activity. Particularly to check influence of generated Ti^{3+} species and reduced band gap of materials. Effect of light source/band gaps in materials, were explored by changing the light sources. 25 % methanol in water under different light sources; Methanol is used as hole scavenger in the photocatalysis. Results of hydrogen production are shown in figure 8 for 25 wt% methanol solution under both UV and AM1.5 light sources. Under UV light, 20B exhibit 550 µmol/g h H_2 evolution followed by 30AP which produced 300 µmol/g h hydrogen gas, followed by both 25AP and 40AP exhibiting nearly 255 µmol/g h H_2 production value, while T0 material showed minuscule H_2 evolution (210 µmol/g) for 4 h.

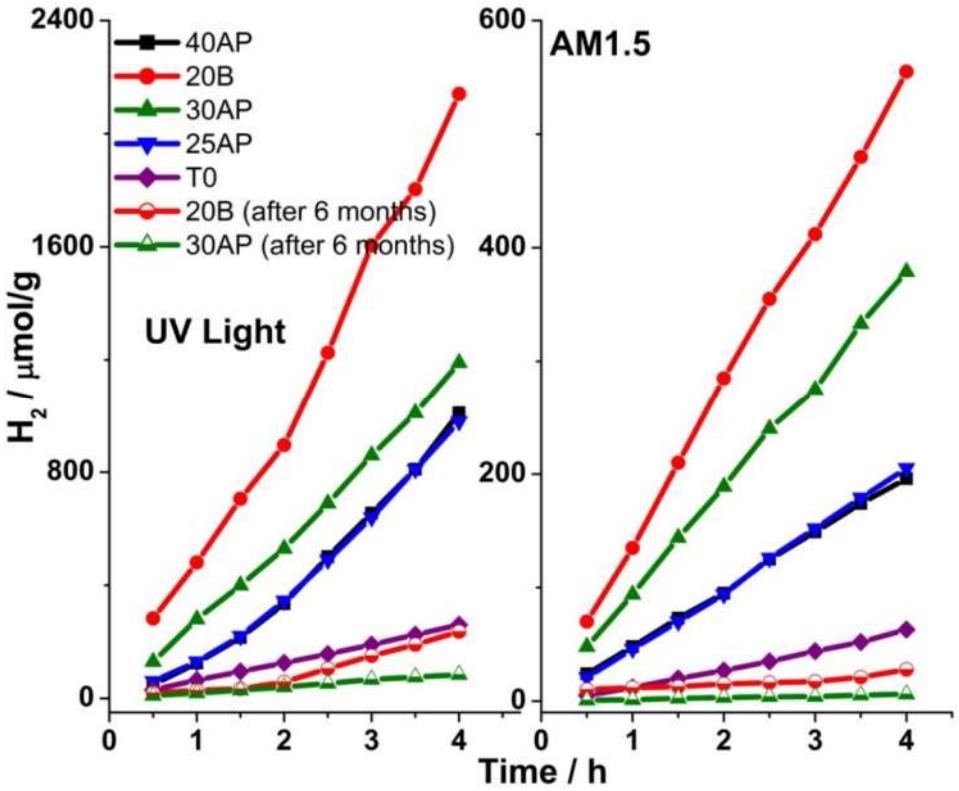

Figure 8. Hydrogen generation results from 25 wt% methanol solution in water, under UV and AM1.5 light sources for fresh and after six month H-TiO_2 catalysts.

Under AM1.5 filtered light source, the same trend in hydrogen yield was observed as that in UV light. 20B exhibit the highest H_2 evolution of 140 μmol/g h followed by 30AP which produced 90 μmol/g h hydrogen gas, followed by both 25AP and 40AP exhibiting nearly 50 μmol/g h H_2 production value, while T0 material showed 15 μmol/g h H_2 evolution.

Contrary to literatures reports of high stability of these materials [27], we found that these materials have low shelf life. Hydrogen reduced titania materials were stored in a typical laboratory atmosphere and within a desiccator for six months, before they were evaluated again for various analysis, including water splitting measurements. Although no change in UV-Visible spectra and other physico-chemical properties, such as surface area, Raman spectra, absorption spectra, was observed but these materials exhibited very low H_2 production values after six months of synthesis. Surprisingly hydrogen production results from these materials (after six months of on shelf) are drastically decreased; hydrogen generation results for 20B and 30AP are depicted, along with that of the fresh materials, for comparison in figure 8. Apparently, the changes and effects created by the high pressure/temperature hydrogen treatment seems to be not sustainable for longer time of even few months. More detailed studies are required to understand the changes that occur after the synthesis.

5.3.2 Dye Sensitized Solar Cell Studies

Figure 9 shows the photocurrent-voltage (J-V) characteristics of the DSSCs made of various photoanodes prepared after hydrogen treatment of TiO_2 under different conditions. Gold photodeposited on TiO_2 prepared by solution combustion method (AuT0) was also measured for DSSC. Result obtained from parent TiO_2 prepared by solution combustion method was also included and compared. Photovoltaic properties, such as open circuit voltage (Voc), short circuit current (Jsc), fill factor (FF), and efficiency (η) are shown in Table 2. 20B material show the highest η of 7.1%, indicating the efficacy of high pressure hydrogen reduction treatment in light harvesting function. Although 20B shows moderate surface area of 67 m^2/g, the highest efficiency is attributed to feasible dye absorption due to large pore diameter with moderate crystallinity. The enhanced device performance with modified H-TiO_2 may be due to band gap reduction of material, formation of Ti^{3+} species. Mesoporosity with high surface area associated with (T0) shows a moderate

efficiency of 5 %. Low porous 40AP shows the lowest efficiency underscoring the necessity of textural characteristics for various functions from dye absorption to charge diffusion and current generation.

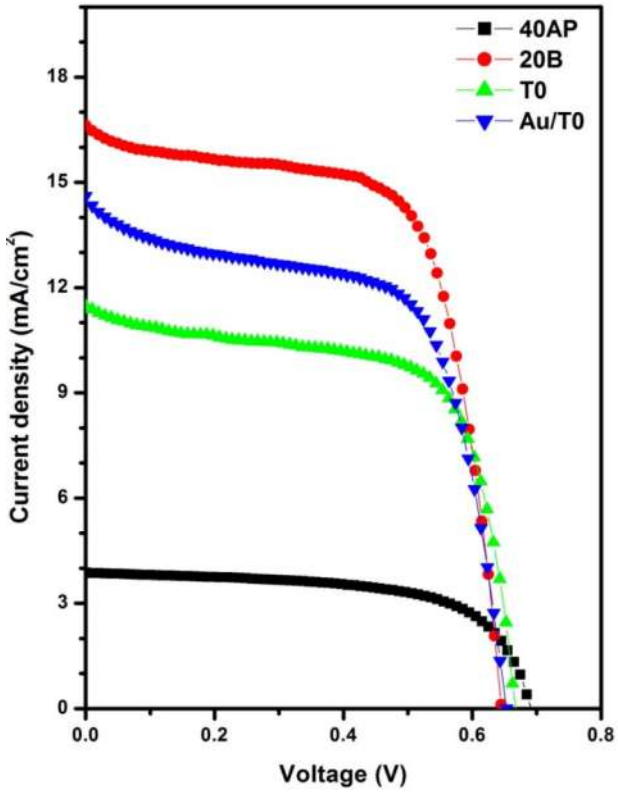

Figure 9. JV plot results are shown for different TiO_2 material, N719 dye is used for sensitization.

It is to be noted that high Jsc and fill factor of 20B fully helps to achieve the highest efficiency. The enhanced device performance with 20B may be partly due to band gap reduction of material, including the availability of Ti^{3+} species. Marginal decrease in Voc observed for all materials compared to parent T0 indicate the scope to improve the efficiency further. We believe that a moderate crystallinity and surface area and porosity help towards maximum dye absorption and charge diffusion, respectively, to increase the efficiency.

Impedance measurement, The equivalent circuit diagram of the DSSC is shown (Figure 10). Resistance (Rs) corresponds to sheet resistance at FTO plate, which is connected via series to resistance (R_2) arising at the interface between mesoporous

titania and dye. The last resistance component (R_3) of diffusion controlled charge transfer resistance of electrolyte was fitted with Warburg diffusive resistance (W_S). The capacitance of TiO_2/electrolyte and electrolyte diffusion can be measured as C_2 and C_3, respectively.

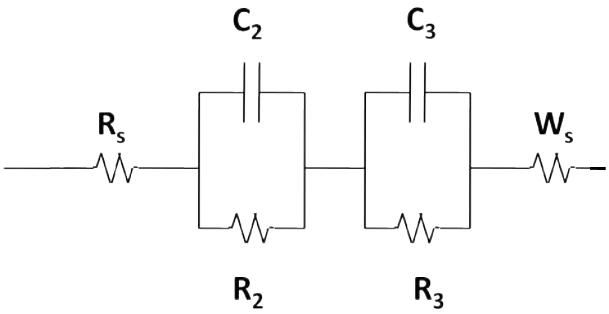

Figure 10. Equivalent circuit diagram for DSSC.

Since our focus in DSSC device is associated with the photo anodes with different TiO_2, we have elucidated the charge carrier accumulation at photo anodes using Electrochemical Impedance Spectroscopy (EIS). The impedance measurements were carried at room temperature using Autolab PGSTAT30 (Eco-Chemie). The impedance measurements of all the samples were made in dark conditions with different applied voltage (VF). The devices were fabricated using I^-/I_3^-redox electrolyte with standard N719 dye as a sensitizer. 40AP, 20B, T0 and AuT0 are used as an anodic material. In principle, a good anode should generate more charge carrier density with relatively less charge recombination. In order to find out the charge carrier accumulation and recombination at TiO_2 anodes, we have maintained the dye concentration, loading time as constant for all devices. The Nyquist plots for the DSSC device with different anode materials are shown (Figure 11).

The impedance spectrum of DSSC mainly consists of three semicircles recognized for the interface between Pt|electrolyte (Z1), TiO_2|dye|electrolyte (Z2) and diffusion of I_3^-(Z3) (refer Figure 11 for more details) in the electrolyte, respectively. The resistance elements R1, R2, and R3 are described as the real part of Z1, Z2, and Z3, respectively. The resistance element Rs in the high frequency region (1 MHz) is subjected to the sheet resistance at the interface of transparent conducting oxide (TCO) and TiO_2. The response at the high-frequency range (500000-1000 Hz) is credited to the charge-transfer process at the electrolyte/Pt interface. The midfrequency range between 1000 and 1 Hz is governed by the charge-transfer

process at the TiO_2/dye/electrolyte interface. It is generally understood that these frequencies represent the recombination process between electrons in TiO_2 and the electrolyte. In the low-frequency region of 1-0.0002 Hz, the arc depicts the mass transport resistance of ions in the electrolyte. The larger semicircle at low frequency region indicates improved ion diffusion in electrolyte. The middle frequency region represents the charge carrier dynamics across the TiO_2/dye/electrolyte interfaces. The charge carrier accumulation at TiO_2 anode can be measured in terms of chemical capacitance (Cμ). We are successful to observe the higher Cμ for the devices fabricated with 20B, could attribute the same to the enhanced carrier accumulation at TiO_2 reduced at 20 bar H_2 pressure. In order to check the possibility of increasing the power conversion efficiency (PCE), the TiO_2 was reduced at 400°C (40AP). Surprisingly, the devices fabricated with 40AP have shown detrimental effect in PCE. This decreasing in the PCE by 75% could be attributed to the agglomerate formation of TiO_2 at higher temperatures which is acting as a charge trapping sites and leads to poor PCE.

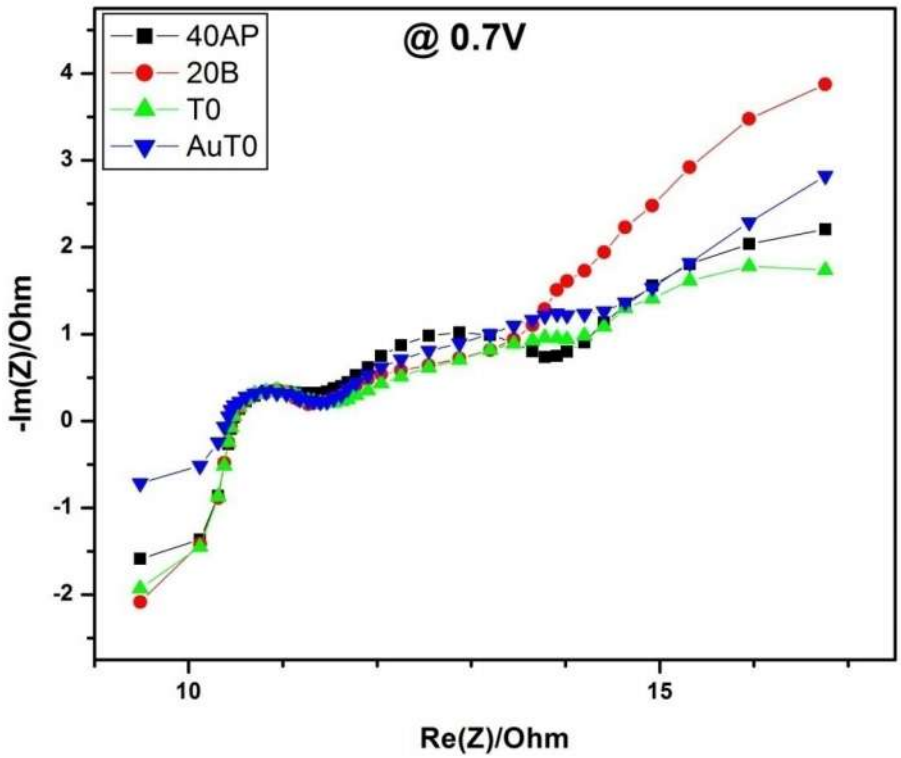

Figure 11. Electron impedance spectroscopy results are shown above for the materials at 0.7 V.

The controlled experiments were carried out using TiO_2 without H_2 reduction shows relatively less device performance (5.04%), is also convincing our approach of reducing the photo anode TiO_2 in DSSC. Furthermore, the incorporation of Au metal nano particles in semiconducting metal oxide (AuT0) was also has been analyzed. Significant improvement has been observed for metal nano particle incorporated devices compared to T0 could be related with the surface plasmonic enhanced light absorbance [28]. However, the PEC measurements was found to be low in efficiency than that of the devices fabricated using 20B TiO_2. This clearly proves our hypothesis that by selectively reducing the TiO_2 photo anodes with optimized conditions like pressure and temperature, the high performance in device efficiency could be achieved. It may also happen that the charge-transfer at the TiO_2/dye/electrolyte interface is strongly dominated by the Pt/electrolyte interface. The fit results are presented in Table 2.

Dye sensitized solar cells fabricated with H-TiO_2 materials, but after a storage period of six months, showed efficiency lower than 4 %, including 20B. Indeed charge separation and diffusion are the two critical parameters for higher efficiency. Low efficiency suggests the disintegration of the material at microstructural level, which needs to be explored thoroughly by microscopy. However, the result generally reiterates the unsustainable nature of H-TiO_2.

Table 2. Electrochemical impedance spectroscopy parameters and J-V plot parameters obtained for the solar cell.

Anode materials	R_{ct} **(Ω)**	C_{μ} **(μF)**	τ_n **(ms)**	**Voc (V)**	**Jsc (mA/cm^2)**	**FF (%)**	**η (%)**
T0	3.5	35.6	124.5	0.66	11.4	66	5.0
20B	8.0	93.3	746.2	0.64	16.6	67	7.1
40AP	4.0	19.1	76.4	0.69	3.87	63	1.7
AuT0	6.0	60.5	363.1	0.65	14.6	61	5.8

5.4 Conclusions

TiO_2 material is well studied material in photocatalysis but its practical use is limited because of wide band gap. We have prepared reduced TiO_2 under different environments i.e. under high temperatures at different hydrogen pressures.Band gap

engineering and structural modification has been attempted through H-TiO_2 materials. After modification they show extended absorbance in visible region of solar spectrum. Rutile phases of TiO_2 developed along with the original anatase phase of T0 material. Textural changes happened after modification; H-TiO_2 materials still exhibit mesoporosity, surface area for the modified material decreased than the parent T0, while pore sizes and crystallite sizes are increased after modification. Reduced Ti^{3+} species are generated in the material, generated Ti (III) has electronic configuration $3d^1$ which means a state closer to conduction band. These H-TiO_2 materials exhibit hydrogen production from aqueous methanol solution. Better H_2 production results are observed under AM1.5 light compared to UV-Visible light source, without any added co-catalysts. Textural properties along with electronic factors are modified, thus improving separation of electron and hole pair ultimately leading to better solar harvesting efficiency. High short circuit current (Jsc), open circuit voltage (Voc), fill factor (FF) and efficiency values are obtained for DSSC prepared with H-TiO_2 as anode material.

Sustainability aspects of H-TiO_2 was evaluated after a period of six months storage in a typical laboratory atmosphere. Large decrease in water splitting and DSSC activity suggests the less sustainable nature of H-TiO_2. Although bulk physico-chemical properties are retained, material disintegration at microstructural level is likely to play a role in decreasing the activity and sustainability. More studies are required to explore further.

5.5 References

1. N. Armaroli, V. Balzani, *Angew. Chem. Int. Ed.* (2007) **46** 52–66.
2. N. S. Lewis, D. G. Nocera, *PNAS* (2006) **43** 15729–15735.
3. C. Strumpel, M. McCann, G. Beaucarne, V. Arkhipov, A. Slaoui, V. Svrcek, C. del Canizo, I. Tobias, *Solar Energy Mat. & Solar Cells* (2007) **91** 238–249.
4. W. McDowall, M. Eames, *Energy Policy* (2006) **34** 1236–1250.
5. J. Wu, Z. Lan, J. Lin, M. Huang, Y. Huang, L. Fan, G. Luo, *Chem. Rev.*(2015) **115** 2136−2173.
6. B. O'Regan, M. Gratzel, *Nature* (1991) **353** 737-739.
7. M. M. Lee, J. Teuscher, T. Miyasaka, T. N. Murakami, H. J. Snaith, *Science* (2012) **338** 643-647.

8. K. Sivaranjani, S. Agarkar, S. B. Ogale, C. S. Gopinath, *J. Phys. Chem. C* (2012) **116** 2581–2587.
9. K. Hashimoto, H. Irie, A. Fujishima, *Jpn. J. Appl. Phys.* (2005) **44** 8269-8285.
10. A. L. Linsebigler, G. Lu, J. T. Yates, *Chem. Rev.* (1995) **95** 735-758.
11. A. Fujishima, K. Honda, *Nature* (1972) **238** 37-38.
12. J. He, J. Zhao, T. Shen, H. Hidaka, N. Serpone, *J. Phys. Chem. B* (1997) **101** 9027-9034.
13. B. H. Meekins, P. V. Kamat, *J. Phys. Chem. Lett.* (2011) **2** 2304–2310.
14. I. Robel, V. Subramanian, M. Kuno, P. V. Kamat, *J. Am. Chem. Soc.* (2006) **128** 2385-2393.
15. Q. Xiang, J. Yu, M. Jaroniec, *J. Am. Chem. Soc.* (2012) **134** 6575−6578.
16. D. A. Wheeler, Y. Ling, R. J. Dillon, R. C. Fitzmorris, C. G. Dudzik, L. Zavodivker, T. Rajh, N. M. Dimitrijevic, G. Millhauser, C. Bardeen, Y. Li, J. Z. Zhang, *J. Phys. Chem. C* (2013) **117** 26821−26830.
17. R. Plass, S. Pelet, J. Krueger, M. Gratzel, *J. Phys. Chem. B* (2002) **106** 7578–7580.
18. R. Asahi, T. Morikawa, T. Ohwaki, K. Aoki, Y. Taga, *Science* (2001) **293** 269-271.
19. X. Chen, L. Liu, P. Y. Yu, S. S. Mao, *Science* (2011) **331** 746-750.
20. X. Chen, L. Liu, F. Huang, *Chem. Soc. Rev.* (2015) **44** 1861-1885.
21. L. Barretoa, A. Makihira, K. Riahi, *Int. Journal of Hydrogen Energy* (2003) **28** 267 – 284.
22. S. M. Sajjadi, M. Haghighi, F. Rahmani, *Journal of Natural Gas science and Engineering* (2015) **22** 9-21.
23. D. E. Carlson, C. R. Wronski, *Appl. Phys. Lett.* (1976) **28**, 671-673.
24. L. Tao, Z. Huo, Y. Ding, Y. Li, S. Dai, L. Wang, J. Zhu, X. Pan, B. Zhang, J. Yao, M. K. Nazeeruddin, M. Gratzel, *J. Mater. Chem. A* (2015) **3** 2344-2352.
25. S. Kumarsrinivasan, S. Agarkar, S. B. Ogale, C. S. Gopinath, *Journal of Physical Chemistry C*, (2012) **116** 2581-2587; K. Sivaranjani, C. S. Gopinath, *J. of Mater. Chem.,* (2011) **21** 2639-2647; M. Satish, B. Viswanathan, R. P. Viswanath, C. S. Gopinath, *Chem. of Mater.*, (2005) **17** 6349-6353.
26. N. C. Saha, H. G. Tompkins, *J. Appl. Phys.* (1992) **72** 3072-3079; E. Gyorgy, A. P. D. Pino, P. Serra, J. L. Morenza, *Surf. Coat. Technol.* (2003) **173** 265-270.

27. Z. Wang, C. Yang, T. Lin, H. Yin, P. Chen, D. Wan, F. Xu , F. Huang , J. Lin , X. Xie , M. Jiang, *Adv. Funct. Mater.* (2013) **23** 5444–5450.
28. S. T. Kochuveedu, D. P. Kim, D. H. Kim, *J. Phys. Chem. C* (2012) **116** 2500–2506.

Chapter VI: Conclusions and Future Outlook

This chapter summarizes the present thesis work and the conclusions and possible future implications that can be extended from the work.

Chapter 1

Gives a brief introduction about catalysis, and discussed about the importance of porosity, particularly ordered and disordered mesoporosity toward catalysis. IUPAC's has used pore size dimension as for classifying materials as micro, meso and macro porous; mesoporous are the most appropriate for catalysis and other relevant fields. Role of disordered mesoporosity in enhancing the diffusion and hence overall catalysis was discussed. A brief introduction about the Titanium dioxide materials, different phases and properties of titania material are discussed such as reducibility, semiconducting nature and effect of doping foreign elements on the properties. V/TiO_2 have been used for sulfoxidation, Mn/TiO_2 used for styrene synthesis, $H\text{-}TiO_2$ is used for H_2 generation via photocatalytic water splitting and as anodic material in solar cell for converting solar light to electricity as discussed in detail in the later chapters. Also this chapter presents trend and challenges present for these catalytic problems.

Chapter 2

Chapter two discusses about the theoretical and experimental procedures used by us in chapters three, four and five for materials preparation and analysis. Solution combustion method is a simple method and propagates through either voluminous or self propagation mode used for vanadium or manganese doped titanium dioxide material. Reduction method was another method used for material preparation i.e. $H\text{-}TiO_2$, used in photocatalysis; it is a simple method to generate new species in the materials which has been reported to improve the activity, without any added foreign elements. Incipient wet impregnation method was also used for preparing materials for comparison via conducting control test reactions. Many different experimental procedures were pursued for catalytic applicability such as sulfoxidation was carried out under single pot reaction set up using V/TiO_2 and aq. H_2O_2. Ethylbenzene to styrene was carried out in fixed bed flow reactor; reactant flow and temperature parameters were varied and studied. Photocatalytic water splitting for hydrogen production was studied using $H\text{-}TiO_2$ under different light conditions. Dye sensitized solar cell were fabricated using $H\text{-}TiO_2$ as anode material and were tested for solar

light harvesting to generate electricity, understanding the processes via obtained solar cell parameters. Theoretical understanding of analysis/characterization methods used were discussed, the list is like powder XRD, surface area determination by N_2 adsorption studies, UV-Visible spectroscopy (DRS), DRIFTs, Raman spectroscopy, X-Ray photoelectron spectroscopy, transmission electron microscopy, scanning electron microscopy (SEM), energy dispersive analysis of X-rays, thermo gravimetric analysis, linear sweep voltammetry, cyclic voltammetry, solid state NMR etc.

Chapter 3

In chapter 3 we have focused on oxidation reactions; oxidation reactions are ubiquitous from long time and they have carried out at industrial scales, but these industrial practices show inherent drawbacks such as usage of heavy metal salts, leaching of metal ions and harsh operating conditions and use of non-environment friendly green oxidants. Sulfoxides are pharmaceutically important molecules and sulfide oxidation is usually practiced for the synthesis. Sulfide oxidation is a sequential process as sulfide is oxidized to sulfoxide (partial oxidation product), and further sulfoxide undergoes oxidation and generates sulfone molecules. In this chapter we have presented V/TiO_2 along with H_2O_2 oxidant for sulfide to sulfoxide conversion under optimized reactions conditions for best sulfoxide yields. Importance of the catalysts lies in making isolated vanadium ion within the lattice of titania and isolated vanadium increases the partial (or controlled) oxidation of sulfides. Structural analyses of materials were also discussed in the chapter. Catalyst with 0.1, 0.25, 0.50, 0.75, 1.0 and 2.0 Vanadium weight percentage compositions were prepared and studied for sulfoxidation and 0.1% composition exhibit the best yield. Catalysts were active at ambient and below ambient temperatures conditions, thus best selectivity can be achieved at 278 K. Several organic sulfide molecules have been evaluated for sulfoxidation with V/TiO_2 catalyst. Reusability or robustness of the catalysts was maintained for three cycles studied, without showing much appreciable loss in activity for different sulfides. These materials can be applied for partial oxidation reactions at milder conditions such as alkene's epoxidation reactions and alkane to alkene oxidation studies. It is worth exploring partial oxidation reactions with V/TiO2 catalysts under mild conditions.

Chapter 4

Styrene is an industrially important precursor, for petrochemical polymer and other industries. Many different catalysts are currently being developed which operates via different mechanisms and significant amount of research is going on to make styrene synthesis process more energy viable or by adopting green routes. One such green route was followed at significantly lower temperatures for EB to styrene conversion with air and oxygen. $Mn_xTi_{1-x}O_2$ catalysts were prepared via solution combustion method and evaluated for styrene synthesis through oxidative dehydrogenation (ODH); $Mn_xTi_{1-x}O_2$ catalysts were characterized using various physio-chemical methods. Manganese oxides are highly active redox catalysts for high temperature conversions, and industrially styrene is generated from ethylbenzene. Ethylbenzene to styrene conversion was thoroughly analyzed for optimization of the reaction conditions, catalyst composition and reactants flow rates. Manganese content of 2 to 15 weight percentages were studied for the styrene synthesis and results shows that 15 % Mn-containing titania gives the best catalytic activity. Reactants such oxygen or air and ethylbenzene flow rate were varied and studied so as to maintain high styrene selectivity, results from many batch studies infer us that 1.8 ml/h EB flow and 180 ml/min air flow gives the highest styrene selectivity and yield. Operating temperatures for the styrene synthesis were contentedly very low compared to as employed in industries using different catalysts. Results from temperature studies of 440, 470, 500, and 530 °C were compared and the highest styrene selectivity and yield are achieved at 530 °C. The progress of reaction for continuous 45 hrs without showing any decrease in activity under optimum reaction condition shows robustness of the catalyst and makes $Mn_xTi_{1-x}O_2$ material good candidate for industrial catalysis.

Understanding of active phase of the catalyst was attempted by characterizing catalysts after the reaction. Characterization results from XRD confirm development of rutile phase along with additional manganese oxide (Mn_3O_4) phases. Raman studies of spent catalyst also infer the presence of rutile phase, which is present in a very small amount at the beginning of reaction. Mechanism for the conversion over $Mn_xTi_{1-x}O_2$ catalyst was explored via controlled reaction over a Mn_3O_4 supported over rutile titania and carrying out the ODH reaction in the absence and later on in the presence of oxygen flow. Thus the results from the studies clearly indicates that Mn_3O_4 supported over rutile titania as the active catalyst and it follows Mars-van Krevelen mechanism in which oxygen molecule adsorbs on catalyst surface and

diffuses into the sub-surfaces and bulk of the catalyst, while lattice oxygen is being used for ODH reaction. $Mn_xTi_{1-x}O_2$ catalysts can be exploited in future for other alkanes to alkene conversion studies also for industrially important metathesis reactions.

Chapter 5

Sunlight is abundant and human race population and energy needs are ever increasing. Extensive research is being carried out to tap the abundant source of solar energy and convert into various forms of energy, to fuel our vehicles and provide electricity to our homes. TiO_2 is a well-studied photocatalysts, but only active in UV light. An attempt has been made to change the bandgap of titania through hydrogen reduction by creating new electronic state in the forbidden gap and utilize the solar energy directly for light to energy conversion. Reduction in band gap is evident from the light absorption, colour changes and ensuing water splitting activity and DSSC efficiency measurements under simulated solar light conditions. Indeed H-TiO_2 exhibits water splitting activity, without any noble metal catalysts is an attractive feature. Nonetheless, H-TiO_2 seems to have poor sustainable character and conversion of solar light to electricity or chemical conversion shows poor activity after six months of storage. This indicates the significant solar catalytic activity associated with H-TiO_2 needs to be made sustainable by suitable treatment. Efficient microstructural integration of as-prepared H-TiO_2 could be a possible strategy to sustain the activity for longer time period.

List of Publications

1. *Disordered mesoporous V/TiO_2 system for ambient oxidation of sulfides to sulfoxides*,
   Sanjay Singh Negi, Kumarsrinivasan Sivaranjani, Anand Pal Singh, Chinnakonda S. Gopinath,
   Applied Catalysis A: General, 452 (2013) 132 – 138.

2. *A green chemistry approach to styrene from ethylbenzene and air on $Mn_xTi_{1-x}O_2$ catalyst*,
   Sanjay Singh Negi, Aswathy Thareparambil Venugopalan, Thirumalaiswamy Raja, Anand Pal Singh and Chinnakonda S. Gopinath,
   RSC Advances, 4 (2014) 57087-57097.

3. *Synthesis characterization and catalytic application of H-TiO_2 materials for solar light harvesting,*
   Sanjay Singh Negi, Anand Pal Singh and Chinnakonda S. Gopinath,
   Manuscript is to be submitted.

4. *Morphology controlled oxygen evolution studies with nano $Ti_{10}Ce_{90}O_2$ photocatalyst under different light sources,* Anjani Dubey, **Sanjay Singh Negi,** and Chinnakonda S. Gopinath,
   Manuscript is to be submitted.

Presentations in National/International Conferences/Symposia

1. *Nature of the acid sites in the metal triflates immobilized in SBA-15 and their role in the Friedel-Crafts acylation of naphthalene.*
   Sanjay Singh Negi, Selva Kumar and Dr. A. P. Singh,
   National Science Day, NCL, Pune February 24-25 (2010)

2. *Disordered mesoporous V/TiO_2 system for ambient oxidation of sulfides to sulfoxides.*

Sanjay Singh Negi, K Sivaranjani, Dr. A. P. Singh and Dr. C. S. Gopinath, National Science Day, NCL, Pune February 26-27 (2013)

3. *A green process for ethyl benzene to styrene with air on $Mn_xTi_{1-x}O_2$ catalyst.*
Sanjay Singh Negi, T. Aswathy, Dr. T. Raja, Dr. A. P. Singh and Dr. C. S. Gopinath,
Catalysis Society of India, 16th National Workshop on Catalysis for sustainable development, CSIR-NEERI, Nagpur February 4-5 (2014)

4. *Solar light harvesting aspects with black titania*
Sanjay Singh Negi, Dr. A. P. Singh and Dr. C. S. Gopinath,
National Science Day, NCL, Pune February 25-28 (2015)

Conferences Participated

1. *Preschool on spectroscopic methods in catalysis*, Indian Institute of Technology, Chennai December 17-18 (2010).

2. *20th national symposium on catalysis*, Indian Institute of Technology, Chennai December 19-22 (2010).

3. *International Conference on Structural and Inorganic Chemistry*, hosted by CSIR-NCL, IISER Pune, SP Pune university, December 4-5 (2014)

4. *17th CRSI National Symposium in Chemistry*, at CSIR-National Chemical laboratory, Pune (India) held from February 6-8 (2015)